Differences in interactions between transmembrane domains tune the activation of metabotropic glutamate receptors

Jordana K. Thibado[1], Jean-Yves Tano[2], Joon Lee[3], Leslie Salas-Estrada[4], Davide Provasi[4], Alexa Strauss[5], Joao Marcelo Lamim Ribeiro[3], Guoqing Xiang[4], Johannes Broichhagen[6], Marta Filizola[3], Martin Lohse[2,7], Joshua Levitz[1,3,5]

[1] Physiology, Biophysics and Systems Biology Graduate Program, Weill Cornell Graduate School of Medical Sciences, New York, NY 10065

[2] Max Delbrück Center for Molecular Medicine, Berlin, 13125, Germany

[3] Department of Biochemistry, Weill Cornell Medicine, New York, NY 10065

[4] Department of Pharmacological Sciences, Icahn School of Medicine at Mount Sinai, New York, NY 10029

[5] Tri-Institutional PhD Program in Chemical Biology, New York, NY 10065

[6] Department of Chemical Biology, Forschungsinstitut für Molekulare Pharmakologie, Berlin, Germany.

[7] ISAR Bioscience Institute, Planegg-Munich, 82152, Germany

*To whom correspondence should be addressed: jtl2003@med.cornell.edu

Abstract:

The metabotropic glutamate receptors (mGluRs) form a family of neuromodulatory G protein-coupled receptors that contain both a seven-helix transmembrane domain (TMD) and a large extracellular ligand-binding domain (LBD) which enables stable dimerization. While numerous studies have revealed variability across subtypes in the initial activation steps at the level of LBD dimers, an understanding of inter-TMD interaction and rearrangement remains limited. Here we use a combination of single molecule fluorescence, molecular dynamics, functional assays, and conformational sensors to reveal that distinct TMD assembly properties drive differences between mGluR subtypes. We uncover a variable region within transmembrane helix 4 (TM4) that contributes to homo- and heterodimerization in a subtype-specific manner and tunes orthosteric, allosteric and basal activation. We also confirm a critical role for a conserved inter-TM6 interface in stabilizing the active state during orthosteric or allosteric activation. Together this study informs a working model of inter-TMD rearrangement that drives mGluR function.

Introduction:

Assembly into multi-subunit complexes is an essential aspect of many membrane receptors. Dimerization or higher-order oligomerization can shape the ligand sensitivity or signaling dynamics of a protein complex by producing various forms of allostery and cooperativity or mediate the formation of binding, functional, or regulatory sites (Changeux and Christopoulos, 2016, Katzung, 2004). In many cases, the formation of a multi-subunit complex is required for function. For example, ligand-gated ion channels require multiple subunits to form a functional pore, making assembly into complexes an absolute necessity. In the case of the vast superfamily of G protein-coupled receptors (GPCRs) the role of quaternary structure has remained more enigmatic. The proposed dimerization of family A GPCRs, such as rhodopsin or the beta-adrenergic receptors, has sparked intense debate based on the wide range of results that are seen across techniques and preparations (Ferré et al., 2014, Milligan et al., 2019, Sleno and Hébert, 2019). However, a reasonable interpretation of the litany of studies is that dimerization can indeed occur and contribute to various modes of regulation of family A GPCR function, but is likely transient, based on single molecule imaging studies (Hern et al., 2010, Kasai et al., 2011, Meral et al., 2018, Işbilir et al., 2020, Möller et al., 2020, Felce et al., 2017), and is not required for G protein activation, based on reconstitution studies (Bayburt et al., 2007, Whorton et al., 2008, Whorton et al., 2007, Kuszak et al., 2009). Importantly, a structural understanding of GPCR dimerization has remained elusive with a wide range of dimer interfaces proposed for different GPCRs based on cross-linking, mutagenesis and x-ray crystallography data. More recently, the concept of dynamic, “rolling” inter-subunit interfaces which inter-change and are associated with different functional states has emerged as a possible explanation for the seemingly incompatible results seen across studies (Gurevich and Gurevich, 2008, Meral et al., 2018, Sleno and Hébert, 2019, Dijkman et al., 2018, Jin et al., 2018). Crucially, dimerization is likely best taken on a case-by-case basis where different dimerization propensities, modes and functional effects are expected for each subtype across the large superfamily of GPCRs.

One major exception to the secondary, modulatory role for dimerization in the function of GPCRs are the family C GPCRs, including the metabotropic glutamate receptors (mGluRs) and a number of other subfamilies (Ellaithy et al., 2020). The family C GPCRs contain canonical seven-helix transmembrane domains (TMDs) but are distinguished by their large, bi-lobed, extracellular ligand binding domains (LBDs), which are essential for their constitutive homo- and hetero-dimerization (Romano et al., 1996, Doumazane et al., 2011, Levitz et al., 2016, Lee et al., 2020). Unlike family A GPCRs, reconstituted mGluR2 monomers are unable to undergo glutamate-mediated G protein activation (El Moustaine et al., 2012), although they can be activated by TMD-targeting allosteric drugs. In response to orthosteric agonists, mGluR LBD dimers undergo dramatic rearrangement between conformations which both reshape and are controlled by a complex inter-LBD dimer interface, as deciphered through crystallographic (Kunishima et al., 2000, Tsuchiya et al., 2002, Muto et al., 2007) and spectroscopic (Levitz et al., 2016, Vafabakhsh et al., 2015, Olofsson et al., 2014) studies. However, how such motions are transmitted to the TMDs, how TMDs can be activated directly by allosteric drugs and the role of associated inter-TMD interactions in this family of receptors remains unclear, although a variety of recent studies have provided insight.

A series of Förster resonance energy transfer (FRET) studies of full-length mGluR1 have shown that glutamate and other agonists produce relative motions between the TMDs that occur on fast millisecond time scales that precede receptor activation (Hlavackova et al., 2012, Marcaggi et al., 2009, Grushevskyi et al., 2019, Tateyama et al., 2004, Tateyama and Kubo, 2006). Structural interpretation of such studies has been limited but the consistently observed FRET efficiency increase seen with intersubunit sensors points to a rearrangement that leads to increased inter-TMD interaction upon LBD activation. Notably, we recently developed an isolated TMD FRET sensor which showed that TMD-targeting allosteric drugs are able to produce intersubunit re-arrangements autonomously without allosteric input from the LBDs (Gutzeit et al., 2019), pointing to a multi-state model of inter-TMD interaction and raising questions about TMD rearrangement in response to allosteric versus orthosteric activation. In line with this, a prior cross-linking study of full-length mGluR2 provided evidence for close proximity of TM4 and TM5 helices in inactive

states and TM6 helices in active states (Xue et al., 2014). Despite such studies, the relative strength of inter-TMD interactions within mGluR dimers remains unknown. High resolution structural studies have provided further insight but no clear consensus regarding TMD interfaces. Crystal structures of isolated mGluR1 (Wu et al., 2014) and mGluR5 (Dore et al., 2014) TMDs have shown TM1-mediated dimerization or monomers, respectively, while a cryogenic electron microscopy (cryo-EM) study of full-length mGluR5 (Koehl et al., 2019) showed no TMD interface in an inactive nanodisc-reconstituted form but a clear TM6 interface in a glutamate and positive allosteric modulator-bound pre-active state. Finally, a series of cryo-EM studies of the related $GABA_B$ receptors showed a lipid-mediated inactive TM5 interface that re-arranged to a TM6 interface in the presence of agonist and a positive allosteric modulator (Mao et al., 2020, Papasergi-Scott et al., 2020, Park et al., 2020, Shaye et al., 2020). Together these studies point to a role for TMD rearrangement in mGluR activation, but the steps prior to formation of a putative active TM6 interface are not clear.

Recent work has also revealed deep conformational heterogeneity between mGluR subtypes at the level of the LBDs that shape the relative activation properties of different homo- and hetero-dimers (Levitz et al., 2016, Vafabakhsh et al., 2015, Habrian et al., 2019). Such findings are in line with the notion that the eight mGluR subtypes are fine-tuned for their distinct roles within the synapse that require unique glutamate sensitivity, activation kinetics and other signaling properties (Reiner and Levitz, 2018). This raises the possibility that such variability between subtypes also exists at the TMDs and can be used as a lens to dissect the TMD activation mechanism. Intriguingly, we recently used a single molecule imaging approach to determine that while all isolated mGluR TMDs tested show a clear propensity for dimerization, the mGluR2 subtype shows substantially higher dimerization propensity than other subtypes (Gutzeit et al., 2019), providing a jumping off point for this study.

Here, we use a combination of optical, functional and computational techniques to dissect the role of inter-TMD interaction in mGluR dimerization and activation with a focus on the highly homologous group II mGluRs. Single molecule fluorescence subunit counting experiments reveal that the TMD

mediates differences in dimer assembly between mGluR2 and mGluR3. Using observations from coarse-grained (CG) molecular dynamics (MD) simulations in conjunction with sequence analysis, mutagenesis, and subunit counting, we isolate this effect to specific residues at the cytoplasmic end of transmembrane helix 4 (TM4). Functional experiments demonstrate that TM4 residues play a modulatory role in both orthosteric and allosteric activation of group II mGluRs and controlling basal activity. Using new inter-TMD FRET sensors in full-length mGluRs, we characterize how orthosteric drugs, allosteric modulators and TM4 residues influence the relative TMD conformational dynamics of group II mGluRs. Further, we demonstrate that activation associated inter-TMD dynamics involve reorientation away from a TM4 inactive interface toward a TM6 active interface by employing single molecule subunit counting experiments in the presence of ligands. Finally, we find that inter-TMD affinity shows an intermediate level in mGluR2/3 heterodimers compared to the homodimers, supporting the role of TMD interactions as mediators of the molecular diversity of mGluRs. Together these results, in combination with existing literature, lead us to propose a three-step mechanism for mGluR activation that considers the role of subtype-specific residues in the TMD that contribute to the functional diversity of mGluR subtypes.

Results:

The transmembrane domain mediates differences in dimerization between metabotropic glutamate receptors

Motivated by our recent finding that isolated mGluR TMDs are able to dimerize to variable levels in the absence of extracellular domains (Gutzeit et al., 2019), we first sought to further understand the molecular basis of mGluR TMD dimerization using single molecule pulldown (SiMPull). In this technique, detergent-solubilized receptor complexes are isolated from fresh cell lysate and sparsely immobilized via antibodies on a glass coverslip. Protein complexes are imaged using TIRF microscopy and photobleaching step analysis of complexes reports on receptor stoichiometry (Jain et al., 2011). We restrict our analysis to

surface receptors by using N-terminally SNAP-tagged receptor constructs labeled with membrane-impermeable fluorophores. Expression and labeling of constructs in HEK 293T cells with benzylguanine-conjugated fluorophore BG-LD555 (Materials and methods) showed fluorescence labeling at the plasma membrane with minimal fluorescence inside the cell (Figure 1A). Receptors were immobilized using an HA-tag at the N-terminus of each construct that directly precedes the SNAP tag (Figure 1B). Consistent with previous work, SNAP-mGluR2-TMD molecules photobleached primarily in one-step (~55%) or two-step (~40%) events with a small population of ≥3 steps (~4 %) (Figure 1C). This represents a population of ~80% dimers when normalized to the obligatory dimerization of SNAP-mGluR2 (Figure 1D; see Materials and methods) (Gutzeit et al., 2019).

Since mGluR TMDs do not form strict dimers, we asked if our preparation maintains the cellular composition of monomers and dimers or if TMDs exchange with one another during SiMPull experiments such that new dimers are formed. To test this, we either co-expressed HA-SNAP-mGluR2-TMD and CLIP-mGluR2-TMD and labeled the same coverslip with both BG-LD655 (for SNAP) and BC-DY547 (for CLIP) or transfected and labeled separate coverslips with either constructs/fluorophore combination prior to mixing and co-lysis (Figure 1–figure supplement 1A-C). Following lysis, protein complexes were isolated via an anti-HA antibody. As expected, in the positive co-expression control HA-SNAP-mGluR2-TMD was able to co-precipitate many spots for CLIP-mGluR2-TMD (Figure 1—figure supplement 1D). In contrast, we observed background levels of spots for the test condition where separate populations of cells were mixed following labeling (Figure 1—figure supplement 1E, F). This suggests that there is no exchange between TMD dimers within detergent on the timescale of our experiments and indicates that our technique can be thought of as capturing a "snapshot" of TMD dimers and monomers in the cell membrane at the time of lysis.

Consistent with prior work, SNAP-mGluR3-TMD molecules photobleached with a greater number of one-step (~70%) events, less two-step (~30%) events, and a similarly small population of ≥3 steps (~3%) (Figure 1C) compared to SNAP-mGluR2-TMD. Thus, unlike their full-length counterparts which both

show strict dimerization (Levitz et al., 2016), mGluR2-TMD and mGluR3-TMD show distinct dimerization propensities that are less than an obligate dimer but greater than a canonical class A GPCR, β2AR, which we used as a monomeric or weak dimerization control (Figure 1D). Importantly, SNAP-mGluR2-TMD and SNAP-mGluR3-TMD retained ~80% and ~50% dimerization, respectively, regardless of whether they were immobilized via their N or C-terminus (Figure 1—figure supplement 2).

To confirm that the dimerization propensities observed in detergent-based single molecule subunit counting experiments reflect those occurring in the cell membrane, we measured ensemble FRET levels for the TMDs of both mGluR2 and mGluR3 at comparable expression levels in live cells. SNAP-mGluR2-TMD or SNAP-mGluR3-TMD constructs were labeled with SNAP-reactive donor (BG-LD555) and acceptor (BG-LD655) fluorophores and fluorescence recovery of the donor was examined following acceptor bleaching with 640 nm illumination (Figure 1—figure supplement 3A). The percent change in donor fluorescence was greater for SNAP-mGluR2-TMD compared to SNAP-mGluR3-TMD, consistent with the interpretation that mGluR2 has a greater inter-TMD dimerization propensity compared to mGluR3 (Figure 1—figure supplement 3B). As a control, SNAP-β_2AR showed less donor recovery than both mGluR constructs (Figure 1—figure supplement 3B). Combined, these results indicate that our single molecule experiments are an accurate reflection of mGluR dimerization in the membrane.

Next, we asked whether the variable propensity for TMD dimerization between mGluR2 and 3 has an effect in the full-length receptor context. To sensitize our constructs to effects at non-covalent interfaces, we mutated a cysteine within the LBD that produces an inter-subunit disulfide bond. Consistent with previous work (Levitz et al., 2016), mutation of the intersubunit disulfide bridge in mGluR2 (C121A) had a minimal effect on mGluR2 dimerization (Figure 1E). However, in stark contrast, the equivalent mutation in mGluR3, C127A, produced a substantial 2-fold reduction in dimerization (Figure 1E). We hypothesized that differences in sensitivity to cysteine mutation are due to differences in the relative strength of inter-TMD interaction and reasoned that if the TMD plays a role in mGluR dimerization, an mGluR2-C121A chimera with the mGluR3 TMD ("mGluR2-C121A-mGluR3TMD") would reduce dimerization further.

Indeed, this construct showed normal expression (Figure 1—figure supplement 4) but reduced dimerization compared to mGluR2-C121A (Figure 1F). We next tested the reverse chimera to see if the mGluR2-TMD can rescue the weak dimerization of mGluR3-C127A. As hypothesized, "mGluR3-C127A-mGluR2TMD" showed un-altered expression (Figure 1—figure supplement 4) but increased dimerization compared to SNAP-mGluR3-C127A (Figure 1F). Together these results indicate that the TMD mediates differences in dimerization between full-length mGluR2 and mGluR3. Specifically, the greater dimer propensity between mGluR2 TMDs strengthens the full-length mGluR2 dimer while the lower affinity inter-TMD interactions in mGluR3 leads to less favorable dimer formation and therefore greater dimer dissociation in the mGluR3-C127A background (Figure 1G). Notably, TMD chimeras were not able to fully swap the relative dimerization propensities between subtypes, suggesting that other differences outside of the TMD also contribute to differential assembly of mGluR2 and mGluR3.

Residues in TM4 control the relative TMD dimerization propensities of mGluR2 and mGluR3

Having demonstrated that the TMD plays a critical role in subtype-specific modes of mGluR dimerization, we wondered which specific regions of the TMD contribute to this effect. Together the existing literature suggests that inter-TMD interaction among class C GPCRs is multifaceted and diverse (see Introduction), motivating further analysis and careful comparison between receptor subtypes. We started by assessing sequence conservation across mGluR subtypes and between mGluR2 and mGluR3. Across all eight rat mGluRs, most TM helices show <50% sequence conservation and <30% sequence identity, while TM6 stands out as the most similar, with 96% conservation and 72% identity (Figure 2-figure supplement 1A). Analysis of only the group II mGluRs reveals much greater sequence similarity, with all TMs having >80% conservation. Restricting analysis to outward-facing residues (defined by homology models based on the mGluR5 TMD crystal structure), which we expect to disproportionately contribute to TMD interface formation, we see marked differences (Figure 2-figure supplement 1A-C). Across all mGluRs, only TM6 remains highly similar, with 87.5% conservation and 87.5% identity.

Between the group II mGluRs, conservation remains high (>70%) for all TMs except for TM4 (33%) (Figure 2B). TM4 identity is also the lowest of the TMs at 0%. Given that the overall sequence identity between mGluR2 and mGluR3 is nearly 70%, it is reasonable to hypothesize that the increased heterogeneity of TM4 contributes to subtype-specific differences in TMD dimerization.

To further address the TMD dimer interfaces of mGluR2 and mGluR3 we used extended CG MD simulations of pairs of receptors randomly placed relative to each other in a 1-palmitoyl-2-oleoyl-sn-glycero-3-phosphocholine (POPC) lipid bilayer (Figure 2—figure supplement 2A) and analyzed them with Markov state models (MSMs) (Figure 2—figure supplement 2B). The results confirm a higher dimerization propensity for mGluR2-TMD compared to mGluR3-TMD (~40% and ~25% dimeric fractions, respectively), and a differential involvement of TMs in dimeric interfaces. We compiled all simulated dimer structures into macrostates consisting of a variety of symmetric and asymmetric configurations involving different combinations of TM helices (Figure 2—figure supplement 2B, C). Significant transition fluxes observed between the different dimeric macrostates (Figure 2—figure supplement 2B) indicate that direct interconversion between some of the identified dimeric configurations does not require reverting first to the monomeric state.

To provide rough estimates of the effect of the extracellular domains on the stability of mGluR2-TMD or mGluR3-TMD dimeric configurations identified in simulations, we carried out steered MD simulations of full-length CG models to representative dimeric configurations of the two receptors and calculated free-energy differences between them. While the identified symmetric (TM1,TM7)/(TM1,TM7) dimeric configuration of mGluR2-TMD was confirmed to be more stable than the asymmetric (TM1,TM7)/(TM4,TM3) and (TM1,TM7)/(TM5) mGluR2-TMD dimers (free-energy differences of -580 ± 18 kJ mol^{-1}, -169 ± 18 kJ mol^{-1}, respectively) in the presence of the LBD, other dimeric configurations such as the symmetric (TM4)/(TM4) dimer of mGluR2 (Figure 2—figure supplement 3A), showed higher compatibility with the full-length receptor than the (TM1,TM7)/(TM1,TM7) dimer and other highly populated macrostates (free energy differences of -1370 ± 18 kJ mol^{-1}, -1950 ± 18 kJ mol^{-1}, and -1540 ± 18

kJ mol^{-1} from the (TM1,TM7)/(TM1,TM7), (TM1,TM7)/(TM4,TM3), and (TM1,TM7)/(TM5), respectively). In contrast, the identified (TM4)/(TM4) dimer configuration of mGluR3-TMD (Figure 2—figure supplement 3B), was estimated to be less stable than the identified largest mGluR3-TMD dimer macrostate in the presence of the LBD (free-energy difference of +630 ± 12 kJ mol^{-1} from the (TM2,TM7)/(TM3) interface).

Together, examination of amino acid sequence conservation and MSM analysis of CG MD simulations point to TM4 as a potential mediator of the differential TMD dimerization of mGluR2 and mGluR3. Intriguingly, differences in TM4 between the group II mGluRs have been reported to contribute to the specific interaction of mGluR2, but not mGluR3, with the 5-HT_{2A} serotonin receptor, a class A GPCR (Gonzalez-Maeso et al., 2008, Fribourg et al., 2011, Moreno et al., 2016, Delille et al., 2012). This interaction has been attributed to three outward-facing alanine residues (A677, A681, A685) at the cytosolic end of TM4 of mGluR2 (Figure 2A) that allow mGluR2, but not mGluR3, to interact with 5-HT_{2A}R (Moreno et al., 2012). Importantly, these three alanine residues and the corresponding residues in mGluR3 are conserved across species (Figure 2—figure supplement 1D) and are observed within many of the TM4-containing dimer interfaces obtained by CG MD simulations (Figure 2—figure supplement 3). We thus wondered whether these alanine residues also play a role in mGluR homodimer formation.

To test our hypothesis, we swapped A677, A681 and A685 in mGluR2 with the corresponding residues in mGluR3: S686, F690 and G694 (Figure 2A, B) and vice versa to create two mGluR-TMD mutants, “mGluR2-TMD-3xTM4” and “mGluR3-TMD-3xTM4”. Both mutants expressed similarly to wild-type receptors in HEK 293T cells and single molecules were isolated for SiMPull experiments (Figure 2—figure supplement 4A, B). Strikingly, we found that dimerization propensity was determined by which 3xTM4 residues were present in the construct (Figure 2C). For mGluR2-TMD-3xTM4, we observed a reduction in dimerization from ~80% for mGluR2-TMD to ~50%. Conversely, mGluR3-TMD-3xTM4 increased dimerization from ~45% for mGluR3-TMD to ~70%. These data indicate that TM4 residues determine the relative dimerization propensity of group II mGluRs at the TMD level. Single amino acid

swap constructs in the SNAP-mGluR2-TMD background show that although each mutation individually alters dimerization, all three mutants combined in the 3xTM4 constructs are required for the greatest effect (Figure 2—figure supplement 4C, D).

We also examined whether mutating other non-conserved outward-facing residues in TM4 influences TMD dimerization. We swapped mGluR2 residues A695 and A696 with mGluR3 residues S703 and V704 to make mGluR2-TMD-A695S/A696V. Notably, these positions were shown to cross-link in a prior study of mGluR2 (Xue et al., 2014). mGluR2-TMD-A695S/A696V exhibited indistinguishable dimerization compared to SNAP-mGluR2-TMD, suggesting that outward-facing residues at the extracellular end of TM4 do not influence the relative TMD dimerization propensities between mGluR2 and mGluR3 (Figure 2—figure supplement 5A, B). We also tested differences between mGluR2 and mGluR3 in TM1 (F584, G587 in mGluR2 and I593, T596 in mGluR3) and TM5 (A726, G730, A733 in mGluR2 and S735, I739, T742 in mGluR3) by swapping non-conserved outward-facing residues and observed no effect in SiMPull (Figure 2—figure supplement 5C-E). Notably, among these residues, only one (F584 in mGluR2 and I593 in mGluR3) was found to participate in dimeric interfaces identified by simulation (specifically, the (TM1,TM7)/(TM1,TM7) interface; Figure 2-figure supplement 2). Importantly, these SiMPull and computational results do not rule out the possibility that the extracellular end of TM4, TM1 or TM5 contribute to TMD dimerization but they show that these regions are not mediators of the differences between mGluR2 and mGluR3.

While isolated TMDs are very useful for studying TMD behavior directly, we asked if the identified TM4 residues are relevant within the context of full-length mGluRs. We first produced an mGluR2-C121A-3xTM4 construct and examined dimerization compared to mGluR2-C121A and mGluR2-C121A-mGluR3TMD. Consistent with isolated TMD data, we found that the effect of swapping the entire TMD was mimicked by only introducing the 3xTM4 mutant (Figure 2D). This effect was also observed with mGluR3-C127A-3xTM4 where the increase in dimerization matched what was observed for mGluR3-

C127A-mGluR2TMD (Figure 2E). All mutants showed limited effects on receptor expression levels (Figure 2—figure supplement 6A-D).

Together, these experiments and computations show that TM4 residues control the relative strength of interaction between TMDs, at least for mGluR2. Importantly, TMD chimeras or 3xTM4 swap mutations showed no clear effect on dimerization in full-length wild type backgrounds likely due to the maintenance of the disulfide bridge that stabilized LBD dimerization (Figure 2—figure supplement 6E). This indicates that cysteine mutation is needed to reveal the distinct inter-TMD interaction modes that exist within mGluR2 and mGluR3 dimers.

TM4 residues control orthosteric and allosteric activation of group II mGluRs

Having observed a clear, but variable role for inter-TMD interfaces involving the cytosolic end of TM4, we next investigated how this region contributes to mGluR function. We turned to a calcium imaging assay in HEK 293T cells where a G-protein chimera (Conklin et al., 1993) allows $G_{i/o}$-coupled receptors, such as mGluR2 and mGluR3, to produce release of calcium from intracellular stores which can be quantified by measuring the fluorescence increase from a fluorescent calcium sensor such as GCaMP6f (Materials and methods). We started by measuring the glutamate response of wild type mGluR2 and mGluR3. As expected from previous studies (Levitz et al., 2016, Tora et al., 2018), mGluR3 showed a higher apparent glutamate affinity compared to mGluR2 (Figure 3—figure supplement 1A, B). Weakening the TM4 interface in mGluR2-3xTM4 produced a ~4-fold leftward shift compared to wild-type mGluR2 (Figure 3A-C). Based on this result, we wondered whether mGluR3-3xTM4 would have reduced apparent glutamate affinity compared to mGluR3. Indeed, we observed a ~20-fold rightward shift for mGluR3-3xTM4 compared to wild type mGluR3 (Figure 3D-F). To further understand the contribution of each residue, we also tested single mutants. Interestingly, mGluR2-A677S, -A681F, and -A685G did not show different glutamate EC_{50} values compared to wild type mGluR2 (Figure 3C; Figure 3—figure supplement

1C). Conversely, mGluR3-S686A, -F690A, and -G684A all exhibited significant rightward shifts compared to mGluR3, though no single mutant had as reduced apparent affinity as mGluR3-3xTM4 (Figure 3F; Figure 3—figure supplement 1D). Together, these measurements show that inter-TM4 interactions influence orthosteric activation of group II mGluRs.

We also tested glutamate responses of the TM1 (F584I/G587T), TM4 (A695S/A696V) and TM5 (A726S/G730I/A733T) mutants, which showed no change compared to wild-type in dimerization experiments (Figure 2—figure supplement 5). Consistent with their lack of effect on dimerization, both mGluR2-F584I/G587T and mGluR2-A726S/G730I/A733T showed identical concentration response curves compared to wild type mGluR2 (Figure 3C; Figure 3—figure supplement 1E).

Next, we wondered whether the 3xTM4 residues also influence allosteric activation. Our work and others' have demonstrated that PAMs can function as direct agonists of mGluR2 (Gutzeit et al., 2019, El Moustaine et al., 2012, Goudet et al., 2004, O'Brien et al., 2018). We tested the mGluR2 PAM LY487379 (LY48) (Johnson et al., 2003) with mGluR2 and mGluR2-3xTM4. Like the glutamate response, we observed a small leftward shift in EC_{50} for mGluR2-3xTM4 compared to wild type mGluR2 (Figure 3G, Figure 3—figure supplement 1F). We also observed that the mGluR2-3xTM4 LY48 PAM response showed greater maximal efficacy, with saturating (100 μM) LY48 giving ~20% greater amplitude compared to wild type mGluR2. This finding shows that 3xTM4 residues also influence allosteric activation.

Given the clear effects of TM4 perturbations on group II mGluR function, we asked what the effects of harsher alteration of this interface would be. Critically, we wondered if further disruption of the TMD interface would enhance activation or impair it, providing a clue into whether a TM4-containing interface is a necessary intermediate along the activation pathway or merely associated with an inactive state. We introduced bulky, hydrophobic tryptophan residues into outward facing residues of TM4 to disrupt inter-subunit interaction. We first produced mGluR2-3xTM4_W (A677W, A681W, A685W) in the isolated TMD background and observed reduced dimerization compared to both mGluR2-TMD and mGluR2-3xTM4 (Figure 3—figure supplement 1G). In contrast to what was observed with mGluR2-3xTM4, full-

length mGluR2-3xTM4_W showed a small right-shift in the functional calcium imaging concentration response curve (Figure 3H), suggesting that harsh perturbation to the lipid-targeting face of TM4 impairs activation. Consistent with this, mGluR3-3xTMD_W (S686W/F690W/G684W) showed similarly weak dimerization compared to wild type mGluR3-TMD (Figure 3—figure supplement 1G) and a pronounced right-shift compared to wild type mGluR3 in the functional calcium imaging assay (Figure 3I). Together these results confirm the importance of TM4 in group II mGluR TMD dimerization and suggests that, despite the weaker TM4-mediated dimerization of mGluR3, outward-facing residues in TM4 are still important for inter-subunit rearrangement along the activation pathway for both receptor subtypes.

SNAP- and Halo-based FRET sensors enable analysis of the effects of TM4 interface perturbation on conformational dynamics of full-length mGluRs

Having established the role of TM4 residues in influencing dimerization and both orthosteric and allosteric activation, we next wondered how they influence mGluR conformational dynamics using fluorescence resonance energy transfer (FRET). We first examined whether TM4 residues influence inter-LBD dynamics using a well-established assay where a decrease in FRET between N-terminal SNAP-tags is correlated with activation-associated inter-LBD reorientation (Doumazane et al., 2013, Olofsson et al., 2014, Vafabakhsh et al., 2015). HEK 293T cells were transfected with SNAP-tagged mGluR constructs and after labeling with SNAP-reactive donor (BG-LD555) and acceptor (BG-LD655) fluorophores (Materials and methods), the donor fluorophore was excited with a 561 nm laser while donor and acceptor channels were imaged simultaneously with a dual camera imaging system as described previously (Gutzeit et al., 2019). 3xTM4 mutants produced inter-LBD FRET responses that were indistinguishable from their wild-type counterparts with identical glutamate concentration-response curves (Figure 4—figure supplement 1). As previously shown, mGluR3 but not mGluR2 showed a clear basal FRET response to the competitive antagonist LY341495 in the absence of glutamate, consistent with constitutive inter-LBD dynamics that drive basal activity (Vafabakhsh et al., 2015, Levitz et al., 2016). mGluR3-3xTM4

maintained a basal response to LY34 that was indistinguishable from WT, while both mGluR2 and mGluR2-3xTM4 showed no basal response to LY34 (Figure 4—figure supplement 1). Together these data show that 3xTM4 mutants undergo normal LBD motions, suggesting that their functional effects are mediated downstream at the TMDs themselves. Furthermore, this underscores the large effects of the 3xTM4 mutations on receptor activation, given that despite normal glutamate sensitivity at the LBDs apparent glutamate affinities were shifted by up to nearly 20-fold in the case of mGluR3 (Figure 3).

We next sought to directly probe dynamics at the TMD by developing new FRET sensors based on ours and others' previous studies of mGluR1 where insertion of fluorescent proteins (i.e. CFP/YFP) into intracellular loops or C-termini have yielded sensors of activation-associated conformational changes that are suitable for live cell studies (Hlavackova et al., 2012, Marcaggi et al., 2009, Grushevskyi et al., 2019, Tateyama et al., 2004, Tateyama and Kubo, 2006). We re-engineered this approach to incorporate HaloTags (Los et al., 2008) which enable the use of organic fluorophores, such as the family of rhodamine-based Janelia Fluor ("JF") dyes (Grimm et al., 2016, Grimm et al., 2020), which show enhanced brightness and stability compared to fluorescent proteins. We produced constructs where a HaloTag is inserted into the second intracellular loop of mGluR2 or mGluR3 to monitor proximity between TMDs (Figure 4A). Following expression, these constructs were labeled with HaloTag donor (JF_{549}) and acceptor (JF_{646}) dyes at a 1:3 ratio where optimal results were observed (Figure 4—figure supplement 2A). Consistent with prior fluorescent protein-based constructs for mGluR1, glutamate application resulted in a FRET increase for both the mGluR2 and mGluR3 sensors (Figure 4B; Figure 4—figure supplement 2B, C). Importantly, no FRET responses were observed when constructs were labeled with only donor or only acceptor fluorophores (Figure 4-figure supplement 2D, E). FRET responses were reversible upon drug washout and concentration-dependent (Figure 4—figure supplement 3A, B). Concentration response curves for wild-type constructs showed the expected higher apparent affinity for mGluR3 compared to mGluR2 (Figure 4C).

We further characterized the sensitivity of the FRET sensors to different types of compounds. As expected, glutamate responses were fully blocked by the competitive antagonist LY341495 (Figure 4—figure supplement 3C, D) at the same concentration (5 μM) used for block of functional responses (Figure 4—figure supplement 3E, F). We next asked if glutamate-induced FRET increases are blocked by TMD-targeting mGluR NAMs. We focused on the non-specific group II mGluR NAM MNI 137, which (10 μM) was only able to produce a weak, partial block of glutamate-induced FRET responses (~30-50%) (Figure 4D, E; Figure 4—figure supplement 3G) at the same saturating concentration (10 μM) where full block of functional responses was observed (Figure 4E; Figure 4—figure supplement 3H, I). Further raising the MNI 137 concentration to 50 μM (IC_{50} ~10 nM (Hemstapat et al., 2007)) did not increase the extent of block of glutamate-induced mGluR3 FRET responses (42.9 ± 7.4 %, n=8 for 10 μM; 44.9 ± 8.3 %, n=3 for 50 μM). These results indicate that these FRET sensors partially report on conformational changes that are insensitive to NAMs. In addition, we tested a saturating concentration of the mGluR2 PAM LY48 and, in contrast to its robust functional activation properties (Figure 3G), observed weak FRET increases that were ~20-30% of the amplitude of the response to saturating glutamate (Figure 4F). This indicates that the inter-TMD motions detected by the FRET sensor are partially insensitive to allosteric modulators.

Next, we asked if the inter-TMD FRET sensors are sensitive to perturbation to TM4. We found that mGluR2-3xTM4 exhibited a clear leftward-shift compared to mGluR2, while mGluR3-3xTM4 exhibited a rightward-shift compared to mGluR3 (Figure 4G-I), supporting a role for TM4 in controlling intersubunit motions. In addition, mGluR3-3xTM4 exhibited a reduced basal FRET response to LY341495 compared to wild type mGluR3 (Figure 4J, K; Figure 4—figure supplement 3K, L), suggesting that the strengthened TM4 interface is capable of decreasing the basal activity of the receptor. We tested basal receptor activity using a previously described (Gutzeit et al., 2019) GIRK-channel based patch clamp assay and, indeed, observed substantially reduced basal activity for mGluR3-3xTM4 compared to wild type mGluR3 (Figure 4L, M). Interestingly the basal FRET response was larger for LY341495 than MNI 137, despite comparable responses to both antagonists in the patch clamp assay (Figure 4—figure supplement 3J-L), further

supporting the partial sensitivity of the FRET sensor to allosteric compounds. Together these results indicate that orthosteric and allosteric compounds differentially control inter-TMD conformational dynamics and that these dynamics are tuned by a TM4-containing dimer interface.

Testing an inter-TMD rearrangement model of mGluR activation

Previous biochemical and structural studies have strongly argued that TMDs undergo reorientation to a TM6 interface upon activation (Xue et al., 2014, Koehl et al., 2019). Notably, TM6 is highly conserved across mGluR subtypes compared to other transmembrane helices and is 100% identical between mGluR2 and mGluR3 (Figure 2—figure supplement 1). This supports a model where divergent inter-TMD interaction modes across mGluR subtypes in inactive states converge on a common active-state interface. To test this model of mGluR activation, we introduced mutations at the TM6 interface based on the full-length mGluR5 agonist- and PAM-bound cryo-EM structure where a single point of contact exists between TMDs centered on conserved isoleucine 791 (I779 in mGluR2 and I788 in mGluR3) in TM6 (Koehl et al., 2019) (Figure 5A). We first tested alanine (I779A) and tryptophan (I779W) mutants in the isolated mGluR2-TMD to determine if either mutation altered dimerization in SiMPull experiments. Interestingly, both mutants showed ~20% reduced dimerization compared to the wild type mGluR2-TMD (Figure 5—figure supplement 1A-C), suggesting that both TM4- and TM6-containing interfaces contribute to the dimer population in this assay. Mutation to a nearby conserved proline (P778) in the TM6 interface also decreased TMD dimerization (Figure 5—figure supplement 1C) and mutation to the same conserved TM6 residue in mGluR3, I788A, produced a similar decrease in TMD dimerization (Figure 5B).

To determine whether functional differences exist between the mutants, we performed calcium imaging experiments with mutations in the full-length mGluR2 background. mGluR2-I779W, -I779A, and -P778A-I779A all showed right-shifted concentration response curves compared to mGluR2 while mGluR2-P778A was not significantly different but did show a modest left-shift (Figure 5C, E; Figure 5—

figure supplement 1D, E). Similar to mGluR2, mGluR3-I788A showed a ~18-fold rightward shift in glutamate response compared to wild-type (Figure 5D, E; Figure 5—figure supplement 1F), suggesting that this residue indeed plays an important conserved role in group II mGluR activation.

Having confirmed the importance of inter-TM6 interactions to orthosteric activation, we asked if this interface also influences allosteric drug activation. It remains unclear how similar the orthosteric and allosteric activation pathways are given that these ligands bind at very distant sites and are able to activate mGluRs independently of each other. Notably, mGluR2 and mGluR4 PAMs can activate full-length receptors even in the presence of orthosteric antagonists suggesting that LBD-driven re-arrangement can be bypassed by TMD-targeting compounds (Gutzeit et al., 2019, Rovira et al., 2015). We tested the response of mGluR2-I779A to LY48 and found a ~12-fold rightward shift and a ~30% reduction in maximal PAM efficacy compared to saturating glutamate (Figure 5F). Together, these results clearly indicate that TM6 interactions also play a role in allosteric activation.

Next, we asked how weakening the TM6 interface would alter the conformational dynamics detected by our TMD FRET sensors. We introduced the I779A mutation into the mGluR2 inter-subunit FRET sensor and observed a modest right shift in the concentration response curve (Figure 5G; Figure 5—figure supplement 1G). While the functional assay revealed an 18-fold rightward shift for I779A, the change in EC_{50} was only ~2-fold, consistent with this sensor primarily sensing steps in the activation process that occur prior to TM6 interface formation or conformational changes stabilized by the TM6 interface. A similar, small right-shift was observed with the mGluR3 inter-TMD FRET sensor (Figure 5H; Figure 5—figure supplement 1H). Combined, these results underscore the importance of the TM6 interface in the conformational changes that drive group II mGluR activation.

Having determined that both the cytosolic end of TM4 and the extracellular end of TM6 shape the mGluR activation process, we next sought to further clarify the specific role of each region in mediating TMD dimerization with the hypothesis that a TM4 to TM6 interface switch occurs during both orthosteric and allosteric activation. This interface is both based on our data and aforementioned previous cross-linking

and structural studies (Koehl et al., 2019, Xue et al., 2014). We decided to conduct SiMPull experiments on wild-type and mutant receptors in the presence of ligands to investigate effects on receptor dimerization strength.

We previously found that allosteric drugs did not alter the dimerization of the mGluR2 TMD (Gutzeit et al., 2019). However, we anticipated that weakening either the TM4 or TM6 interface (Figure 6A) would sensitize the mGluR2-TMD to shifts in dimerization strength produced by stabilizing distinct states. Indeed, while wild type mGluR2-TMD showed no sensitivity to PAM or NAM treatment, mGluR2-TMD-3xTM4 showed a clear increase in dimerization following treatment with a PAM (TASP) while mGluR2-TMD-I779A showed a clear increase following treatment with a NAM (MNI 137) (Figure 6B; Figure 6—figure supplement 6A-C). This result is consistent with a model where PAM treatment shifts the dimer toward a TM6 interface enabling rescue of weak TM4-mediated dimerization for 3xTM4 whereas NAM treatment shifts the dimer toward a TM4 interface to rescue the weak TM6-mediated dimerization of I779A. Supporting this, simultaneously weakening both interfaces with combination of 3xTM4 and I779A mutations prevented any PAM- or NAM-induced dimerization shifts (Figure 6A, B; Figure 6—figure supplement 1D).

We next conducted the same experiments in the mGluR2-C121A background (Figure 6C) to assess whether this model also described dimer rearrangement for full-length receptors. Similar to the wild-type mGluR2-TMD, mGluR2-C121A dimerization was unchanged by ligands (Figure 6D; Figure 6—figure supplement 1E). However, mGluR2-C121A-3xTM4 showed a clear increase in dimerization following treatment with a PAM or glutamate (Figure 6D; Figure 6—figure supplement 1F) and mGluR2-C121A-I779A showed increased dimerization following treatment with a NAM (Figure 6D; Figure 6—figure supplement 1G). Lastly, mGluR2-C121A-3xTM4-I779A retained reduced dimerization (~45%) with and without all ligands (Figure 6D; Figure 6—figure supplement 1H). Together, these findings support a model of mGluR TMD activation in which TM4 supports the inactive mGluR TMD interface and reorientation to a TM6 interface is required for activation.

Next, we wondered whether the same inactive and active interfaces could be observed for mGluR3. Since mGluR3-C127A already shows reduced dimerization compared to mGluR3 (Figure 6E), we anticipated that the addition of ligands might alter dimerization without further mutation to the TMD. Indeed, addition of LY34 decreased dimerization while addition of glutamate increased dimerization (Figure 6F; Figure 6—figure supplement 1I). Strengthening the TM4 interface in mGluR3-C127A-3xTM4 prevented the ligand-induced effects on dimerization strength (Figure 6F; Figure 6—figure supplement 1J), likely due to a relative balance in dimerization strength between TM4 and TM6 in this construct as is seen with mGluR2. Finally, we tested mGluR3-C127A-I788A and observed a small increase in dimerization following the addition of LY34 and no difference in the presence of glutamate (Figure 6F; Figure 6—figure supplement 1K). Overall, these results establish the combination of drug treatment with single molecule pulldown as a means to assess ligand-induced membrane protein assembly and support a general model of ligand-regulated shift between TM4 and TM6-containing dimer interfaces (Figure 6G).

Inter-TMD interactions fine-tune the assembly of mGluR2/3 heterodimers

An increasingly appreciated aspect of mGluR molecular diversity is the formation of heterodimers which have been shown to have unique pharmacological and functional properties (Levitz et al., 2016, Habrian et al., 2019, Yin et al., 2014, Delgado et al., 2017, Liu et al., 2017, Sevastyanova and Kammermeier, 2014, Werthmann et al., 2020). We recently showed that extensive co-expression of mGluR subtypes occurs throughout the brain and that a complex set of preferences determines the relative propensities for heterodimerization of different mGluR pairs (Lee et al., 2020). Among the most preferred pairs are mGluR2 and mGluR3 which readily form heterodimers following heterologous expression and can be co-immunoprecipitated from the frontal cortex. Given our finding that mGluR2 and mGluR3 homodimers have distinct inter-TMD interaction properties, we asked how this would manifest in the mGluR2/3 heterodimer: Are mGluR2 and mGluR3 TMDs able to interact? Does the TMD-TMD interface resemble mGluR2 or mGluR3 homodimers?

We first performed 2-color SiMPull experiments to determine if the isolated HA-SNAP-mGluR2-TMD construct can pull down CLIP-mGluR2-TMD or CLIP-mGluR3-TMD (Figure 7A). We labeled HA-SNAP-mGluR2-TMD with BG-LD655 (red) and either CLIP construct with BC-DY547 (green) and calibrated surface expression to be comparable between conditions (Figure 7—figure supplement 1A, B), before isolating receptor complexes using the anti-HA antibody (Figure 7A) as was done for previous 1-color experiments. While SNAP-mGluR2-TMD was able to pull-down both constructs, a higher level was observed for CLIP-mGluR2-TMD (Figure 7B), suggesting that TMD heterodimers can form but the inter-TMD interface of mGluR2 homodimers is more stable than that of mGluR2/3 heterodimers. We performed the reverse experiment with HA-SNAP-mGluR3-TMD (Figure 7C) and found higher levels of pulldown for CLIP-mGluR2-TMD compared to CLIP-mGluR3-TMD (Figure 7D), suggesting that the inter-TMD assembly of mGluR3 homodimers is less stable than that of mGluR2/3 heterodimers.

We next investigated inter-TMD interaction of mGluR2/3 homodimers in the full-length context. Consistent with previous work (Lee et al., 2020), at comparable levels of surface-expression, full-length mGluR2 preferentially assembles with mGluR3 (Figure 7E,F; Figure 7—figure supplement 2A,B). However, mutating the intersubunit disulfide-forming cysteine (C121A in mGluR2; C127A in mGluR3) resulted in a dramatic swap of the dimerization preference. HA-SNAP-mGluR2-C121A pulled down CLIP-mGluR2-C121A at nearly wild-type levels, consistent with the minor effect of this mutation on mGluR2 homodimerization (Figure 1D) but pulled down a much lower level of CLIP-mGluR3-C127A (Figure 7E, F). Consistent with isolated TMD results, SNAP-mGluR3-C127A also showed a weak preference for CLIP-mGluR2-C121A over CLIP-mGluR3-C127A (Figure 7G). To test whether inter-TM4 interactions contribute to the distinct assembly properties of mGluR2/3 heterodimers, we introduced the 3xTM4 mutation into CLIP-mGluR3-C127A and observed enhanced pulldown via SNAP-mGluR2-C121A (Figure 7F). While this was unable to rescue mGluR2/3 heterodimerization back to the level of wild-type receptors, this result clearly indicates that this stretch of TM4 is a determinant of the assembly of mGluR2/3 heterodimers. Similarly, introducing the 3xTM4 mutation into CLIP-mGluR2-C121A decreased the

efficiency of pulldown via SNAP-mGluR3-C127A (Figure 7G). Together these data indicate that mGluR2/3 TMD dimers show an intermediate affinity compared to their parent homodimers (Figure 7H), further supporting the TMD dimer interface as a site of structural and functional diversity between mGluR subtypes.

Discussion:

Despite advancements in our understanding of dimeric family C GPCR assembly and activation at the level of the extracellular domains (Ellaithy et al., 2020), it has remained less clear how TMDs interact and rearrange in this process. Our findings provide new insight into the molecular basis of mGluR TMD association and argue for a perspective that takes into account an ensemble of inter-TMD dimerization states that are dynamically populated with distinct occupancies across subtypes.

Our finding that swapping TMDs between mGluR2 and mGluR3 swaps dimerization strength, demonstrates that subtype-specific interactions between TMDs affect full-length mGluR dimer assembly. Furthermore, our discovery that three membrane-facing residues at the cytoplasmic end of TM4 confer differences between mGluR2 and mGluR3 builds on previous reports of TM4 as a putative mGluR2 TMD interface based on cross-linking (Xue et al., 2014, Koehl et al., 2019, Gonzalez-Maeso et al., 2008), while adding a critical new perspective that dimer assembly can vary dramatically within a receptor subfamily and even between two closely related receptors with >70% sequence identity. The conserved triple alanine motif in TM4 of mGluR2 and the corresponding differences in mGluR3 raise questions about the mechanism by which these residues contribute to TMD dimerization strength. Alanine is a small, nonpolar amino acid which has been demonstrated to display a preference to be buried when in an alpha-helical transmembrane helix (Ulmschneider and Sansom, 2001) and can contribute to tight helix-helix packing due to its short side chain (Senes et al., 2000, Eilers et al., 2000). For example, in potassium channels, alanine has the most frequent occurrence at helix interfaces (Javadpour et al., 1999). Conversely, the mGluR3 TM4-

containing dimer region corresponding to the conserved triple alanine motif in mGluR2 TM4 includes serine, phenylalanine, and glycine residues. The hydrophobic and bulky nature of phenylalanine makes this residue less favorable for close helix-helix packing in membrane proteins (Eilers et al., 2000). Serine has been found to contribute to transmembrane packing, although less so than alanine (Eilers et al., 2000) and its polarity and position enable cytosol-facing orientations as seen in our mGluR3 homology model (Figure 2A). Glycine, the smallest amino acid due to its lack of a side chain, often occurs at helix-helix interfaces in transmembrane regions (Senes et al., 2000). However, biochemical experiments in a model transmembrane helix and molecular dynamics simulations have argued that glycine is helix destabilizing in membrane proteins as it can induce local flexibility (Dong et al., 2012, Högel et al., 2018). Such helix destabilization may impair formation of stable intersubunit interfaces for mGluR3.

Our data on mGluR2/3 heterodimer assembly (Figure 7) confirms the dominant role of inter-LBD interfaces in determining relative dimer propensities (Levitz et al., 2016, Lee et al., 2020). However, the dramatic effect of disruption of inter-subunit disulfide bonds reveals an unexpected critical role for this covalent linkage in determining the enhanced assembly of mGluR2/3 heterodimers compared to mGluR2 homodimers. TM4 interfaces are a clear contributor to the assembly of mGluR2/3 heterodimers with stronger interaction observed for heterodimers compared to mGluR3 homodimers and weaker interaction compared to mGluR2 homodimers. This likely shapes the activation properties of this complex which we have previously shown to have intermediate glutamate affinity, basal activity and cooperativity compared to parent homodimers (Levitz et al., 2016). The considerable variability observed within TM4 and other helices across group I and group III mGluRs (Figure 2—figure supplement 1) suggests that further complexity likely exists in TMD dimerization beyond the group II subtypes. We've previously shown that mGluR2 TMD dimerization is stronger than that observed for both mGluR1 and mGluR5 (Gutzeit et al., 2019) which is in line with the lack of an inter-TMD interface in the inactive, antagonist-bound mGluR5 cryo-EM structure (Koehl et al., 2019). Consistent with this, only mGluR2 shows the triple alanine motif

at the bottom half of TM4 suggesting that while TM4 interfaces may contribute to dimerization across all subtypes, mGluR2 maintains uniquely strong constitutive interactions between TMDs.

Most importantly, our study provides new insight into the role of inter-TMD interaction in the activation of mGluRs. While strengthening the TM4 interface hinders receptor activation and inter-TMD re-arrangement, weakening the TM4 interface has more complex effects that can either enhance activation, in the case of 3xTM4 on mGluR2, or impair activation, in the case of harsher tryptophan mutants (Figure 3, 4). Based on these results we anticipate that outward-facing residues in TM4 can both stabilize inactive states, as seen in wild-type mGluR2 and a previous study where TM4/TM5 crosslinking impaired receptor activation (Xue et al., 2014), but can also contribute to the receptor activation pathway. Such observations are in-line with the MSM analysis of our CG MD simulations, which reveals many distinct modes of TM4-based dimerization, including those that engage helices other than TM4, and especially TM1. It's possible that distinct modes are associated with inhibited inactive states while others are likely to be intermediates along an activation pathway that converges on TM6 interfaces. Notably, the MSM analysis of mGluR2 reveals a direct reactive flux between the identified macrostate of TM4-containing dimers and the macrostate containing TM6-containing helices, whereas equivalent macrostates identified for mGluR3 are only indirectly connected. Most clearly, our ligand coupled SiMPull analysis (Figure 6), strongly supports a TM4 to TM6 re-arrangement along the activation pathway with both orthosteric and allosteric agonists favoring a TM6 interface while antagonists stabilize a TM4 interface. It's notable that TM6-containing interfaces are formed with much lower probability with respect to others in our inactive-state MD simulations, suggesting that an active TMD and/or active LBDs are required to engage this interface. Finally, TM1 interfaces are prominent in our MD simulations, with TM1-containing dimers being among the most probable configurations alongside TM4-containing dimers. While our computations suggest that TM1 is involved in a variety of kinetically inter-changeable asymmetric dimers, TM1 interfaces could also be relevant for higher order oligomers, as proposed for mGluR2 in neurons (Møller et al., 2018).

Taking into consideration the results of this study along with existing literature, we have illustrated a working 4-state model of mGluR activation at the level of the TMDs (Figure 8A). While our MSM analysis suggests that many microstates likely contribute to the activation pathway, this simplified model proposes that TMDs transition between a monomeric assembly, TM4-containing dimer assemblies and a TM6-containing active dimer interface that transitions to an active TMD conformation stabilized by agonists, PAMs and G proteins. Notably, the highly probable TM4-containing dimer macrostates and the least probable TM6-containing macrostates of inactive mGluR2 and mGluR3 appear to be connected both directly and indirectly by reactive fluxes. In the first step of our proposed 4-state model of mGluR activation, monomeric TMDs are able to associate to form dimers via TM4-containing interfaces. In the case of mGluR2, such TM4-containing interfaces are considerably more stable than in mGluR3 with mGluR2/3 showing an intermediate level (Figure 8B), based on SiMPull measurements (Figure 1, 2) and the larger FRET change observed with the mGluR3 inter-TMD FRET sensor (Figure 4). Following TM4 dimer formation, a dimer reorientation step enables the formation of a TM6 interface. We hypothesize that the intersubunit FRET sensors are likely able to sense a mix of step 1 and step 2. Based on the fast transitions previously observed with similar inter-TMD FRET sensors on the same ~1-10 ms timescale as inter-LBD rearrangement (Grushevskyi et al., 2019, Hlavackova et al., 2012, Olofsson et al., 2014), the first transition is likely driven by the agonist-induced relaxed to active LBD transition where the intermediate cysteine-rich domains (CRDs) come into closer proximity (Koehl et al., 2019, Huang et al., 2011, Liauw et al., 2021). Given the partial sensitivity of the intersubunit FRET sensors to NAMs and PAMs, we propose that step 1 is largely insensitive to allosteric drugs which primarily control the reorientation between TM4 and TM6 interfaces. This is in line with our previous mGluR2 inter-TMD FRET measurements with isolated domains where changes in FRET but not monomer: dimer equilibrium were observed with PAMs and NAMs (Gutzeit et al., 2019). One possibility not explicitly acknowledged in our model is that there may be transitions directly from a monomeric TMD state to the active TM6 interface. However, the impaired activation observed with mGluR3-3xTM4_W suggests that some form of TM4 interaction is part of the activation pathway. Along these lines, the proposed metastability of TM4 interfaces may explain why they

have not yet been observed in static structures solved by crystallography or cryo-EM, although our steering simulations suggest that symmetric TM4-containing dimers should be relatively stable in the full-length mGluR2. However, the clear effect of perturbing this interface and the subtype differences suggest that it may be a potential target for specific and potent drugs. Intriguingly, inter-TMD PAM and NAM binding has recently been observed in cryo-EM structures of $GABAB_{RS}$ (Mao et al., 2020, Shaye et al., 2020), indicating that TMD interfaces may be druggable sites across family C GPCRs.

Our model posits that TMD dimer rearrangement precedes the intra-TMD conformational changes that drive G protein activation. This is consistent with our previous studies of mGluR1 where intersubunit FRET sensors show faster (1 ms) FRET changes compared to intrasubunit sensors (~10-20 ms) (Grushevskyi et al., 2019, Hlavackova et al., 2012). Following dimer rearrangement, an intra-TMD conformational step is likely required to enable receptor activation. Furthermore, we anticipate that the transition between inactive and active TMD conformations is likely stabilized by G proteins (Figure 8C), as has been reported for family A GPCRs (Nygaard et al., 2013, Manglik et al., 2015, Rasmussen et al., 2011, Weis and Kobilka, 2018). The lack of such stabilization by G proteins likely explains why the intra-subunit TMD conformation in agonist, PAM and allosteric nanobody-bound mGluR5 cryo-EM structure is very similar to the TMD conformation seen in the apo state (Koehl et al., 2019).

It's important to note that alternative activation pathways may be reasonably proposed. For example, given that PAMs can activate isolated monomeric mGluR2 (El Moustaine et al., 2012) and a previous study showed only modest inhibition of PAM responses in a TM4/TM5-crosslinked mGluR2 (Xue et al., 2014), it's possible that allosteric activation can proceed without inter-TMD interaction. However, the clear effects of TM4 and TM6 interface mutations on PAM responses in our study (Figure 3, Figure 6), indicate that this is likely not the typical pathway taken. In addition, it is difficult to distinguish between a "rolling" dimer interface model where many dimeric microstates exist *en route* to a TM6 interface versus a dynamic association/re-association model where TM4 interfaces are fully broken prior to reformation of a TM6-containing active interface. However, both our MSM analysis of the MD simulations and prior

crosslinking studies suggest that macrostates of TM4- and TM6-containing dimers are kinetically connected which favors the former interpretation. Overall, this model is meant to provide a framework for thinking about the possible routes of activation but higher resolution structural and, especially, computational and spectroscopic measurements will be needed to decipher the complex activation dynamics of different homo- and hetero-dimeric mGluR subtypes. Of critical importance is understanding how the molecular motions of the LBDs and CRDs on the millisecond and sub-millisecond timescales are transmitted to the many micro- and macro-states of the TMDs.

What is the biological relevance of the modulatory effects of TMD dimerization differences between subtypes? The variable strength of the TM4 interface likely contributes to the tuning the mGluR activation dynamics to the synaptic roles of each particular subtype. The ~3-20-fold shifts in apparent glutamate affinity observed when swapping residues between mGluR2 and mGluR3, while subtle, are highly relevant in the context of the spatiotemporally complex dynamics of synaptic and extra-synaptic glutamate (Reiner and Levitz, 2018). Our data also suggest that in addition to controlling apparent glutamate sensitivity, relative inter-TMD dimerization strength tunes the basal activity, and likely also shapes the signaling kinetics of different mGluRs. Outside of the mGluR homo- and hetero-dimer context, the proposed inactive TM4 interface is intriguing to consider in the context of the mGluR2-5HT$_{2A}$R interaction, which was reported to require the same three alanine residues for heterocomplex formation (Moreno et al., 2012, Moreno et al., 2016). Our working model suggests that formation of this heterocomplex would either require activation of mGluR2 to induce TMD reorientation away from a TM4 mGluR interface or stabilization of a state where TMD dimers are unable to interact. In line with this hypothesis, previous work found that co-expression of mGluR2 and 5-HT$_{2A}$R increased glutamate-elicited G$_{i/o}$ activation (Fribourg et al., 2011). More work will be required to fully understand this unique inter-family interaction and if such inter-TMD interactions occur beyond the prototypical mGluR2-5HT$_{2A}$R complex.

Materials and methods:

Cell culture, molecular cloning and gene expression

HEK 293T cells were purchased from ATCC and validated by DNA profiling (Bio-Synthesis, Inc). They tested negative for mycoplasma using a commercial kit. The cells were cultured in DMEM with 5% FBS on poly-L-lysine-coated glass coverslips. Lipofectamine 2000 (Thermo Fisher) was used for transfection of DNA plasmids. For single-molecule pulldown (SiMPull) experiments, cells were transfected with 0.7 µg DNA of HA- and SNAP-tagged receptor constructs. For calcium imaging experiments, cells were transfected with the mGluR of interest, a $G\alpha_{qi3}$ chimera (Conklin et al., 1993) and GCaMP6f, in a 7:5:3 ratio with 0.7 µg of receptor. For FRET experiments, cells were transfected with either 0.7 µg SNAP-tagged constructs or 0.7 µg HaloTag constructs. For inter-TMD FRET experiments, HaloTags were inserted in ICL2 at an identical position in both mGluR2 and mGluR3 (directly following I669 in mGluR3 and I660 in mGluR2). An alanine-serine linker precedes the HaloTag and a leucine-glutamatic acid linker follows it. SNAP-mGluR-TMD clones were made as described in (Gutzeit et al., 2019). All mutations were made using standard PCR-based techniques. TMD swap chimeras were made using Gibson assembly (Gibson et al., 2009). For mGluR3-mGluR2TMD, Q558 to P821 of mGluR2 was inserted into mGluR3 between P556 and Q831. For mGluR2-mGluR3TMD, E567 to P830 of mGluR3 was inserted into mGluR2 between P835 and Q800.

Single-molecule pulldown and subunit counting

Single-molecule pulldown (SiMPull) was performed as previously described (Levitz et al., 2016). Briefly, flow chambers were prepared with mPEG-passivated glass slides and coverslips doped with ~1% biotinylated mPEG to prevent non-specific sticking of proteins. Preceding each experiment, chambers were incubated with 0.2 mg/mL NeutrAvidin (ThermoFisher) for two minutes followed by 10 nM of a biotinylated anti-HA antibody (abcam ab26228) for 20-30 min. Following each conjugation step, chambers were washed with T50 buffer (50 mM NaCl, 10 mM Tris, pH = 7.5).

24-48 hours after transfection of HEK 293T cells, the cells were labeled with 1.5 μM benzylguanine (BG)-LD555 (Gutzeit et al., 2019) (Qinsi et al., 2017) or SNAP-Surface Alexa Fluor 546 (New England BioLabs) in extracellular solution at 37°C for 45 minutes. After labeling, cells were washed in extracellular solution to remove excess dye. Next, cells were transferred to Ca^{2+}-free PBS for 20 minutes to dissociate cells from coverslips. Cells were then completely removed from coverslips by gentle pipetting. Centrifugation was used to pellet cells (16,000 g for 1 minute) before lysis in buffer containing 10 mM Tris, 150 mM NaCl, 1 mM EDTA, protease inhibitor cocktail, and 1.2% IGEPAL (Sigma), pH = 8.0. After 1 hour of lysis at 4°C, cells were centrifuged at 16,000 g for 20 minutes. Next, the supernatant was collected and kept on ice. During experiments, the cell lysate was diluted in a 0.1% detergent dilution buffer to achieve sparse immobilization of fluorophore-labeled protein on the passivated slide. Protein was added to the slide until an optimal density was reached and then the flow chamber was washed with dilution buffer to remove unbound protein. For experiments with ligands, drugs were added to cells after dye labeling (during dissociation step in Ca^{2+}-free PBS) and maintained throughout the entire experiment at saturating concentration.

Single molecule imaging was conducted with a 100x objective on an inverted microscope (Olympus IX73) in total internal reflection fluorescence (TIRF) mode. Movies were recorded with a scMOS camera (Hamamatsu ORCA-Flash4v3.0) at 20 Hz with 50 ms exposure. The fluorophores were excited with a 561 nm laser. Multiple independent experiments were performed for each condition tested, including at least two separate transfections and protein preparations. LabVIEW was used for data analysis as previously described (Ulbrich and Isacoff, 2007).

Sequence Conservation Analysis

mGluR amino acid sequences were obtained from UniProt and aligned using the Multiple Sequence Alignment tool from Clustal Omega. Conservation is defined by the chemical characteristics of the amino acid side chain (R group): aliphatic (glycine, alanine, valine, leucine, isoleucine); hydroxyl or sulfur-containing (serine, cystine, threonine, methionine); cyclic (proline); aromatic (phenylalanine, tyrosine,

tryptophan); basic (histidine, lysine, arginine); acidic and their amides (aspartate, glutamate, asparagine, glutamine).

Homology modeling

An initial model of the transmembrane domain of inactive rat mGluR2 was obtained by homology modeling using the MODELLER 9.19 software (Sali and TL, 1993) and the 2.2 Å X-ray crystal structure of inactive mGluR5 (PDB ID: 6FFI (Christopher et al., 2019)) as a structural template. Missing atomic coordinates of extracellular loop 2 (EC2; residues 707-710 of rat mGluR2) were taken from PDB ID 6FFH (Christopher et al., 2019) whereas missing atomic coordinates of intracellular loop 2 (IC2; residues 669-674 of rat mGluR2) were generated *ab initio* and selected according to the lowest MODELLER DOPE score (Shen and Sali, 2006). To minimize differences in the modeled IC2 region between mGlu2 and mGluR3, an inactive rat mGluR3 homology model was obtained using the aforementioned mGluR2 model as a structural template and the Prime 5.9 software (Jacobson et al., 2002, MP et al., 2004).

Coarse-grained molecular dynamics simulations

Coarse-grained (CG) representations of mGluR2 and mGluR3 inactive models were obtained using the *martinize.py* script within the MARTINI 2.2 force field (de Jong et al., 2013). To preserve the tertiary structure of the two receptors, an elastic network was applied to pairs of backbone beads whenever the distance between the pairs was smaller than 0.9 nm. A larger force constant of 1000 kJ mol^{-1} nm^{-2} was applied to pairs of beads within helical secondary structures whereas loop regions were kept more flexible with a force constant of 250 kJ mol^{-1} nm^{-2}. Two CG copies of the same receptor were placed in a 15 × 15 × 11 nm^3 simulation box at a distance of 4.5 or 5.5 nm from each other. Each protomer was then rotated randomly around the axis perpendicular to the membrane plane (z-axis) to generate multiple starting configurations of neighboring protomers. Each pair of protomers was then embedded in a POPC membrane (~635 lipids) and solvated with water molecules and NaCl (0.15 M plus neutralizing ions) using the INSert

membrANE (*insane*) method (Wassenaar et al., 2015). In total, 90 systems were generated for mGluR2 and 92 for mGluR3.

Each system was energy minimized and then equilibrated in five steps. First, a 400 ns MD simulation was run using position restraints on the backbone beads of the receptor with a force constant of 1000 kJ mol^{-1} nm^{-2}. Four additional equilibration steps followed, each of which ran for 60 ns and with position restraints applied with decreasing force constants of 500, 100, 50 and 10 kJ mol^{-1} nm^{-2}, respectively. These MD equilibration simulations used the velocity-rescale thermostat (Bussi et al., 2007) and the Berendsen algorithm (Eslami et al., 2008) to maintain constant temperature at 310 K and pressure at 1 bar, respectively. Production MD runs of 3 or 6 μs (depending on the shorter or longer distance between protomers in the initial configuration) for each system, amounting to 450 μs of simulation time for mGluR2 and 462 μs for mGluR3, were then carried out in the NPT ensemble at 310K and 1 bar using the velocity-rescale thermostat (Bussi et al., 2007) and the Parrinello-Rahman pressure coupling scheme (Parrinello and Rahman, 1998) respectively and using an integration timestep of 30 fs. The Coulombic and van der Waals interactions both were set to decay to zero between 0 and 1.2 nm (Coulombic) and 0.9 and 1.2 nm (van der Waals). All simulations were performed using the GROMACS 2020.4 software package.

Markov State Model Analysis

The relative position of two protomers of mGluR2 or mGluR3 was characterized by calculating the number of residues in each helix and loop on one protomer formed with the other protomer. Contacts were defined by a cutoff of 10 Å on the minimal distance over the beads of the residue. Each simulation frame was then classified using a label that contained the domain names of each protomer that formed more than 20 contacts with the other protomer. This classification yielded ~2,400 and ~1,700 microstates for the mGluR2 and mGluR3 simulations, respectively. Trajectory frames thus clustered were used to estimate a MSM with a lag time of $\tau = 20$ ns, identified after inspecting the change of the transition matrix eigenvalues for increasing lag times. The resulting transition matrix was used in the PCCA+ algorithm (Röblitz and Weber, 2013) to aggregate the microstates into a number of putative biologically relevant macrostates identified by

a gap in the characteristic relaxation timescales. Macrostate equilibrium probabilities $\pi_I = \sum_{i \in I} \pi_i$ were calculated summing the probabilities of the corresponding microstates. To label each macrostate, we calculated the probability that each helix be at the interface by summing the conditional probabilities that a helix D is present for protomer α in the label $\ell_i^{(\alpha)}$ of a microstate i in the macrostate I:

$$p(D, \alpha, I) = \sum_{i \in I, D \in \ell_i^{(\alpha)}} \frac{\pi_i}{\pi_I}$$

Helices with a probability of at least 40% to be at the interface were reported in the macrostate label. Coarse-grained reactive flux between pairs of macrostates was calculated using Transition Path Theory, aggregating asymmetric macrostates that correspond to the same interface but with swapped protomers. I supplemental table XX, microstates were aggregated if (a) their labels $\ell_i^{(\alpha)}$ contained the same helices, but different loops, and (b) their labels were equivalent after swapping protomers, i.e., $\ell_i^{(\alpha)} = \ell_j^{(\beta)}$ and $\ell_i^{(\beta)} = \ell_j^{(\alpha)}$. Macrostate contact matrices between domain D on the first protomer and D' on the second protomer $\langle C_{DD'} \rangle_I = \sum_i \rho_i(I) \langle C_{DD'} \rangle_i$ were calculated by averaging the microstate contacts using the PCCA+ cluster memberships ρ. Contact probabilities between each microstate were defined as averages over the microstate frames using a cutoff of 0.9 nm. Fitting of the Markov Models was carried out using the pyEmma library, version 2.5.7 (Scherer et al., 2015).

Steered molecular dynamics simulations

A model of the dimeric full-length inactive rat mGluR2 was generated by homology modeling using the MODELLER 9.19 software (Sali and TL, 1993). The 4 Å electron microscopy structure of inactive mGluR5 (PDB ID: 6N52 (Christopher et al., 2019)) was used as a template for the extracellular domain (ECD) and extracellular loop 2. The rest of the TMD was modeled based on the 2.2 Å X-ray crystal structure of inactive mGluR5 (PDB ID: 6FFI (Christopher et al., 2019)) or generated *ab initio* (IC2), similarly to what was done for the TMD models. Just as for the aforementioned TMD systems, a homology model of inactive rat

mGluR3 was obtained using the dimeric full-length mGluR2 model as a structural template and the Prime 5.9 software (Jacobson et al., 2002, MP et al., 2004).

As reported for the TMD-only models, CG representations of mGluR2 and mGluR3 full-length models were obtained with the *martinize.py* script within the MARTINI 2.2 force field (de Jong et al., 2013) and the same criteria for the elastic network was enforced to preserve the tertiary structure of the receptors. The full-length dimers were placed in a 1000 × 1000 × 1000nm^3 simulation box, respectively, and minimized in gas phase with a pseudo-PBC approach (Konermann et al., 2018). Briefly, non-bonded interactions were calculated using periodic boundary conditions and the Verlet neighbor search scheme, with the Coulomb and Lennard-Jones cutoffs set to 333.3 nm. To preserve the ECD dimeric interface configuration and its orientation relative to the TMD, additional positional restraints were imposed on the LBD (1000 kJ mol^{-1} nm^{-2} on the x-, y-, and z-coordinates), the CRD (100 kJ mol^{-1} nm^{-2} on the z-coordinates), and the TMD (100 kJ mol^{-1} nm^{-2} on the z-coordinates).

Target configurations for the steered simulations were generated from the most probable dimers identified by the MSM analysis of the TMD-only simulations. Pairwise receptor configurations containing a given dimeric interface in the TMD systems were clustered based on the root mean squared deviation (RMSD) of the participating domains. The least different configurations from all the others for a particular interface was used as a reference to align the protomers of the full-length homology models, so that they could be used as target structures. Steered MD simulations were carried out using the GROMACS 2020.4 software package patched with PLUMED 2.7 (Tribello et al., 2014). Starting from the full-length homology models, the systems were steered over 5,000 steps with a spring constant of 750 kJ mol^{-1} nm^{-2} for the harmonic potential pulling the system along a collective variable defined by the RMSD of the transmembrane backbone beads to the target structures, using the `MOVINGRESTRAINT` algorithm in PLUMED. In total, 30 steered simulations were carried out for each interface. Relative free energy estimates were calculated by comparing the work obtained applying Jarzynski's equality (Jarzynski, 1997) to the different simulations.

Calcium Imaging

24-48 hours after transfection, cells were imaged at room temperature in extracellular solution composed of 135 mM NaCl, 5.4 mM KCl, 2 mM $CaCl_2$, 1 mM $MgCl_2$, 10 mM HEPES, pH = 7.4. Experiments were conducted on an inverted microscope (Olympus IX73) and imaged with a 20x objective. A continuous gravity-driven perfusion was used throughout the entirety of experiments. GCaMP6f was excited using a 488 nm laser and movies were recorded using a scMOS camera (Hamamatsu ORCA-Flash4v3.0) at 1 Hz with a 100 ms exposure time. Olympus cellSens software was used to select regions of interest (ROIs) (representing single cells or small clusters of 2-3 cells) and subsequent data analysis was performed in Microsoft Excel, in which fluorescence intensities were normalized to a baseline of extracellular solution without drug. ~30 ROIs were analyzed per movie. Glutamate responses were quantified by comparing the response to saturating (1 mM) glutamate. PAM responses were also quantified relative to 1 mM glutamate responses. Concentration-response curves were fit using Graphpad Prism. Multiple independent experiments were performed for each construct tested, including at least two separate transfections.

Live-cell FRET measurements

24-48 hours after transfection, cells were washed in extracellular solution containing 135 mM NaCl, 5.4 mM KCl, 2 mM $CaCl_2$, 1 mM $MgCl_2$, 10 mM HEPES, pH = 7.4. For inter-LBD FRET experiments, cells were labeled with 1 μM benzylguanine LD555 and 3 μM benzylguanine LD655 (diluted in extracellular solution). For inter-TMD FRET experiments with HaloTag constructs, cells were labeled with 1 μM JF 549 and 3 μM JF 646 (diluted in extracellular solution). All conditions were labeled for 45 minutes at 37 °C. Following labeling, coverslips were washed in extracellular solution to remove excess dye. Next, coverslips were imaged with a 60x objective on an inverted microscope (Olympus IX73). The donor fluorophore was excited with a 561 nm laser and images were recorded at the same time in both donor and acceptor channels on distinct scMOS cameras (Hamamatsu ORCA-Flash4v3.0) at 0.5-1 Hz with an exposure time of 100 ms. ImageJ was used to analyze cell clusters and FRET was calculated as FRET = $(I_{Acceptor})/(I_{Donor} + I_{Acceptor})$, in which I = fluorescence intensity. Analysis was restricted to relative FRET changes between drug

applications rather than absolute FRET values. For each individual trace, FRET was normalized to the basal FRET value observed before drug treatment. For glutamate concentration-response curves, FRET changes were calculated by normalizing to saturating glutamate applied in the same recording. For all concentration-response curves, data was obtained from multiple cell clusters and averaged from at least two separate experiments. All concentration-response curves were fit using Prism (Graphpad). For basal activity measurements, FRET responses to saturating (5 μM) LY34 were normalized to saturating (100 μM) glutamate. A gravity-driven perfusion system was used to deliver drugs diluted in extracellular solution and all experiments were performed at room temperature.

Patch Clamp Electrophysiology

Whole cell patch clamp recordings from HEK 293T cells co-transfected with GIRK channels were performed as previously described (Gutzeit et al., 2019).

Acknowledgements

We thank Melanie Kristt for technical assistance and Drs. Jeremy Dittman & Anant Menon for helpful discussion and Dr. Scott Blanchard for sharing critical reagents. JKT is supported by an NSF Graduate Research Fellowship under grant 1746886. JL is supported by an R35 grant (R35 GM124731) from NIGMS and the Rohr Family Research Scholar Award. Computational work was supported by National Institutes of Health grant DA038882 (to MF and ML). Simulations were run on resources available through the Office of Research Infrastructure of the National Institutes of Health under award numbers S10OD018522 and S10OD026880, as well as the Extreme Science and Engineering Discovery Environment under MCB080077, which is supported by National Science Foundation grant number ACI-1548562.

Figure Legends:

Figure 1. mGluR2 and mGluR3 transmembrane domains show different dimerization propensities in a single molecule pulldown assay

(A) Left, cartoons of SNAP-mGluR2-TMD (top) and SNAP-mGluR3-TMD (bottom) labeled with fluorophore LD555. Right, representative images showing expression and surface labeling of SNAP-mGluR2-TMD (top) and SNAP-mGluR3-TMD (bottom) in HEK 293T cells before lysis.
(B) Top, schematic showing the SiMPull setup. Bottom, representative image of single molecules with representative fluorescence time course for an individual protein complex (red circle) demonstrating two-step photobleaching. Scale bar = 10 μm.
(C) Histogram summarizing the photobleaching step distribution for SNAP-mGluR2-TMD (n = 1,598 total spots from 14 movies) and SNAP-mGluR3-TMD (n = 1,435 total spots from 10 movies). Dashed line on both histograms indicates SNAP-mGluR2-TMD photobleaching step distribution.
(D) Bar graph showing the percentage of spots bleaching in two steps for SNAP-tagged constructs. * indicates statistical significance (unpaired t-tests; for mGluR3 vs. mGluR2-TMD, p = 1.9E-5; for mGluR2-TMD vs. mGluR3-TMD, p = 1.1E-10; for mGluR3-TMD vs. β2AR, p = 2.4E-8). mGluR2 is not significantly different from mGluR3 (unpaired t-test, p = 0.15).
(E) Bar graph showing the percentage of spots bleaching in two steps for SNAP-tagged constructs. * indicates statistical significance (unpaired t-tests; for mGluR2 vs. mGluR2-C121A, p = 0.010; for mGluR3 vs. mGluR3-C127A, p = 4.8E-9).
(F) Bar graph showing the percentage of spots bleaching in two steps for SNAP-tagged constructs. * indicates statistical significance (unpaired t-tests; for mGluR2-C121A vs. mGluR2-C121A-mGluR3TMD, p = 4.3E-4; for mGluR3-C127A vs. mGluR3-C127A-mGluR2TMD, p = 1.5E-6). Shaded bars indicate data repeated from Figure 1E.
(G) Schematic illustrating the effect of inter-TMD interactions in mGluR2 and mGluR3 dimer assembly.
Number of movies analyzed for each condition is shown in parenthesis above each bar. Error bars are s.e.m.

Figure 2. Residues in TM helix 4 mediate differences in inter-TMD interaction between mGluR2 and mGluR3
(A) Homology models of the TMD of mGluR2 (purple) and mGluR3 (grey) showing TM4 (cyan) residues of interest in magenta.
(B) TM4 sequence alignment for mGluR2 and mGluR3.
(C) Bar graph showing the percentage of spots bleaching in two steps for SNAP-tagged TMD constructs. * indicates statistical significance (unpaired t-tests; for mGluR2-TMD vs. mGluR2-TMD-3xTM4, p = 9.5E-6; for mGluR3-TMD vs. mGluR3-TMD-3xTM4, p = 1.0E-5).
(D) Bar graph showing the percentage of spots bleaching in two steps for SNAP-tagged full-length constructs. * indicates statistical significance (unpaired t-test, p = 7.6E-5). SNAP-mGluR2-C121A-mGluR3TMD is not significantly different from SNAP-mGluR2-C121A-3xTM4 (unpaired t-test, p = 0.85). Shaded bars show repeated data from Figure 1D-E.
(E) Bar graph showing the percentage of spots bleaching in two steps for N-terminally SNAP-tagged constructs labeled with LD555. * indicates statistical significance (unpaired t-test, p = 0.00013). SNAP-mGluR3-C127A-mGluR2TMD is not significantly different from SNAP-mGluR3-C127A-3xTM4 (unpaired t-test, p = 0.30). Shaded bars show repeated data from Figure 1D-E. Number of movies analyzed for each condition is shown in parenthesis above each bar. Error bars are s.e.m.

Figure 3. Differences in TM4 residues mediate different activation properties of mGluR2 and mGluR3
(A) Representative calcium imaging trace showing calcium responses induced by glutamate application from a HEK 293T cell expressing mGluR2-3xTM4, a G protein chimera and GCaMP6f.

(B) Glutamate calcium imaging concentration response curves for mGluR2 (EC_{50} = 1.68 ± 0.03 μM) and mGluR2-3xTM4 (EC_{50} = 0.41 ± 0.06). All values are normalized to saturating (1 mM) glutamate. * indicates statistical significance (two-way ANOVA, p = 5.2E-10).
(C) Summary of glutamate EC_{50} shifts relative to wild type mGluR2 obtained for mGluR2 mutants. * indicates statistical significance (two-way ANOVA; for mGluR2 vs. mGluR2-3xTM4, p = 5.2E-10). "TM1" = F584I, G587T; "TM5" =A726S, G730I, A733T
(D) Representative calcium imaging trace showing calcium responses from mGluR3-3xTM4.
(E) Glutamate calcium imaging concentration response curves for mGluR3 (EC_{50} = 0.56 ± 0.06) and mGluR3-3xTM4 (EC_{50} = 11.0 ± 0.1). All values are normalized to saturating (1 mM) glutamate. * indicates statistical significance (two-way ANOVA, p = 3.6E-10).
(F) Summary of glutamate EC_{50} shifts relative to wild type mGluR3 obtained for mGluR3 mutants. * indicates statistical significance (two-way ANOVA; for mGluR3 vs. mGluR3-S686A, p = 2.2E-8; for mGluR3 vs. mGluR3-F690A, p = 2.6E-14; for mGluR3 vs. mGluR3-G694A, p = 4.8E-10; for mGluR3 vs. mGluR3-3xTM4, p = 3.6E-10).
(G) LY48 calcium imaging concentration response curves for mGluR2 (EC_{50} = 0.45 ± 0.10) and mGluR2-3xTM4 (EC_{50} = 0.27 ± 0.06). mGluR2-3xTM4 has ~17% greater efficacy than mGluR2 at saturating LY48. All values are normalized to saturating (1 mM) glutamate. * indicates statistical significance (two-way ANOVA, p = 1.3E-7).
(H) Glutamate calcium imaging concentration response curves for mGluR2 and mGluR2-3xTM4_W (EC_{50} = 9.01 ± 0.08). All values are normalized to saturating (1 mM) glutamate. * indicates statistical significance (two-way ANOVA, p = 0.00087).
(I) Glutamate calcium imaging concentration response curves for mGluR3 and mGluR3-3xTM4_W (EC_{50} = 186.00 ± 0.27). All values are normalized to saturating (1 mM) glutamate. * indicates statistical significance (two-way ANOVA, p = 1.2E-10).

Figure 4. An inter-TMD FRET assay enables detection of inter-TMD conformational dynamics in full-length mGluR2 and mGluR3 in live cells
(A) Top, schematic showing an mGluR2 dimer with a HaloTag inserted into intracellular loop 2 (ICL2). and labeled with donor and acceptor fluorophores. Bottom, representative cell images showing donor and acceptor channels after donor excitation with a 561 nm laser. Scale bar = 20 μm.
(B) Representative FRET trace showing donor and acceptor fluorescence intensity (top) during glutamate application. A corresponding normalized FRET trace (bottom) shows reversible FRET increases upon glutamate stimulation.
(C) Glutamate FRET concentration response curves for mGluR2 (EC_{50} = 15.75 ± 0.04) and mGluR3 (EC_{50} = 0.23 ± 0.08). All values are normalized to saturating (1 mM) glutamate.
(D) Application of the negative allosteric modulator MNI 137 partially blocks glutamate-induced FRET increases for mGluR2.
(E) Quantification of saturating LY34 (5 μM) and MNI (10 μM) blockade of glutamate responses in FRET and calcium imaging for mGluR2 and mGluR3. * indicates statistical significance (unpaired t-test, for MNI inhibition in FRET vs. function for mGluR2, p = 0.0064; for MNI inhibition in FRET vs. function for mGluR3, p = 0.013).
(F) Representative FRET trace shows application of positive allosteric modulator LY48 at a saturating concentration induces a smaller FRET response than saturating glutamate for mGluR2. Inset, quantification of LY48 response in FRET and calcium imaging for mGluR2. * indicates statistical significance (unpaired t-test, p = 0.0033)
(G) Representative FRET trace showing glutamate titration for mGluR2-3xTM4.
(H) Glutamate FRET concentration response curves for mGluR2 and mGluR2-3xTM4 (EC_{50} = 5.39 ± 0.03). All values are normalized to saturating (1 mM) glutamate. * indicates statistical significance (two-way ANOVA, p value = 1.7E-6).

(I) Glutamate FRET concentration response curves for mGluR3 and mGluR3-3xTM4 (EC_{50} = 0.56 ± 0.10). All values are normalized to saturating (1 mM) glutamate. * indicates statistical significance (two-way ANOVA, p value = 0.0083).
(J) Representative FRET trace showing weak sensitivity to LY34 in the absence of glutamate for mGluR3-3xTM4.
(K) Summary showing decrease in basal FRET response to LY34 for mGluR3-3xTM4 compared to wild type mGluR3. * indicates statistical significance (unpaired t-test, p = 0.0048).
(L) Representative patch clamp recording showing weak sensitivity to LY34 in the absence of glutamate for mGluR3-3xTM4, indicating minimal basal receptor signaling.
(M) Summary showing decrease in basal activity as assessed by LY34 application in patch clamp recordings for mGluR3-3xTM4 compared to wild type mGluR3. * indicates statistical significance (unpaired t-test, p = 0.015). The number of cells tested are shown in parentheses. Error bars represent s.e.m.

Figure 5. Testing the role of TM6 in group II mGluR activation
(A) Left, cryo-EM structure of mGluR5 TMD dimer (PDB: 6N51) with TM4 highlighted in cyan and TM6 highlighted in pink. The side chain of I791 (I779 in mGluR2, I788 in mGluR3) is shown in green. Right, top view.
(B) Bar graph showing the percentage of spots bleaching in two steps for N-terminally SNAP-tagged constructs labeled with LD555. * indicates statistical significance (unpaired t-tests; for mGluR2-TMD vs. mGluR2-TMD-I779A, p = 0.0014; for mGluR3-TMD vs. mGluR3-TMD-I788A, p = 0.019).
(C) Calcium imaging glutamate concentration response curves for mGluR2 and mGluR2-I779A (EC_{50} = 18.66 ± 0.80). All values are normalized to saturating (1 mM) glutamate. * indicates statistical significance (two-way ANOVA, p = 1.2E-10).
(D) Glutamate calcium imaging concentration response curves for mGluR3 and mGluR3-I788A (EC_{50} = 10.43 ± 0.10). All values are normalized to saturating (1 mM) glutamate. * indicates statistical significance (two-way ANOVA, p = 8.2E-10).
(E) Summary of glutamate EC_{50} shifts relative to wild type mGluR2 or mGluR3 obtained for their respective mutants. * indicates statistical significance (two-way ANOVA; for mGluR2 vs. mGluR2-I779A, p = 1.2E-10; for mGluR2 vs. mGluR2-I779W, p = 0.0028; for mGluR2 vs. mGluR2-P778A-I779A, p = 0.0015; for mGluR3 vs. mGluR3-I788A, p = 8.2E-10). mGluR2-P778A is not significantly different from mGluR2 (two-way ANOVA, p = 0.27).
(F) LY48 calcium imaging concentration response curves for mGluR2 and mGluR2-I779A (EC_{50} = 5.46 ± 0.01). mGluR2-I779A has ~31% lower efficacy than mGluR2 at saturating LY48. All values are normalized to saturating (1 mM) glutamate. * indicates statistical significance (two-way ANOVA, p = 6.2E-9).
(G) Glutamate FRET concentration response curve for mGluR2 and mGluR2-I779A (EC_{50} = 33.63 ± 0.07). All values are normalized to saturating (1 mM) glutamate. * indicates statistical significance (two-way ANOVA, p = 0.00060).
(H) Glutamate FRET concentration response curve for mGluR3 and mGluR3-I788A (EC_{50} = 0.66 ± 0.05). All values are normalized to saturating (1 mM) glutamate. * indicates statistical significance (two-way ANOVA, p = 0.030).

Figure 6. SiMPull analysis of ligand induced inter-TMD dimer rearrangement
(A) Bar graph showing the percentage of spots bleaching in two steps for SNAP-tagged constructs labeled with LD555. * indicates statistical significance (unpaired t-test, p = 4.5E-5). Shaded bars indicate data is repeated from Figures 3C and 7B.
(B) Bar graph showing the percent change in dimerization compared to no drug conditions for SNAP-tagged constructs labeled with LD555. * indicates statistical significance (unpaired t-tests; for mGluR2-TMD-3xTM4 vs. mGluR2-TMD-3xTM4 + TASP, p = 1.4E-5; for mGluR2-TMD-I779A vs. mGluR2-TMD-I779A + MNI 137, p = 0.0016).
(C) Bar graph showing the percentage of spots bleaching in two steps for SNAP-tagged constructs labeled with LD555. * indicates statistical significance (unpaired t-tests; for mGluR2-C121A vs. mGluR2-C121A-

I779A, p = 0.00029; for mGluR2-C121A-I779A vs. mGluR2-C121A-3xTM4-I779A, p = 2.8E-6). Shaded bars indicate data is repeated from Figures 1E and 3D.
(D) Bar graph showing the percent change in dimerization compared to no drug conditions for SNAP-tagged constructs labeled with LD555. * indicates statistical significance (unpaired t-tests; for mGluR2-C121A-3xTM4 vs. mGluR2-C121A-3xTM4 + TASP, p = 0.00037; for mGluR2-C121A-3xTM4 vs. mGluR2-C121A-3xTM4 + Glu, p = 0.00095; for mGluR2-C121A-I779A vs. mGluR2-C121A-I779A + MNI 137, p = 0.00088).
(E) Bar graph showing the percentage of spots bleaching in two steps for SNAP-tagged constructs labeled with LD555. * indicates statistical significance (unpaired t-test, p = 8.1E-5). Shaded bars indicate data is repeated from Figures 1E and 3E.
(F) Bar graph showing the percent change in dimerization compared to no drug conditions for SNAP-tagged constructs labeled with LD555. * indicates statistical significance (unpaired t-tests; for mGluR3-C127A vs. mGluR3-C127A + Glu, p = 0.00060; for mGluR3-C127A-I788A vs. mGluR3-C127A-I788A + LY34, p = 0.00021). The number of movies analyzed is shown in parentheses. Error bars represent s.e.m.
(G) Schematic summarizing data indicating that TM4 mediates inactive interfaces which reorient to a TM6 interface upon activation by PAMs or agonists.

Figure 7. mGluR2/3 heterodimers show intermediate inter-TMD affinity compared to parent homodimers.
(A) Top, schematic of 2-color heterodimer SiMPull experiments where HA-SNAP-mGluR2-TMD (labeled with LD655) is able to immobilize with CLIP-mGluR3-TMD (labeled with DY-547). Bottom, representative image showing efficient pulldown in both channels, indicative of heterodimerization of mGluR2 and mGluR3 TMDs.
(B) Summary bar graph showing the efficiency of pulldown of either CLIP-mGluR2-TMD or CLIP-mGluR3-TMD by SNAP-mGluR2-TMD. *** indicates statistical significance (unpaired t-test; p=3.8E-6).
(C) Top, schematic of 2-color heterodimer SiMPull experiments where HA-SNAP-mGluR3-TMD (labeled with LD655) is able to immobilize with CLIP-mGluR2-TMD (labeled with DY-547) via an anti-HA antibody. Bottom, representative image showing efficient pulldown in both channels, indicative of heterodimerization.
(D) Summary bar graph showing the efficiency of pulldown of either CLIP-mGluR2-TMD or CLIP-mGluR3-TMD by SNAP-mGluR2-TMD. ** indicates statistical significance (unpaired t-test; p=0.0097).
(E) Representative images showing SiMPull of full-length CLIP-mGluR3 by full-length HA-SNAP-mGluR2.
(F) Summary bar graph showing efficiency of pulldown of wild type and mutant full-length CLIP-tagged mGluR2 and mGluR3 by HA-SNAP-mGluR2. *** indicates statistical significance (unpaired t-tests; for mGluR2/mGluR2 vs. mGluR2/mGluR3, p=1.6E-6; for C121A/C121A vs. C121A/C127A, p=1.9E-9; for C121A/C127A vs. C121A/C127A-3xTM4, p=1.2E-5).
(G) Summary bar graph showing efficiency of pulldown of wild type and mutant full-length CLIP-tagged mGluR2 and mGluR3 by HA-SNAP-mGluR3. *** indicates statistical significance (unpaired t-tests; for C127A/C127A vs. C127A/C121A, p=1.3E-5; for C127A/C121A vs. C127A/C121A-3xTM4, p=0.00081).
(H) Summary schematic showing relative dimerization propensities of mGluR2, mGluR2/3 and mGluR3 TMD.

Figure 8. A working model of inter-TMD rearrangement and mGluR activation.
(A) Four-state working model of inter-TMD rearrangement during mGluR activation. LBD-driven TMD dimer formation occurs first, followed by dimer reorientation from TM4-containing to TM6-containing interfaces, and intra-subunit conformational changes. Transitions between steps can be differentially modulated by orthosteric and allosteric drugs.
(B) Proposed relative free energy plots along the activation pathway for mGluR2. Inset, TM4 dimer interface intermediates likely show differential stabilities across subtypes which tunes the efficiency of

activation and the relative basal activity. Multiple local energy minima likely exist within state 2 due to distinct inter-TMD dimer interfaces that involve TM4.
(C) Proposed relative free energy plots for mGluR2 in the absence and presence of agonist and G protein showing possible relative stabilizations of states and alterations of energy barriers. Generally, agonist-binding lowers the barrier between states 1 and 2 and stabilizes TM6 interfaces (states 3 and 4) while G protein further stabilizes state 4. It's important to note that there are likely many microstates and alternative activation trajectories that are not captured in this simplified model.

References:

BAYBURT, T., LEITZ, A., XIE, G., OPRIAN, D. & SLIGAR, S. 2007. Transducin activation by nanoscale lipid bilayers containing one and two rhodopsins. *The Journal of biological chemistry,* 282.

BUSSI, G., D, D. & M, P. 2007. Canonical sampling through velocity rescaling. *The Journal of chemical physics,* 126.

CHANGEUX, J.-P. & CHRISTOPOULOS, A. 2016. Allosteric Modulation as a Unifying Mechanism for Receptor Function and Regulation. *Cell,* 166.

CHRISTOPHER, J., Z, O., M, C., AS, D., JC, E., FH, M., JS, M., K, O., P, R., MJ, S.-V., GG, F. & GM, K. 2019. Structure-Based Optimization Strategies for G Protein-Coupled Receptor (GPCR) Allosteric Modulators: A Case Study from Analyses of New Metabotropic Glutamate Receptor 5 (mGlu 5) X-ray Structures. *Journal of medicinal chemistry,* 62.

CONKLIN, B. R., FARFEL, Z., LUSTIG, K. D., JULIUS, D. & BOURNE, H. R. 1993. Substitution of three amino acids switches receptor specificity of G q α to that of G i α. *Nature,* 363**,** 274-276.

DE JONG, D., G, S., WF, B., C, A., TA, W., LV, S., X, P., DP, T. & SJ, M. 2013. Improved Parameters for the Martini Coarse-Grained Protein Force Field. *Journal of chemical theory and computation,* 9.

DELGADO, D. M., MØLLER, T. C., STER, J., GIRALDO, J., MAUREL, D., ROVIRA, X., SCHOLLER, P., ZWIER, J. M., PERROY, J., DURROUX, T., TRINQUET, E., PREZEAU, L., RONDARD, P. & PIN, J.-P. 2017. Pharmacological evidence for a metabotropic glutamate receptor heterodimer in neuronal cells.

DELILLE, H. K., BECKER, J. M., BURKHARDT, S., BLEHER, B., TERSTAPPEN, G. C., SCHMIDT, M., MEYER, A. H., UNGER, L., MAREK, G. J. & MEZLER, M. 2012. Heterocomplex formation of 5-HT2A-mGlu2 and its relevance for cellular signaling cascades. *Neuropharmacology,* 62**,** 2184-91.

DIJKMAN, P., OK, C., AD, G., JC, M.-G., C, D. G., MI, W. & A, W. 2018. Dynamic tuneable G protein-coupled receptor monomer-dimer populations. *Nature communications,* 9.

DONG, H., M, S., HX, Z. & TA, C. 2012. Glycines: role in α-helical membrane protein structures and a potential indicator of native conformation. *Biochemistry,* 51.

DORE, A. S., OKRASA, K., PATEL, J. C., SERRANO-VEGA, M., BENNETT, K., COOKE, R. M., ERREY, J. C., JAZAYERI, A., KHAN, S., TEHAN, B., WEIR, M., WIGGIN, G. R. & MARSHALL, F. H. 2014. Structure of class C GPCR metabotropic glutamate receptor 5 transmembrane domain. *Nature,* 511**,** 557-62.

DOUMAZANE, E., SCHOLLER, P., FABRE, L., ZWIER, J. M., TRINQUET, E., PIN, J. P. & RONDARD, P. 2013. Illuminating the activation mechanisms and allosteric properties of metabotropic glutamate receptors. *Proc Natl Acad Sci U S A,* 110**,** E1416-25.

DOUMAZANE, E., SCHOLLER, P., ZWIER, J. M., TRINQUET, E., RONDARD, P. & PIN, J. P. 2011. A new approach to analyze cell surface protein complexes reveals specific heterodimeric metabotropic glutamate receptors. *Faseb j,* 25**,** 66-77.

EILERS, M., SHEKAR, S., SHEKAR C., SHIEH, T., SMITH, S. O. & FLEMING, P. J. 2000. Internal packing of helical membrane proteins.

EL MOUSTAINE, D., GRANIER, S., DOUMAZANE, E., SCHOLLER, P., RAHMEH, R., BRON, P., MOUILLAC, B., BANERES, J. L., RONDARD, P. & PIN, J. P. 2012. Distinct roles of metabotropic glutamate receptor dimerization in agonist activation and G-protein coupling. *Proc Natl Acad Sci U S A,* 109**,** 16342-7.

ELLAITHY, A., GONZALEZ-MAESO, J., LOGOTHETIS, D. A. & LEVITZ, J. 2020. Structural and Biophysical Mechanisms of Class C G Protein-Coupled Receptor Function: Trends in Biochemical Sciences.

ESLAMI, H., F, M., J, M. & F, M.-P. 2008. Molecular dynamics simulation of confined fluids in isosurface-isothermal-isobaric ensemble. *The Journal of chemical physics,* 129.

FELCE, J., SL, L., RG, K., SR, M., Y, L., SF, L., D, K. & SJ, D. 2017. Receptor Quaternary Organization Explains G Protein-Coupled Receptor Family Structure. *Cell reports,* 20.

FERRÉ, S., CASADÓ, V., DEVI, L. A., FILIZOLA, M., JOCKERS, R., LOHSE, M. J., MILLIGAN, G., PIN, J.-P. & GUITART, X. 2014. G protein-coupled receptor oligomerization revisited: functional and pharmacological perspectives. *Pharmacological reviews,* 66.

FRIBOURG, M., MORENO, J. L., HOLLOWAY, T., PROVASI, D., BAKI, L., MAHAJAN, R., PARK, G., ADNEY, S. K., HATCHER, C., ELTIT, J. M., RUTA, J. D., ALBIZU, L., LI, Z., UMALI, A., SHIM, J., FABIATO, A., MACKERELL, A. D., BREZINA, V., SEALFON, S. C., FILIZOLA, M., GONZÁLEZ-MAESO, J. & LOGOTHETIS, D. E. 2011. Decoding the Signaling of a GPCR Heteromeric Complex Reveals a Unifying Mechanism of Action of Antipsychotic Drugs. *Cell,* 147**,** 1011-23.

GIBSON, D., L, Y., RY, C., JC, V., CA, H. & HO, S. 2009. Enzymatic assembly of DNA molecules up to several hundred kilobases. *Nature methods,* 6.

GONZALEZ-MAESO, J., ANG, R. L., YUEN, T., CHAN, P., WEISSTAUB, N. V., LOPEZ-GIMENEZ, J. F., ZHOU, M., OKAWA, Y., CALLADO, L. F., MILLIGAN, G., GINGRICH, J. A., FILIZOLA, M., MEANA, J. J. & SEALFON, S. C. 2008. Identification of a serotonin/glutamate receptor complex implicated in psychosis. *Nature,* 452**,** 93-7.

GOUDET, C., GAVEN, F., KNIAZEFF, J., VOL, C., LIU, J., COHEN-GONSAUD, M., ACHER, F., PREZEAU, L. & PIN, J. P. 2004. Heptahelical domain of metabotropic glutamate receptor 5 behaves like rhodopsin-like receptors. *Proc Natl Acad Sci U S A,* 101**,** 378-83.

GRIMM, J. B., ENGLISH, B. P., CHOI, H., MUTHUSAMY, A. K., MEHL, B. P., DONG, P., BROWN, T. A., LIPPINCOTT-SCHWARTZ, J., LIU, Z., LIONNET, T. & LAVIS, L. D. 2016. Bright photoactivatable fluorophores for single-molecule imaging. *Nature Methods,* 13**,** 985-988.

GRIMM, J. B., TKACHUK, A. N., XIE, L., CHOI, H., MOHAR, B., FALCO, N., SCHAEFER, K., PATEL, R., ZHENG, Q., LIU, Z., LIPPINCOTT-SCHWARTZ, J., BROWN, T. A. & LAVIS, L. D. 2020. A general method to optimize and functionalize red-shifted rhodamine dyes. *Nature Methods,* 17**,** 815-821.

GRUSHEVSKYI, E. O., KUKAJ, T., SCHMAUDER, R., BOCK, A., ZABEL, U., SCHWABE, T., BENNDORF, K. & LOHSE, M. J. 2019. Stepwise activation of a class C GPCR begins with millisecond dimer rearrangement.

GUREVICH, V. & GUREVICH, E. 2008. How and why do GPCRs dimerize? *Trends in pharmacological sciences,* 29.

GUTZEIT, V. A., THIBADO, J., STOR, D. S., ZHOU, Z., BLANCHARD, S. C., ANDERSEN, O. S. & LEVITZ, J. 2019. Conformational dynamics between transmembrane domains and allosteric modulation of a metabotropic glutamate receptor.

HABRIAN, C., LEVITZ, J., VYKLICKY, V., FU, Z., HOAGLAND, A., MCCORT-TRANCHEPAIN, I., ACHER, F. & ISACOFF, E. Y. 2019. Conformational pathway provides unique sensitivity to a synaptic mGluR. *Nature Communications,* 10**,** 1-13.

HEMSTAPAT, K., H, D. C., Y, N., AE, B., Q, L., CM, N., GD, T. & PJ, C. 2007. A novel family of potent negative allosteric modulators of group II metabotropic glutamate receptors. *The Journal of pharmacology and experimental therapeutics,* 322.

HERN, J. A., BAIG, A. H., MASHANOV, G. I., BIRDSALL, B., T, C. J. E., LAZARENO, S., MOLLOY, J. E. & M, B. N. J. 2010. Formation and dissociation of M1 muscarinic receptor dimers seen by total internal reflection fluorescence imaging of single molecules.

HLAVACKOVA, V., ZABEL, U., FRANKOVA, D., BATZ, J., HOFFMANN, C., PREZEAU, L., PIN, J. P., BLAHOS, J. & LOHSE, M. J. 2012. Sequential inter- and intrasubunit rearrangements during activation of dimeric metabotropic glutamate receptor 1. *Sci Signal,* 5**,** ra59.

HUANG, S., J, C., M, J., G, L., J, L., JP, P. & P, R. 2011. Interdomain movements in metabotropic glutamate receptor activation. *Proceedings of the National Academy of Sciences of the United States of America,* 108.

HÖGEL, P., GÖTZ, A., KUHNE, F., EBERT, M., STELZER, W., RAND, K. D., SCHARNAGL, C. & LANGOSCH, D. 2018. Glycine Perturbs Local and Global Conformational Flexibility of a Transmembrane Helix. *Biochemistry,* 57.

IŞBILIR, A., J, M., M, A., V, B., C, P.-V., C, H., A, I., R, H., C, D. G., MJ, S., P, A. & MJ, L. 2020. Advanced fluorescence microscopy reveals disruption of dynamic CXCR4 dimerization by subpocket-specific inverse agonists. *Proceedings of the National Academy of Sciences of the United States of America,* 117.

JACOBSON, M., RA, F., Z, X. & B, H. 2002. On the role of the crystal environment in determining protein side-chain conformations. *Journal of molecular biology,* 320.

JAIN, A., LIU, R., RAMANI, B., ARAUZ, E., ISHITSUKA, Y., RAGUNATHAN, K., PARK, J., CHEN, J., XIANG, Y. K. & HA, T. 2011. Probing cellular protein complexes using single-molecule pull-down. *Nature,* 473**,** 484.

JARZYNSKI, C. 1997. Nonequilibrium Equality for Free Energy Differences. *Physical Review Letters,* 78**,** 2690.

JAVADPOUR, M. M., EILERS, M., GROESBEEK, M. & SMITH, S. O. 1999. Helix packing in polytopic membrane proteins: role of glycine in transmembrane helix association. *Biophys J,* 77**,** 1609-18.

JIN, J., F, M., G, B., F, K., Z, Z., N, C., F, A.-S., F, P., B, L., E, K. & A, B. 2018. CCR5 adopts three homodimeric conformations that control cell surface delivery. *Science signaling,* 11.

JOHNSON, M. P., BAEZ, M., JAGDMANN, G. E., JR., BRITTON, T. C., LARGE, T. H., CALLAGARO, D. O., TIZZANO, J. P., MONN, J. A. & SCHOEPP, D. D. 2003. Discovery of allosteric potentiators for the metabotropic glutamate 2 receptor: synthesis and subtype selectivity of N-(4-(2-methoxyphenoxy)phenyl)-N-(2,2,2- trifluoroethylsulfonyl)pyrid-3-ylmethylamine. *J Med Chem,* 46**,** 3189-92.

KASAI, R., SUZUKI, K., PROSSNITZ, E., KOYAMA-HONDA, I., NAKADA, C., FUJIWARA, T. & KUSUMI, A. 2011. Full characterization of GPCR monomer-dimer dynamic equilibrium by single molecule imaging. *The Journal of cell biology,* 192.

KATZUNG, B. G. 2004. *Basic & clinical pharmacology,* New York, McGraw Hill.

KOEHL, A., HU, H., FENG, D., SUN, B., ZHANG, Y., ROBERTSON, M. J., CHU, M., KOBILKA, T. S., LAEREMANS, T., STEYAERT, J., TARRASCH, J., DUTTA, S., FONSECA, R., WEIS, W. I., MATHIESEN, J. M., SKINIOTIS, G. & KOBILKA, B. K. 2019. Structural insights into the activation of metabotropic glutamate receptors. *Nature,* 566**,** 79-84.

KONERMANN, L., H, M., RG, M. & V, P. 2018. How to run molecular dynamics simulations on electrospray droplets and gas phase proteins: Basic guidelines and selected applications. *Methods (San Diego, Calif.),* 144.

KUNISHIMA, N., SHIMADA, Y., TSUJI, Y., SATO, T., YAMAMOTO, M., KUMASAKA, T., NAKANISHI, S., JINGAMI, H. & MORIKAWA, K. 2000. Structural basis of glutamate recognition by a dimeric metabotropic glutamate receptor. *Nature,* 407**,** 971-7.

KUSZAK, A., S, P., JP, A., HI, M., NG, W. & RK, S. 2009. Purification and functional reconstitution of monomeric mu-opioid receptors: allosteric modulation of agonist binding by Gi2. *The Journal of biological chemistry,* 284.

LEE, J., MUNGUBA, H., GUTZEIT, V. A., SINGH, DEO R, K., MELANIE, DITTMAN, J. S. & LEVITZ, J. 2020. Defining the Homo- and Heterodimerization Propensities of Metabotropic Glutamate Receptors. *Cell reports,* 31.

LEVITZ, J., HABRIAN, C., BHARILL, S., FU, Z., VAFABAKHSH, R. & ISACOFF, E. Y. 2016. Mechanism of Assembly and Cooperativity of Homomeric and Heteromeric Metabotropic Glutamate Receptors. *Neuron,* 92**,** 143-159.

LIAUW, B., HS, A. & R, V. 2021. Conformational rearrangement during activation of a metabotropic glutamate receptor. *Nature chemical biology*.

LIU, J., ZHANG, Z., MORENO-DELGADO, D., DALTON, J. A., ROVIRA, X., TRAPERO, A., GOUDET, C., LLEBARIA, A., GIRALDO, J., YUAN, Q., RONDARD, P., HUANG, S., LIU, J. & PIN, J.-P. P. 2017. Allosteric control of an asymmetric transduction in a G protein-coupled receptor heterodimer.

LOS, G. V., ENCELL, L. P., MCDOUGALL, M. G., HARTZELL, D. D., KARASSINA, N., ZIMPRICH, C., WOOD, M. G., LEARISH, R., OHANA, R. F., URH, M., SIMPSON, D., MENDEZ, J., ZIMMERMAN, K., OTTO, P., VIDUGIRIS, G., ZHU, J., DARZINS, A., KLAUBERT, D. H., BULLEIT, R. F. & WOOD, K. V. 2008. HaloTag: A Novel Protein Labeling Technology for Cell Imaging and Protein Analysis.

MANGLIK, A., TH, K., M, M., C, A., Z, Y., D, H., MT, L., TS, K., FS, T., WL, H., RS, P. & BK, K. 2015. Structural Insights into the Dynamic Process of β2-Adrenergic Receptor Signaling. *Cell,* 161.

MAO, C., SHEN, C., LI, C., SHEN, D.-D., XU, C., ZHANG, S., ZHOU, R., SHEN, Q., CHEN, L.-N., JIANG, Z., LIU, J. & ZHANG, Y. 2020. Cryo-EM structures of inactive and Gi-coupled GABAB heterodimer.

MARCAGGI, P., MUTOH, H., DIMITROV, D., BEATO, M. & KNÖPFEL, T. 2009. Optical measurement of mGluR1 conformational changes reveals fast activation, slow deactivation, and sensitization. *Proc Natl Acad Sci U S A.*

MERAL, D., PROVASI, D., PRADA-GRACIA, D., MÖLLER, J., MARINO, K., LOHSE, M. J. & FILIZOLA, M. 2018. Molecular details of dimerization kinetics reveal negligible populations of transient μ-opioid receptor homodimers at physiological concentrations. *Scientific Reports,* 8**,** 1-13.

MILLIGAN, G., WARD, R. & MARSANGO, S. 2019. GPCR homo-oligomerization. *Current opinion in cell biology,* 57.

MORENO, J. L., MIRANDA-AZPIAZU, P., GARCIA-BEA, A., YOUNKIN, J., CUI, M., KOZLENKOV, A., BEN-EZRA, A., VOLOUDAKIS, G., FAKIRA, A. K., BAKI, L., GE, Y., GEORGAKOPOULOS, A., MORON, J. A., MILLIGAN, G., LOPEZ-GIMENEZ, J. F., ROBAKIS, N. K., LOGOTHETIS, D. E., MEANA, J. J. & GONZALEZ-MAESO, J. 2016. Allosteric signaling through an mGlu2 and 5-HT2A heteromeric receptor complex and its potential contribution to schizophrenia. *Sci Signal,* 9**,** ra5.

MORENO, J. L., MUGURUZA, C., UMALI, A., MORTILLO, S., HOLLOWAY, T., PILAR-CUELLAR, F., MOCCI, G., SETO, J., CALLADO, L. F., NEVE, R. L., MILLIGAN, G., SEALFON, S. C., LOPEZ-GIMENEZ, J. F., MEANA, J. J., BENSON, D. L. & GONZALEZ-MAESO, J. 2012. Identification of three residues essential for 5-hydroxytryptamine 2A-

metabotropic glutamate 2 (5-HT2A.mGlu2) receptor heteromerization and its psychoactive behavioral function. *J Biol Chem,* 287**,** 44301-19.

MP, J., DL, P., CS, R., TJ, D., B, H., DE, S. & RA, F. 2004. A hierarchical approach to all-atom protein loop prediction. *Proteins,* 55.

MUTO, T., TSUCHIYA, D., MORIKAWA, K. & JINGAMI, H. 2007. Structures of the extracellular regions of the group II/III metabotropic glutamate receptors. *Proc Natl Acad Sci U S A,* 104**,** 3759-64.

MÖLLER, J., A, I., T, S., B, O., C, K., V, S., EO, G., A, B., P, A., M, H., C, S. & MJ, L. 2020. Single-molecule analysis reveals agonist-specific dimer formation of μ-opioid receptors. *Nature chemical biology,* 16.

MØLLER, T., J, H., C, C., JM, Z., T, D., P, R., L, P., CA, R., JP, P., E, M. & J, K. 2018. Oligomerization of a G protein-coupled receptor in neurons controlled by its structural dynamics. *Scientific reports,* 8.

NYGAARD, R., Y, Z., RO, D., TJ, M., DH, A., A, M., AC, P., CW, L., JJ, F., MP, B., FS, T., TS, K., DE, S., L, M., RS, P. & BK, K. 2013. The dynamic process of β(2)-adrenergic receptor activation. *Cell,* 152.

O'BRIEN, D., DM, S., HP, C., AJ, C., SS, W., AS, F., J, B., CS, E., CW, L., CM, N. & PJ, C. 2018. Differential Pharmacology and Binding of mGlu 2 Receptor Allosteric Modulators. *Molecular pharmacology,* 93.

OLOFSSON, L., FELEKYAN, S., DOUMAZANE, E., SCHOLLER, P., FABRE, L., ZWIER, J. M., RONDARD, P., SEIDEL, C. A., PIN, J. P. & MARGEAT, E. 2014. Fine tuning of sub-millisecond conformational dynamics controls metabotropic glutamate receptors agonist efficacy. *Nat Commun,* 5**,** 5206.

PAPASERGI-SCOTT, M. M., ROBERTSON, M. J., SEVEN, A. B., PANOVA, O., MATHIESEN, J. M. & SKINIOTIS, G. 2020. Structures of metabotropic GABA B receptor. *Nature,* 584**,** 310-314.

PARK, J., FU, Z., FRANGAJ, A., LIU, J., MOSYAK, L., SHEN, T., SLAVKOVICH, V. N., RAY, K. M., TAURA, J., CAO, B., GENG, Y., ZUO, H., KOU, Y., GRASSUCCI, R., CHEN, S., LIU, Z., LIN, X., WILLIAMS, J. P., RICE, W. J., ENG, E. T., HUANG, R. K., SONI, R. K., KLOSS, B., YU, Z., JAVITCH, J. A., HENDRICKSON, W. A., SLESINGER, P. A., QUICK, M., GRAZIANO, J., YU, H., FIEHN, O., CLARKE, O. B., FRANK, J. & FAN, Q. R. 2020. Structure of human GABA B receptor in an inactive state. *Nature,* 584**,** 304-309.

PARRINELLO, M. & RAHMAN, A. 1998. Polymorphic transitions in single crystals: A new molecular dynamics method.

QINSI, Z., JOCKUSCH, S., ZHOU, Z., ALTMAN, R. B., ZHAO, H., ASHER, W., HOLSEY, M., MATHIASEN, S., GEGGIER, P., JAVITCH, J. A. & BLANCHARD, S. C. 2017. Electronic tuning of self-healing fluorophores for live-cell and single-molecule imaging.

RASMUSSEN, S., HJ, C., JJ, F., E, P., P, C., PS, C., BT, D., DM, R., FS, T., TS, K., A, S., I, K., RK, S., SH, G., A, P., J, S., WI, W. & BK, K. 2011. Structure of a nanobody-stabilized active state of the β(2) adrenoceptor. *Nature,* 469.

REINER, A. & LEVITZ, J. 2018. Glutamatergic Signaling in the Central Nervous System: Ionotropic and Metabotropic Receptors in Concert. *Neuron,* 98.

ROMANO, C., YANG, W. L. & O'MALLEY, K. L. 1996. Metabotropic glutamate receptor 5 is a disulfide-linked dimer. *J Biol Chem,* 271**,** 28612-6.

ROVIRA, X., MALHAIRE, F., SCHOLLER, P., RODRIGO, J., GONZALEZ-BULNES, P., LLEBARIA, A., PIN, J.-P., GIRALDO, J. & GOUDET, C. 2015. Overlapping binding sites drive allosteric agonism and positive cooperativity in type 4 metabotropic glutamate receptors. *FASEB journal : official publication of the Federation of American Societies for Experimental Biology,* 29.

RÖBLITZ, S. & WEBER, M. 2013. Fuzzy spectral clustering by PCCA+: application to Markov state models and data classification. *Advances in Data Analysis and Classification,* 7**,** 147-179.

SALI, A. & TL, B. 1993. Comparative protein modelling by satisfaction of spatial restraints. *Journal of molecular biology,* 234.

SCHERER, M., B, T.-S., F, P., G, P.-H., M, H., N, P., C, W., JH, P. & F, N. 2015. PyEMMA 2: A Software Package for Estimation, Validation, and Analysis of Markov Models. *Journal of chemical theory and computation,* 11.

SENES, A., GERSTEIN, M. & ENGELMAN, D. M. 2000. Statistical Analysis of Amino Acid Patterns in Transmembrane Helices: The GxxxG Motif Occurs Frequently and in Association With Beta-Branched Residues at Neighboring Positions. *Journal of molecular biology,* 296.

SEVASTYANOVA, T. & KAMMERMEIER, P. 2014. Cooperative signaling between homodimers of metabotropic glutamate receptors 1 and 5. *Molecular pharmacology,* 86.

SHAYE, H., ISHCHENKO, A., LAM, J. H., HAN, G. W., XUE, L., RONDARD, P., PIN, J.-P., KATRITCH, V., GATI, C. & CHEREZOV, V. 2020. Structural basis of the activation of a metabotropic GABA receptor. *Nature,* 584**,** 298-303.

SHEN, M. & SALI, A. 2006. Statistical potential for assessment and prediction of protein structures. *Protein science : a publication of the Protein Society,* 15.

SLENO, R. & HÉBERT, T. E. 2019. Shaky ground - The nature of metastable GPCR signalling complexes. *Neuropharmacology,* 152.

TATEYAMA, M., HIDEKI, A., NAKATA, H., SAITO, O. & KUBO, Y. 2004. Ligand-induced rearrangement of the dimeric metabotropic glutamate receptor 1α. *Nature Structural & Molecular Biology,* 11**,** 637-642.

TATEYAMA, M. & KUBO, Y. 2006. Dual signaling is differentially activated by different active states of the metabotropic glutamate receptor 1α.

TORA, A. S., ROVIRA, X., CAO, A.-M., CABAYE, A., OLOFSSON, L., MALHAIRE, F., SCHOLLER, P., BAIK, H., EECKHAUT, A. V., SMOLDERS, I., RONARD, P., MARGEAT, E., ACHER, F., PIN, J.-P. & GOUDET, C. 2018. Chloride ions stabilize the glutamate-induced active state of the metabotropic glutamate receptor 3. *Neuropharmacology,* 140.

TRIBELLO, G. A., BONOMI, M., BRANDUARDI, D., CAMILLONI, C. & BUSSI, G. 2014. PLUMED 2: New feathers for an old bird. *Computer Physics Communications,* 185**,** 604-613.

TSUCHIYA, D., KUNISHIMA, N., KAMIYA, N., JINGAMI, H. & MORIKAWA, K. 2002. Structural views of the ligand-binding cores of a metabotropic glutamate receptor complexed with an antagonist and both glutamate and Gd3+. *Proc Natl Acad Sci U S A,* 99**,** 2660-5.

ULBRICH, M. H. & ISACOFF, E. Y. 2007. Subunit counting in membrane-bound proteins. *Nature Methods,* 4**,** 319.

ULMSCHNEIDER, M. B. & SANSOM, M. S. 2001. Amino Acid Distributions in Integral Membrane Protein Structures. *Biochimica et biophysica acta,* 1512.

VAFABAKHSH, R., LEVITZ, J. & ISACOFF, E. Y. 2015. Conformational dynamics of a class C G-protein-coupled receptor. *Nature,* 524**,** 497-501.

WASSENAAR, T., HI, I., RA, B., DP, T. & SJ, M. 2015. Computational Lipidomics with insane: A Versatile Tool for Generating Custom Membranes for Molecular Simulations. *Journal of chemical theory and computation,* 11.

WASSENAAR, T., K, P., RA, B., SJ, M. & DP, T. 2014. Going Backward: A Flexible Geometric Approach to Reverse Transformation from Coarse Grained to Atomistic Models. *Journal of chemical theory and computation,* 10.

WEIS, W. & KOBILKA, B. 2018. The Molecular Basis of G Protein-Coupled Receptor Activation. *Annual review of biochemistry,* 87.

WERTHMANN, R., M, T., J, L., A, A., T, F., L, T., M, S., A, R., C, D., C, F., M, G., L, L. & B, B. 2020. Symmetric signal transduction and negative allosteric modulation of heterodimeric mGlu1/5 receptors. *Neuropharmacology*.

WHORTON, M., JASTRZEBSKA, B., PARK, P., FOTIADIS, D., ENGEL, A., PALCZEWSKI, K. & SUNAHARA, R. 2008. Efficient coupling of transducin to monomeric rhodopsin in a phospholipid bilayer. *The Journal of biological chemistry,* 283.

WHORTON, M., MP, B., SG, R., B, H., RN, Z., B, K. & RK, S. 2007. A monomeric G protein-coupled receptor isolated in a high-density lipoprotein particle efficiently activates its G protein. *Proceedings of the National Academy of Sciences of the United States of America,* 104.

WU, H., WANG, C., GREGORY, K. J., HAN, G. W., CHO, H. P., XIA, Y., NISWENDER, C. M., KATRITCH, V., MEILER, J., CHEREZOV, V., CONN, P. J. & STEVENS, R. C. 2014. Structure of a class C GPCR metabotropic glutamate receptor 1 bound to an allosteric modulator#. *Science,* 344**,** 58-64.

XUE, L., ROVIRA, X., SCHOLLER, P., ZHAO, H., LIU, J., PIN, J.-P. & RONDARD, P. 2014. Major ligand-induced rearrangement of the heptahelical domain interface in a GPCR dimer. *Nature Chemical Biology,* 11**,** 134.

YIN, S., NOETZEL, M. J., JOHNSON, K. A., ZAMORANO, R., JALAN-SAKRIKAR, N., GREGORY, K. J., CONN, P. J. & NISWENDER, C. M. 2014. Selective Actions of Novel Allosteric Modulators Reveal Functional Heteromers of Metabotropic Glutamate Receptors in the CNS.

Figure 1

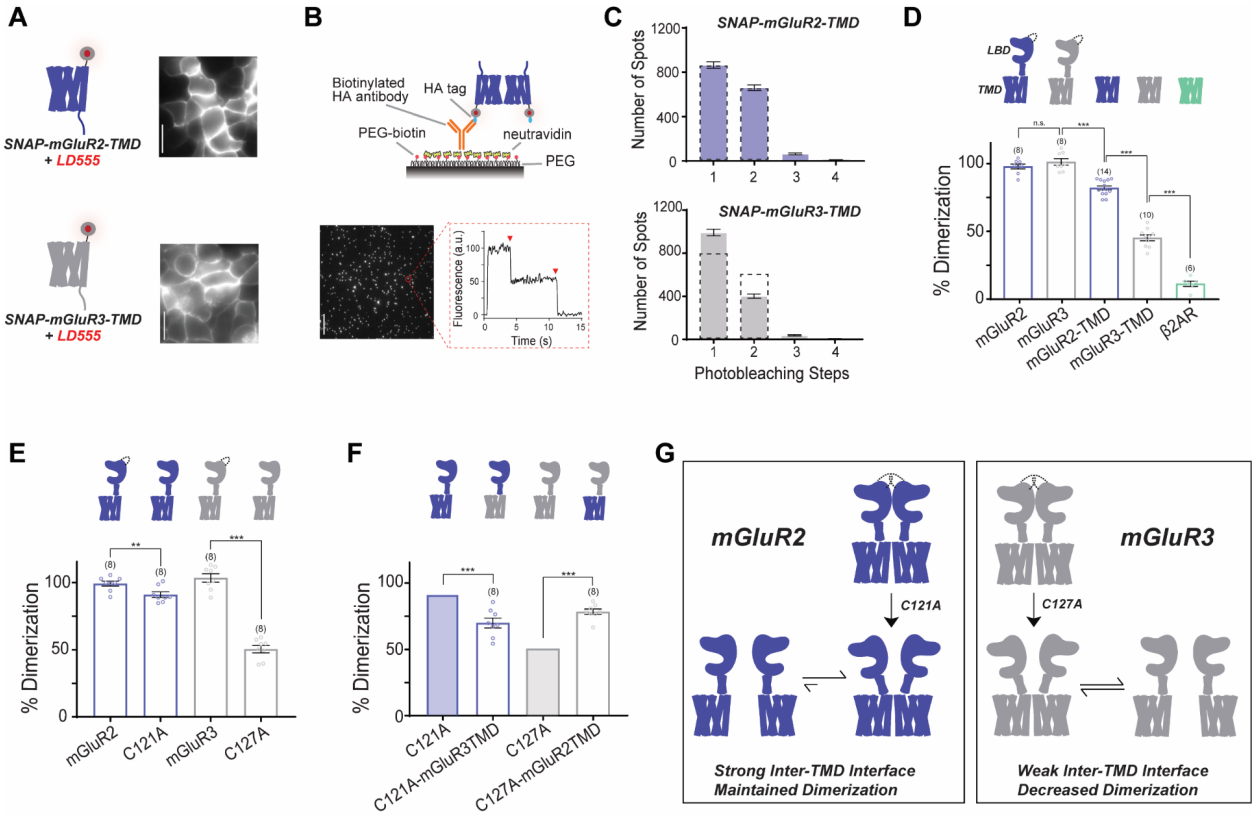

Figure 2

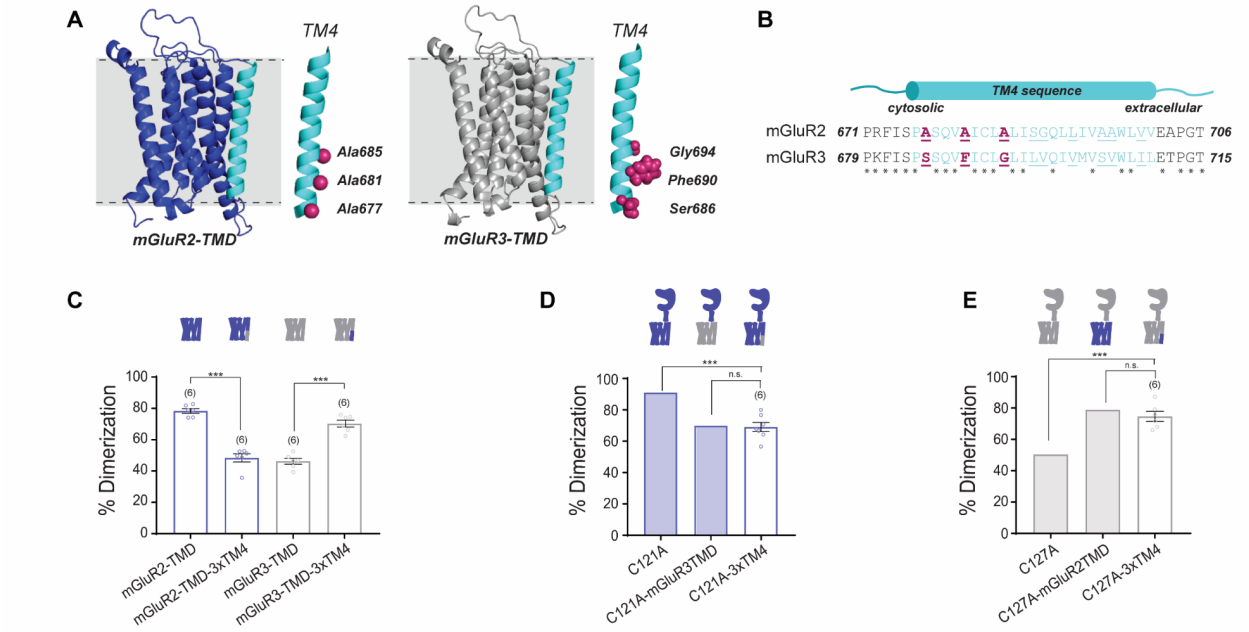

Figure 3

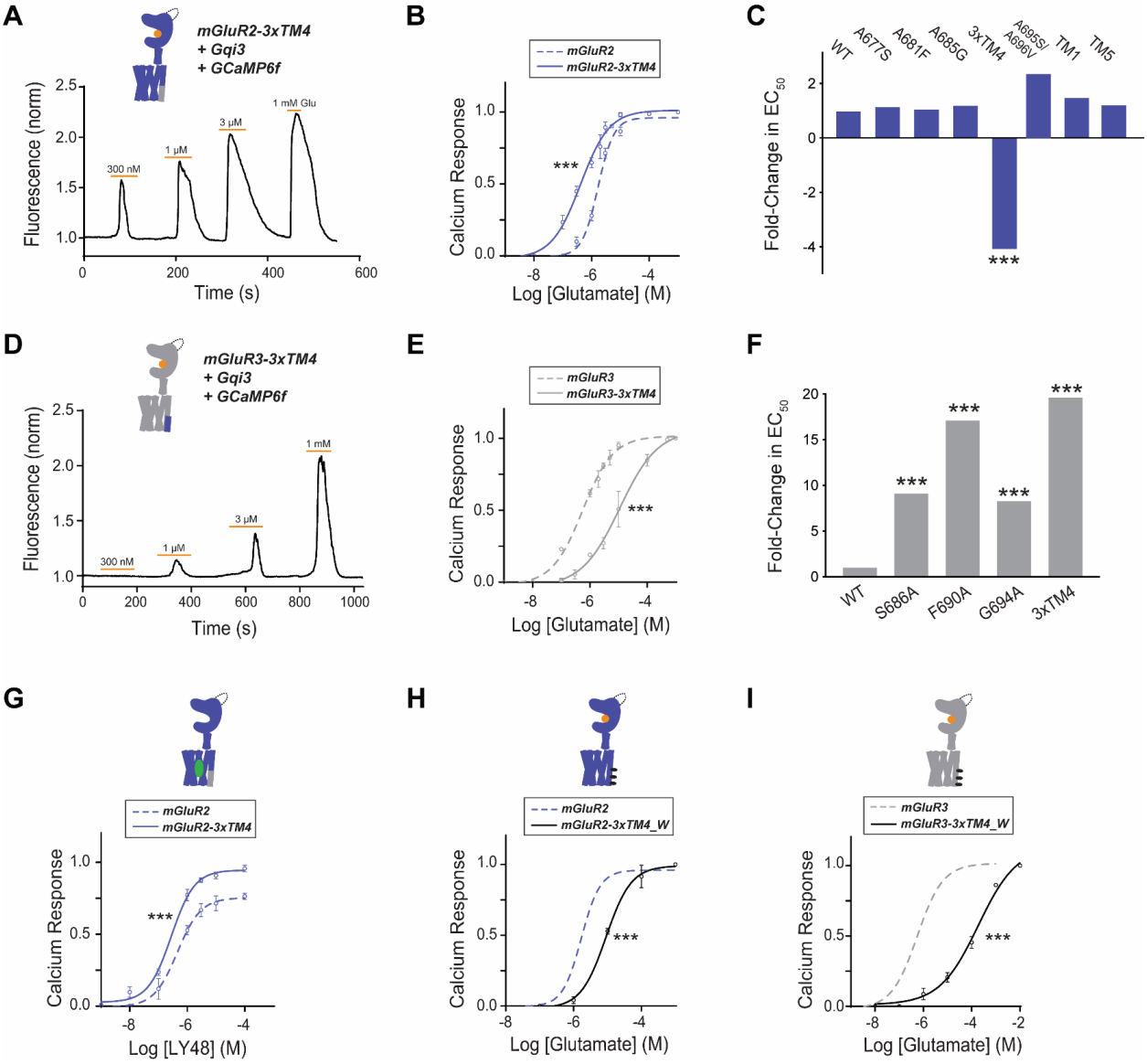

Figure 4

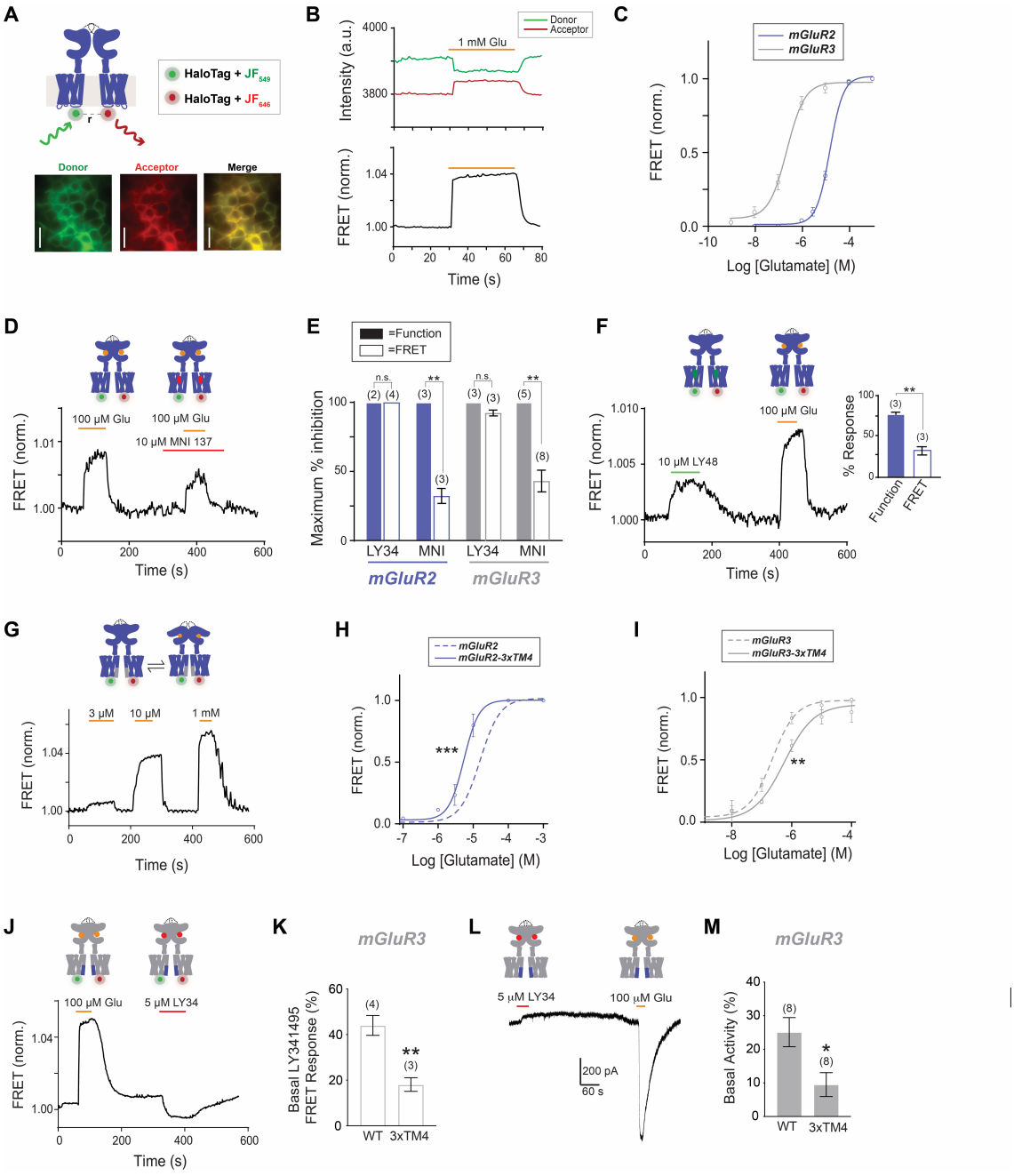

Figure 5

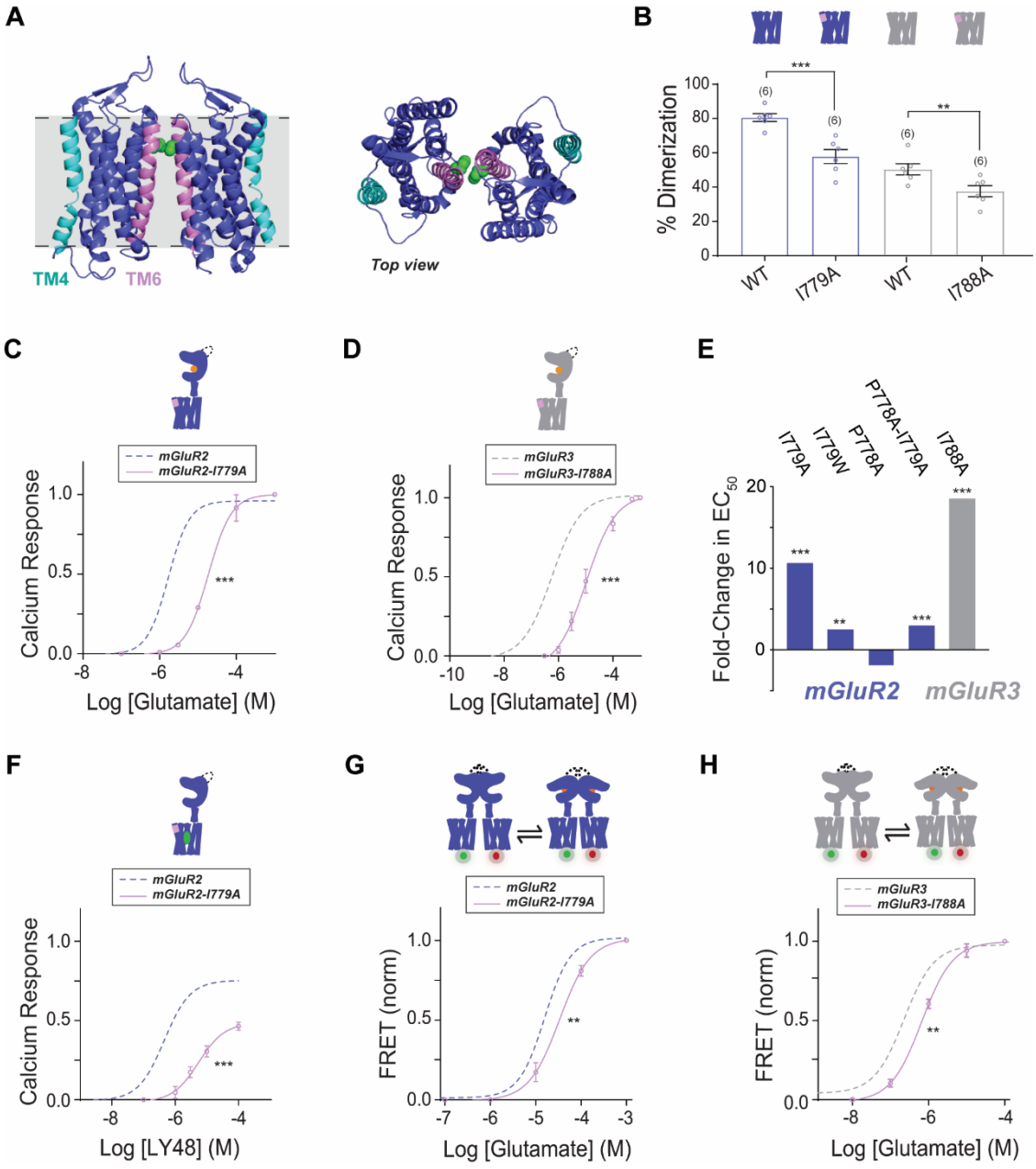

Figure 6

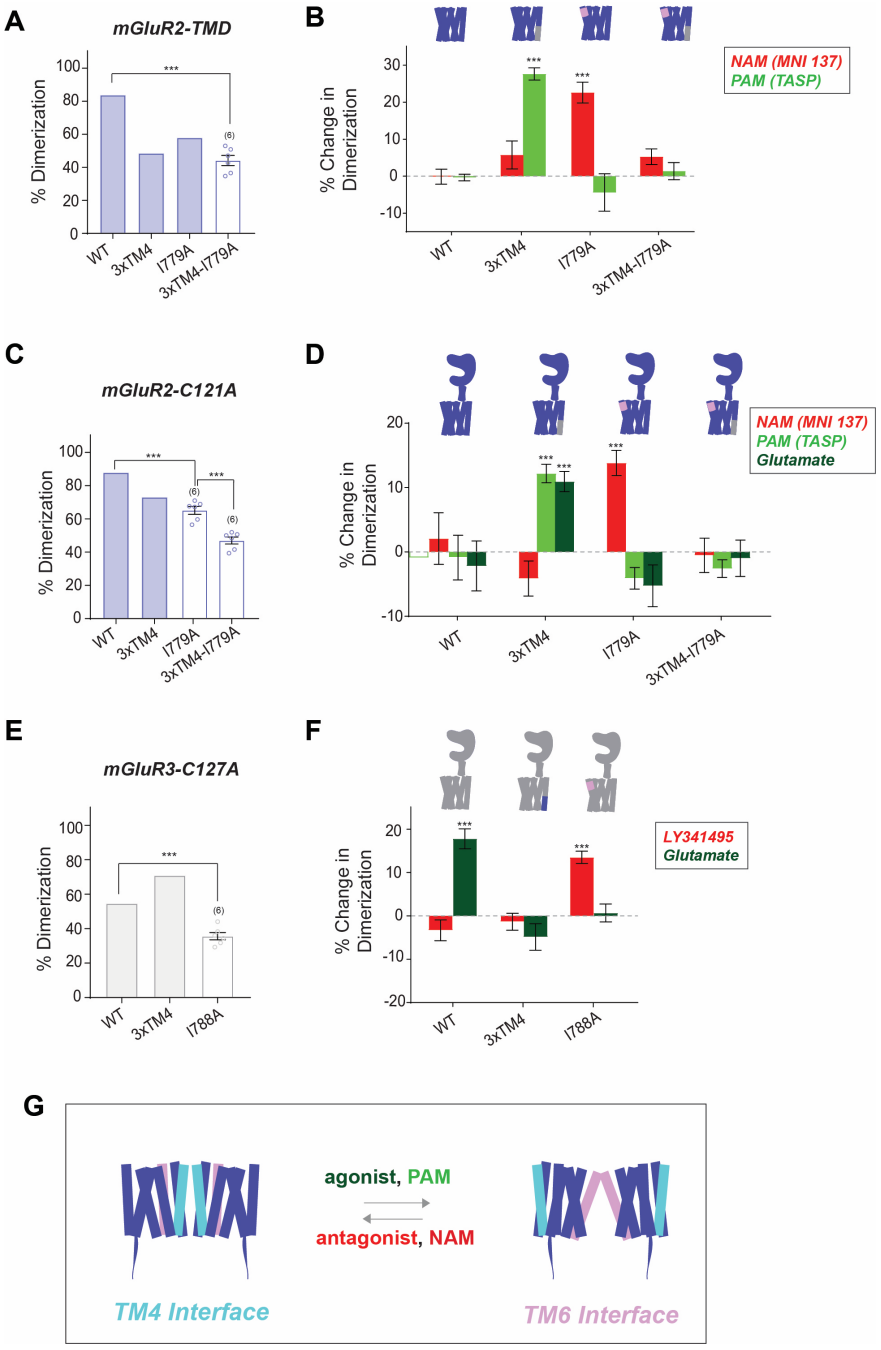

Figure 7

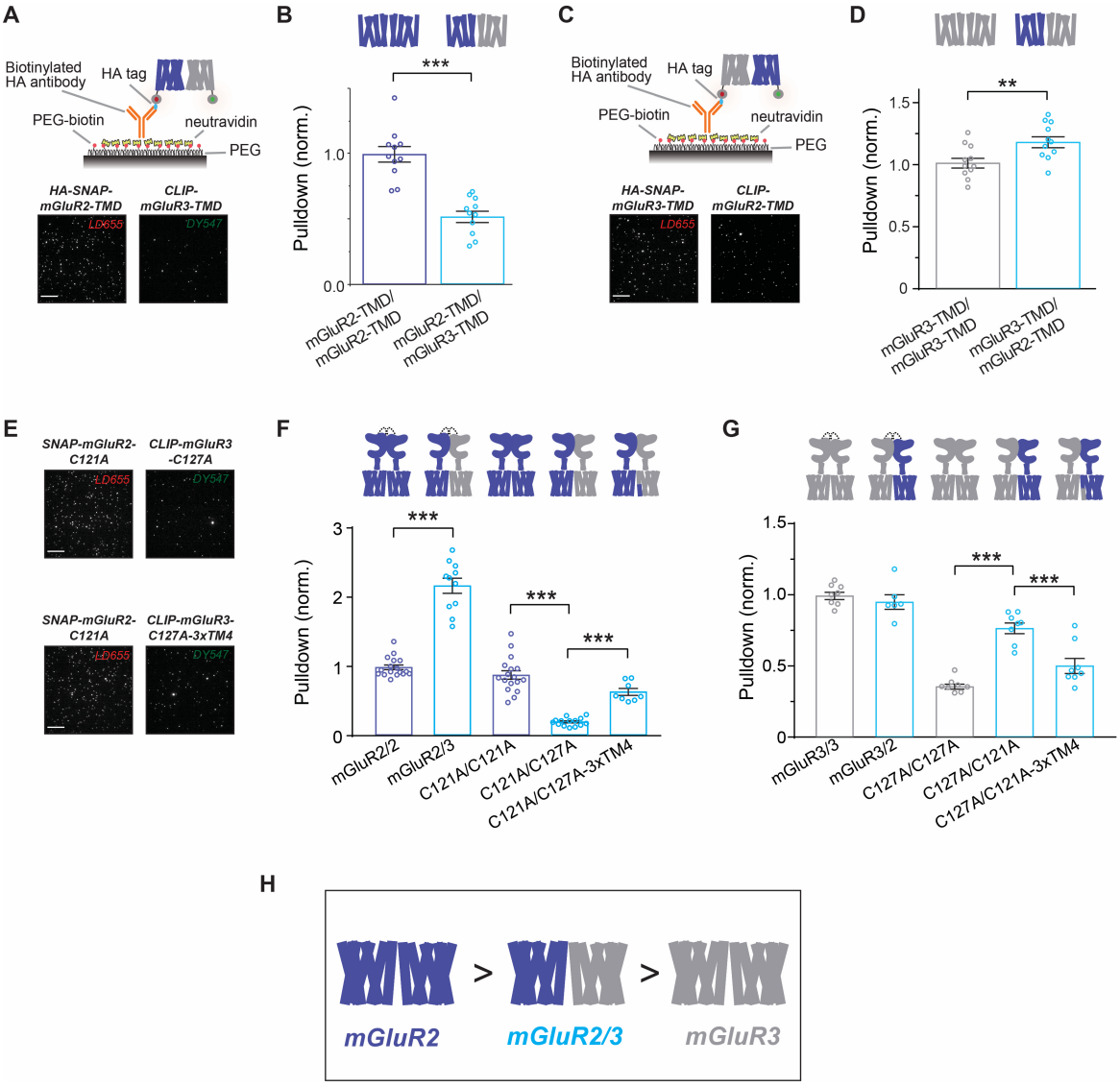

Figure 8

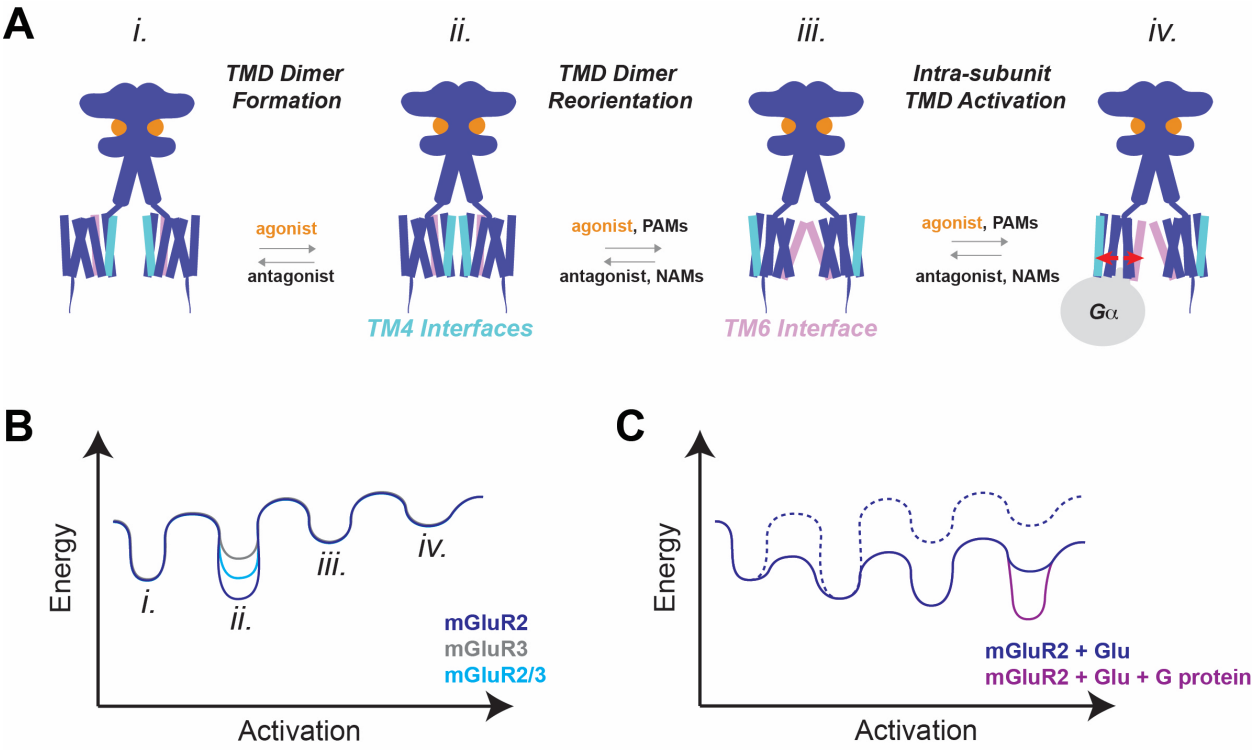

Supplementary Information for:

Differences in interactions between transmembrane domains tune the assembly and activation of metabotropic glutamate receptor subtypes

Jordana K. Thibado[1], Jean-Yves Tano[2], Joon Lee[3], Leslie Salas-Estrada[4], Davide Provasi[4], Alexa Strauss[5], Joao Marcelo Lamim Ribeiro[3], Guoqing Xiang[4], Johannes Broichhagen[6], Marta Filizola[3], Martin Lohse[2,7], Joshua Levitz[1,3,5]

[1] Physiology, Biophysics and Systems Biology Graduate Program, Weill Cornell Graduate School of Medical Sciences, New York, NY 10065

[2] Max Delbrück Center for Molecular Medicine, Berlin, 13125, Germany

[3] Department of Biochemistry, Weill Cornell Medicine, New York, NY 10065

[4] Department of Pharmacological Sciences, Icahn School of Medicine at Mount Sinai, New York, NY 10029

[5] Tri-Institutional PhD Program in Chemical Biology, New York, NY 10065

[6] Department of Chemical Biology, Forschungsinstitut für Molekulare Pharmakologie, Berlin, Germany.

[7] ISAR Bioscience Institute, Planegg-Munich, 82152, Germany

*To whom correspondence should be addressed: jtl2003@med.cornell.edu

Supplemental Figure Legends:

Figure 1—figure supplement 1. Further characterization of single molecule pulldown of mGluR TMDs: lack of subunit exchange in detergent.
(A) Cartoons of mGluR2-TMD constructs. Left, a SNAP-tagged TMD is labeled with LD655 and has an HA tag for antibody pulldown. Right, a CLIP-tagged TMD is labeled with CLIP-Surface 547.
(B) Schematic of experimental design in which cells are co-transfected with CLIP-mGluR2-TMD and SNAP-mGluR2-TMD constructs.
(C) Schematic of experimental design in which cells are transfected with either CLIP-mGluR2-TMD or SNAP-mGluR2-TMD and combined just prior to cell lysis.
(D) Representative single molecule images of co-transfected HA-SNAP-mGluR2-TMD labeled with LD655 (red circled spots) and CLIP-mGluR2-TMD labeled with CLIP-Surface 547 (green circled spots). Molecules were imaged with a 640 nm laser (left) and a 561 nm laser (right). Scale bar = 10 μm.
(E) Representative single molecule images of HA-SNAP-mGluR2-TMD labeled with LD655 (red circled spots) and CLIP-mGluR2-TMD labeled with CLIP-547 (green circled spots) mixed prior to cell lysis. Molecules were imaged with a 640 nm laser (left) and a 561 nm laser (right). Scale bar = 10 μm.
(F) Bar graph showing the total number of SNAP- or CLIP-mGluR2-TMD spots for the co-transfected condition and the condition in which cells were mixed just prior to lysis. Error bars represent s.e.m.

Figure 1—figure supplement 2. Inter-TMD dimerization propensities are maintained with C-terminal pulldown of mGluR2 and mGluR3 TMDs
(A) Top, schematic showing SiMPull strategy with C-terminal pulldown. Bottom, representative single molecule images of SNAP-mGluR2-TMD and SNAP-mGluR3-TMD pulled down via the C-terminal antibody. Scale bar = 10 μm.
(B) Bar graph showing that dimer propensities characteristic of SNAP-mGluR2-TMD and SNAP-mGluR3-TMD are maintained upon C-terminal pulldown. * indicates statistical significance (unpaired t-test, p = 0.0011). Number of movies analyzed for each condition is shown in parenthesis above each bar. Error bars represent s.e.m.

Figure 1—figure supplement 3. Ensemble FRET dequenching measurements show higher levels of inter-TMD FRET for mGluR2 compared to mGluR3
(A) Representative donor and acceptor images of HEK 293T cells before and after acceptor channel bleaching for SNAP-mGluR2-TMD.
(B) Summary bar graph showing a significantly higher donor recovery for mGluR2-TMD compared mGluR3-TMD and the prototypical class A GPCR, ß$_2$AR (unpaired t-tests; for ß$_2$AR vs. mGluR2-TMD, p = 1.3E-6; for mGluR2-TMD vs. mGluR3-TMD, p = 0.00060). Error bars represent s.e.m.

Figure 1—figure supplement 4. Representative images showing similar expression and single molecule pulldown for mGluR2 and mGluR3 cysteine mutant constructs.
(A) Representative HEK 293T cell images and single molecule images of SNAP-mGluR2-C121A and SNAP-mGluR3-C127A. Scale bar = 10 μm.
(B) Representative HEK 293T cell images and single molecule images of SNAP-mGluR2-C121A-mGluR3TMD and SNAP-mGluR3-C127A-mGluR2TMD. Scale bar = 10 μm.
(C) Quantification of surface expression from HEK 293T cell images shows similar expression between constructs. Error bars represent s.e.m.

Figure 2—figure supplement 1. mGluR TMD sequence conservation analysis
(A) Amino acid sequence alignments across the eight mGluR family members for all 7 TMs with outward-facing residues underlined and shown in purple.

(B) Top, homology models of mGluR2-TMD in grey with TM helices highlighted. Bottom left, homology models of mGluR2-TMD showing side chains of outward-facing residues in purple. Bottom right, top view of model with outward-facing residues.
(C) Quantification of percent conservation and identity across the 7 TM helices.
(D) TM4 sequence alignment shows the 3xTM4 motif in mGluR2 and mGluR3 is mostly conserved across species.

Figure 2—figure supplement 2. CG MD analysis of mGluR TMD dimerization.
(A) Coarse-grained (CG) representations of pairs of mGluR2 or mGluR3 simulated in a hydrated POPC bilayer.
(B-C) Reactive flux between the different macrostates identified by the PCCA+ analysis of the MSM analysis. Macrostates encompassing asymmetric dimers (i.e., tm1/tm4 and tm4/tm1) have been aggregated for the sake of clarity. The size of the nodes is proportional to the probability of each macrostate, and the thickness of the edges is proportional to the logarithm of the total reactive flux between the nodes. Microstates were defined by labels that contained the names of helices and loops of each protomer that formed more than 20 contacts with the other protomer, with contacts defined by a cutoff of 10 Å on the minimal distance over the beads of the residue. Total probability and fraction within a macrostate were calculated aggregating microstates if their labels contained the same helices but different loops, or if their labels were equivalent after swapping protomers. Microstates with total probability above 0.1% and macrostate fraction above 0.6% in either mGluR2 or mGluR3 are indicated below as part of the top macrostate they belong to for each receptor separately. (B) Reactive flux between the different macrostates identified for mGluR2; a consisting of 33.8% microstate (tm1,tm7)/tm4, 18.2% tm3/tm7, 7.9% (tm1,tm7)/tm3, 7.9% tm4/tm7, 5.1% (tm3,tm5)/tm7, 5.0% tm1/tm4, 4.5% tm5/tm7, 4.1% tm1/tm3, 3.9% tm1/tm5, 1.9% (tm3,tm5)/tm1, 1.5% (tm1,tm7)/(tm3,tm4), 1.0% (tm1,tm7)/(tm3,tm5), 0.6% (tm3,tm4)/tm1, 0.4% tm2/tm3, 0.3% tm4/tm4; b consisting of 32.2% microstate (tm1,tm7)/tm5, 8.5% (tm1,tm7)/(tm5,tm6), 6.1% tm2/tm5, 3.0% (tm2,tm7)/tm5, 2.4% (tm1,tm5)/tm2, 1.6% (tm5,tm7)/tm7, 1.0% (tm1,tm2)/(tm5,tm6), 1.0% (tm5,tm7)/tm2, 0.8% (tm5,tm6)/tm1; c consisting of 13.0% microstate (tm1,tm7)/(tm1,tm7), 8.8% (tm1,tm7)/tm7, 8.1% tm2/tm7, 6.0% tm7/tm7, 5.1% tm1/tm7, 4.4% (tm2,tm7)/tm7, 4.3% tm1/tm1, 3.8% (tm1,tm7)/tm1, 3.5% (tm1,tm2)/(tm1,tm7), 2.6% tm1/tm2, 1.9% (tm1,tm2)/tm7, 1.7% (tm2,tm7)/tm2, 1.5% (tm2,tm7)/(tm2,tm7), 1.5% (tm2,tm3)/tm7, 1.3% tm1/tm6, 1.2% (tm1,tm7)/tm2, 1.1% (tm1,tm2)/tm1, 0.8% (tm1,tm7)/(tm2,tm7), 0.8% (tm1,tm6)/tm1, 0.7% (tm3,tm4)/tm7, 0.7% tm2/tm2, 0.6% tm6/tm6, 0.3% (tm1,tm7)/(tm2,tm3); d consisting of 47.5% microstate tm3/tm6. (C) Reactive flux between the different macrostates identified for mGluR3; a' consisting of 17.6% microstate tm2/tm3, 10.9% tm3/tm7, 9.7% (tm1,tm7)/tm4, 9.1% (tm2,tm7)/tm3, 6.2% (tm1,tm7)/tm3, 5.2% (tm3,tm5)/tm2, 4.7% tm1/tm4, 4.3% (tm1,tm2)/tm4, 3.8% tm1/tm3, 3.5% (tm2,tm7)/tm4, 2.7% (tm3,tm5)/tm7, 2.4% tm4/tm7, 1.5% (tm3,tm5)/tm1, 1.4% (tm2,tm7)/(tm3,tm5), 1.2% (tm3,tm4)/tm1, 1.1% tm2/tm4, 1.1% (tm1,tm7)/(tm3,tm4), 0.8% (tm1,tm7)/tm2, 0.8% (tm1,tm7)/(tm2,tm3), 0.7% (tm2,tm7)/tm5, 0.7% (tm1,tm7)/(tm3,tm5), 0.5% (tm3,tm4)/tm7, 0.4% tm1/tm5, 0.4% tm2/tm5, 0.3% (tm2,tm3)/tm7, 0.3% (tm2,tm7)/tm2; b' consisting of 53.7% microstate (tm1,tm7)/(tm1,tm7), 15.1% (tm1,tm7)/tm7, 10.7% tm7/tm7, 4.3% tm1/tm7, 3.7% (tm1,tm7)/tm1, 3.3% tm2/tm7, 3.1% tm2/tm2, 1.4% (tm1,tm7)/(tm2,tm7), 1.3% (tm1,tm2)/(tm1,tm7), 0.6% (tm2,tm7)/tm7; c' consisting of 32.0% microstate tm3/tm4, 20.4% tm4/tm4, 16.0% (tm3,tm5)/tm4, 8.4% tm4/tm5; d' consisting of 56.6% microstate (tm1,tm7)/(tm5,tm6), 18.7% (tm5,tm6)/tm1, 8.6% (tm1,tm7)/tm5; **e'** consisting of 54.8% microstate (tm1,tm7)/tm4).
(D-G) Representative structures of the largest macrostates identified by MSM analysis of simulations of mGluR2 ((D) macrostate **c**, (E) macrostate **a**, and (F) macrostate **b**) and mGluR3 ((G) macrostate **a'**)). Representative coarse-grained configurations of the macrostates of mGluR2 or mGluR3 were clustered based on the RMSD of the corresponding interfaces. For a given interface, the least different configuration from all others was converted into an all-atom model using backward (Wassenaar et al., 2014). Interfacial residues within 4 Å are depicted as spheres. TM1: green, TM3: yellow, TM4: cyan, TM5: orange, TM7: red.

Figure 2—figure supplement 3. Symmetric TM4-TM4 interfaces for group II mGluR TMDs
(A-B) Representative structures of TM4-TM4 dimeric microstates for mGluR2 (A) and mGluR3 (B) showing conserved residues (cyan) at the cytosolic end that differ between subtypes.

Figure 2—figure supplement 4. Further analysis of dimerization of TM4 mutants of mGluR2 and mGluR3 TMD constructs.
(A) Representative HEK 293T cell images and single molecule images of SNAP-mGluR2-TMD-3xTM4 and SNAP-mGluR3-TMD-3xTM4. Scale bar = 10 μm.
(B) Quantification of surface expression from HEK 293T cell images shows similar expression between constructs.
(C) Bar graph showing the percentage of spots bleaching in two steps for SNAP-tagged constructs labeled with LD555. Single TM4 mutant constructs alter SNAP-mGluR2-TMD or SNAP-mGluR3-TMD dimerization. * indicates statistical significance (unpaired t-tests; for mGluR2-TMD vs. mGluR2-TMD-A677S, $p = 0.0029$; for mGluR2-TMD vs. mGluR2-TMD-A681F, $p = 0.0059$; for mGluR2-TMD vs. mGluR2-TMD-A685G, $p = 0.00013$; for mGluR3-TMD vs. mGluR3-TMD-S686A, $p = 0.00041$; for mGluR3-TMD vs. mGluR3-TMD-F690A, $p = 0.0048$; for mGluR3-TMD vs. mGluR3-TMD-G694A, $p = 0.029$). Number of movies analyzed for each condition is in parenthesis above each bar. Error bars represent s.e.m.
(D) Representative HEK 293T cell images of single TM4 mutant constructs. Scale bar = 10 μm.

Figure 2—figure supplement 5. TM1 and TM5 mutants do not alter TMD dimerization or function of mGluR2.
(A) Top left, homology model of mGluR2-TMD showing side chains of residues of interest in magenta. Top right, top view. Bottom, sequence alignment of TM4 residues in mGluR2 and mGluR3 showing outward-facing residues underlined and in purple.
(B) Bar graph showing the percentage of spots bleaching in two steps for SNAP-tagged constructs labeled with LD555. The mutations to TM4 do not alter dimerization compared to wild-type mGluR2-TMD (unpaired t-test, $p = 0.67$).
(C) Top left, cartoon model of mGluR1-TMD (PDB: 4OR2) showing side chains of residues of interest in blue and green. Top right, top view. Bottom, sequence alignment of TM1 residues in mGluR2 and mGluR3 showing outward-facing residues underlined and in purple.
(D) Top left, cartoon model of mGluR5-TMD (PDB: 6N52) showing side chains of residues of interest in red, orange and yellow. Top right, top view. Bottom, sequence alignment of TM5 residues in mGluR2 and mGluR3 showing outward-facing residues underlined and in purple.
(E) Bar graph showing the percentage of spots bleaching in two steps for SNAP-tagged constructs labeled with LD555. The mutations to TM1 and TM5 do not alter dimerization compared to wild-type mGluR2-TMD (unpaired t-tests; for mGluR2-TMD vs. mGluR2-TMD-F584I-G587T, $p = 0.14$; for mGluR2-TMD vs. mGluR2-TMD-A726S-G730I-A733T, $p = 0.38$). Number of movies analyzed for each condition is shown in parenthesis above each bar. Error bars represent s.e.m.

Figure 2—figure supplement 6. Further analysis of dimerization of TM4 mutants of mGluR2 and mGluR3 TMD constructs.
(A) Representative HEK 293T cell images and single molecule images of SNAP-mGluR2-mGluR3TMD and SNAP-mGluR3-mGluR2TMD. Scale bar = 10 μm.
(B) Representative HEK 293T cell images and single molecule images of SNAP-mGluR2-3xTM4 and SNAP-mGluR3-3xTM4. Scale bar = 10 μm.
(C) Representative HEK 293T cell images and single molecule images of SNAP-mGluR2-C121A-3xTM4 and SNAP-mGluR3-C127A-3xTM4. Scale bar = 10 μm.
(D) Quantification of surface expression from HEK 293T cell images shows similar expression between constructs.

(E) Bar graph showing the percentage of spots bleaching in two steps for SNAP-tagged constructs labeled with LD555. TMD chimera constructs and 3xTM4 mutant constructs do not alter dimerization of SNAP-mGluR2 or SNAP-mGluR3 (unpaired t-tests; for SNAP-mGluR2 vs. SNAP-mGluR2-mGluR3TMD, p = 0.085; for SNAP-mGluR2 vs. SNAP-mGluR2-3xTM4, p = 0.14; for SNAP-mGluR3 vs. SNAP-mGluR3-mGluR2TMD, p = 0.27; for SNAP-mGluR3 vs. SNAP-mGluR3-3xTM4, p = 0.37). Number of movies analyzed for each condition is shown in parenthesis above each bar. Error bars represent s.e.m.

Figure 3—figure supplement 1. Differences in TM4 residues mediate different activation properties of mGluR2 and mGluR3.

(A) Representative calcium imaging trace showing calcium responses induced by glutamate application from HEK 293T cells expressing mGluR2, a $G\alpha_{qi}$ protein chimera and GCaMP6f.

(B) Glutamate calcium imaging concentration response curves for mGluR2 (EC_{50} = 1.68 ± 0.03 μM) and mGluR3 (EC_{50} = 0.56 ± 0.06). All values are normalized to saturating (1 mM) glutamate. * indicates statistical significance (two-way ANOVA, p = 6.4E-5).

(C) Glutamate calcium imaging concentration response curves for mGluR2 and TM4 mutants mGluR2-A677S (EC_{50} = 1.94 ± 0.03), -A681F (EC_{50} = 1.79 ± 0.03), -A685G (EC_{50} = 2.01 ± 0.06). The mutants do not significantly differ from wild-type mGluR2 (two-way ANOVA; for mGluR2 vs. mGluR2-A677S, p = 0.96; for mGluR2 vs. mGluR2-A681F, p = 0.81; for mGluR2 vs. mGluR2-A685G, p = 0.64).

(D) Glutamate calcium imaging concentration response curves for mGluR3 and TM4 mutants mGluR3-S686A (EC_{50} = 5.12 ± 0.06), -F690A (EC_{50} = 9.59 ± 0.06), -G694A (EC_{50} = 4.66 ± 0.03). * indicates statistical significance (two-way ANOVA; for mGluR3 vs. mGluR3-S686A, p = 2.2E-8; for mGluR3 vs. mGluR3-F690A, p = 2.6E-14; for mGluR3 vs. mGluR3-G694A, p = 4.9E-10).

(E) Glutamate calcium imaging concentration response curves for mGluR2 and TM1 mutant mGluR2-F584I-G587T (EC_{50} = 2.50 ± 0.06) and TM5 mutant mGluR2-A726S-G730I-A733T (EC_{50} = 2.05 ± 0.10). All values are normalized to saturating (1 mM) glutamate. The mutants do not significantly differ from wild-type mGluR2 (two-way ANOVA; for mGluR2 vs. mGluR2-F584I-G587T, p = 0.29; for mGluR2 vs. mGluR2-A726S-G730I-A733T, p = 0.71).

(F) Representative calcium imaging trace showing calcium responses induced by LY487379 and glutamate application from HEK 293T cells expressing mGluR2, a $G\alpha_{qi}$ protein chimera and GCaMP6f.

(G) Bar graph showing the percentage of spots bleaching in two steps for SNAP-tagged constructs labeled with LD555. * indicates statistical significance (unpaired t-test, p = 4.7E-8). mGluR3-TMD is not significantly different from mGluR3-TMD-3xTM4_W (unpaired t-test, p = 0.85).

(H) Representative single molecule images of SNAP-mGluR2-TMD-3xTM4_W and SNAP-mGluR3-TMD-3xTM4_W and representative HEK 293T cell images of SNAP-mGluR2-3xTM4_W and SNAP-mGluR3-3xTM4_W. Scale bar = 10 μm.

(I) Quantification of surface expression from HEK 293T cell images shows similar expression between constructs.

Figure 4—figure supplement 1. Differences in TM4 residues do not alter inter-LBD conformational dynamics

(A) Representative LBD FRET trace showing FRET decreases in response to glutamate application.

(B) Glutamate LBD FRET concentration response curves for mGluR2 (EC_{50} = 11 ± 0.02), mGluR2-3xTM4 (EC_{50} = 11 ± 0.02), mGluR3 (EC_{50} = 0.64 ± 0.10) and mGluR3-3xTM4 (EC_{50} = 0.67 ± 0.05). All values are normalized to saturating (1 mM) glutamate. The mutants do not differ from their wild-type counterparts (two-way ANOVA; for mGluR2 vs. mGluR2-3xTM4, p = 0.17; for mGluR3 vs. mGluR3-3xTM4, p = 0.60).

(C) Representative mGluR2-3xTM4 LBD FRET trace showing a FRET response induced by glutamate application and no change induced by antagonist LY34 application.

(D) Quantification of LBD basal FRET. Error bars represent s.e.m.

Figure 4—figure supplement 2. Characterization of inter-TMD FRET sensor in mGluR2 and mGluR3.
(A) Bar graph showing that 1:3 donor:acceptor dye labeling is the optimal ratio to detect FRET changes for the inter-TMD FRET sensor. * indicates statistical significance (unpaired t-tests; for 1:2 vs. 1:3, p = 0.0023; for 1:3 vs. 1:5, p = 0.011).
(B) Representative FRET trace shows stability of signal over a 2-minute glutamate application.
(C) Bar graph showing maximum FRET change from saturating glutamate observed for mGluR2 compared to mGluR3. * indicates statistical significance (unpaired t-test, p = 0.00066).
(D) A FRET change does not occur when only donor dye (JF 549) is labeled.
(E) A FRET change does not occur when only acceptor dye (JF 646) is labeled.

Figure 4—figure supplement 3. Characterization of inter-TMD conformational dynamics in response to orthosteric and allosteric drugs.
(A) Representative FRET trace for mGluR3 shows concentration-dependent glutamate responses.
(B) Representative FRET trace for mGluR2 shows concentration-dependent glutamate responses.
(C) Representative FRET trace for mGluR2 shows application of antagonist LY34 blocks a glutamate-induced FRET response.
(D) Representative FRET trace for mGluR3 shows application of antagonist LY34 blocks a glutamate-induced FRET response.
(E) Representative calcium imaging trace showing calcium responses induced by glutamate application from a HEK 293T cell expressing mGluR2, a G protein chimera and GCaMP6f. A second glutamate application is blocked by application of antagonist LY34.
(F) Representative calcium imaging trace showing calcium responses induced by glutamate application from a HEK 293T cell expressing mGluR3, a G protein chimera and GCaMP6f. A second glutamate application is blocked by application of antagonist LY34.
(G) Representative FRET trace for mGluR3 shows application of negative allosteric modulator MNI 137 partially blocks a glutamate-induced FRET response.
(H) Representative calcium imaging trace showing calcium responses induced by glutamate application from a HEK 293T cell expressing mGluR2, a G protein chimera and GCaMP6f. A second glutamate application is blocked by application of negative allosteric modulator MNI 137.
(I) Representative calcium imaging trace showing calcium responses induced by glutamate application from a HEK 293T cell expressing mGluR3, a G protein chimera and GCaMP6f. A second glutamate application is blocked by application of negative allosteric modulator MNI 137.
(J) Quantification of basal inter-TMD FRET response upon LY34 or MNI 137 application in mGluR3-Halo-ICL2. * indicates statistical significance (unpaired t-test, p = 0.00043).
(K) Representative patch clamp recording showing sensitivity in response to LY34 application in the absence of glutamate for mGluR3, indicating basal receptor signaling.
(L) Quantification of basal activity in patch clamp recordings shows no significant difference between LY34 and MNI 137.

Figure 5—figure supplement 1. Further characterization of TM6 in mGluR activation.
(A) Representative HEK 293T cell images of mGluR2 TM6 mutants. Scale bar = 10 μm.
(B) Quantification of surface expression from HEK 293T cell images shows similar expression between constructs.
(C) Bar graph showing the percentage of spots bleaching in two steps for SNAP-tagged constructs labeled with LD555. * indicates statistical significance (unpaired t-tests; for SNAP-mGluR2-TMD vs. SNAP-mGluR2-TMD-I779A, p = 0.00074; for SNAP-mGluR2-TMD vs. SNAP-mGluR2-TMD-I779W, p = 0.00038; for SNAP-mGluR2-TMD vs. SNAP-mGluR2-TMD-P778A, p = 0.00047; for SNAP-mGluR2-TMD vs. SNAP-mGluR2-TMD-P778A-I779A, p = 6.4E-5). Number of movies analyzed for each condition is shown in parenthesis above each bar. Error bars represent s.e.m.

(D) Glutamate calcium imaging concentration response curves for mGluR2 and TM6 mutants mGluR2-I779A (EC_{50} = 18.66 ± 0.08), -I779W (EC_{50} = 4.37 ± 0.04), -P778A (EC_{50} = 0.85 ± 0.1), -P778A-I779A (EC_{50} = 5.09 ± 0.08). * indicates statistical significance (two-way ANOVA; for mGluR2 vs. mGluR2-I779A, p = 1.2E-10; for mGluR2 vs. mGluR2-I779W, p = 0.003; for mGluR2 vs. mGluR2-P788A-I779A, p = 0.0015). mGluR2-P788A is not significantly different from mGluR2 (two-way ANOVA, p = 0.27).
(E) Representative calcium imaging trace showing calcium responses induced by glutamate application from HEK 293T cells expressing mGluR2-I779A, a G protein chimera and GCaMP6f.
(F) Representative calcium imaging trace showing calcium responses induced by glutamate application from HEK 293T cells expressing mGluR3-I788A, a G protein chimera and GCaMP6f.
(G) Representative FRET trace for mGluR2-I779A.
(H) Representative FRET trace for mGluR3-I788A.

Figure 6—figure supplement 1. Analysis of ligand induced inter-TMD rearrangement by SiMPull.
(A) Bar graph showing the percentage of spots bleaching in two steps for SNAP-tagged constructs labeled with LD555. Application of PAM or NAM does not alter mGluR2-TMD dimerization (unpaired t-test; for mGluR2-TMD vs. mGluR2-TMD + TASP, p = 0.87; for mGluR2-TMD vs. mGluR2-TMD + MNI 137, p = 0.96).
(B) Bar graph showing the percentage of spots bleaching in two steps for SNAP-tagged constructs labeled with LD555. Application of PAM significantly increases dimerization for mGluR2-TMD-3xTM4 compared to no drug and NAM conditions. * indicates statistical significance (unpaired t-test; for mGluR2-TMD-3xTM4 vs. mGluR2-TMD-3xTM4 + TASP, p = 5.6E-7; for mGluR2-TMD-3xTM4 + TASP vs. mGluR2-TMD-3xTM4 + MNI 137, p = 0.0011).
(C) Bar graph showing the percentage of spots bleaching in two steps for SNAP-tagged constructs labeled with LD555. Application of NAM significantly increases dimerization for mGluR2-TMD-I779A compared to no drug and NAM conditions. * indicates statistical significance (unpaired t-test; for mGluR2-TMD-I779A + TASP vs. mGluR2-TMD-I779A + MNI 137, p = 0.0017). mGluR2-TMD-I779A is not significantly different from mGluR2-TMD-I779A + TASP (unpaired t-test, p = 0.40).
(D) Bar graph showing the percentage of spots bleaching in two steps for SNAP-tagged constructs labeled with LD555. Application of PAM or NAM does not alter mGluR2-TMD-3xTM4-I779A dimerization (unpaired t-tests; for mGluR2-TMD-3xTM4-I779A vs. mGluR2-TMD-3xTM4-I779A + TASP, p = 0.86; for mGluR2-TMD-3xTM4-I779A vs. mGluR2-TMD-3xTM4-I779A + MNI 137, p = 0.25).
(E) Bar graph showing the percentage of spots bleaching in two steps for SNAP-tagged constructs labeled with LD555. Application of ligand does not alter mGluR2-C121A dimerization (unpaired t-test; for mGluR2-C121A vs. mGluR2-C121A + TASP, p = 0.56; for mGluR2-C121A vs. mGluR2-C121A + MNI 137, p = 0.97; for mGluR2-C121A vs. mGluR2-C121A + Glu, p = 0.44).
(F) Bar graph showing the percentage of spots bleaching in two steps for SNAP-tagged constructs labeled with LD555. Application of PAM and glutamate significantly increases dimerization for mGluR2-C121A-3xTM4 compared to no drug and NAM conditions. * indicates statistical significance (unpaired t-tests; for mGluR2-C121A-3xTM4 vs. mGluR2-C121A-3xTM4 + TASP, p = 0.0016; for mGluR2-C121A-3xTM4 + TASP vs. mGluR2-C121A-3xTM4 + MNI 137, p = 0.00086; for mGluR2-C121A-3xTM4 + MNI 137 vs. mGluR2-C121A-3xTM4 + Glu, p = 0.0013).
(G) Bar graph showing the percentage of spots bleaching in two steps for SNAP-tagged constructs labeled with LD555. Application of NAM significantly increases dimerization for mGluR2-C121A-I779A compared to no drug, PAM, and glutamate conditions. * indicates statistical significance (unpaired t-test; for mGluR2-C121A-I779A vs. mGluR2-C121A-I779A + TASP, p = 0.19; for mGluR2-C121A-I779A + TASP vs. mGluR2-C121A-I779A + MNI 137, p = 4.5E-5; for mGluR2-C121A-I779A + MNI 137 vs. mGluR2-C121A-I779A + Glu, p = 0.00093).
(H) Bar graph showing the percentage of spots bleaching in two steps for SNAP-tagged constructs labeled with LD555. Application of ligand does not alter mGluR2-C121A-3xTM4-I779A dimerization (unpaired t-tests; for mGluR2-C121A-3xTM4-I779A vs. mGluR2-C121A-3xTM4-I779A + TASP, p = 0.33; for

mGluR2-C121A-3xTM4-I779A vs. mGluR2-C121A-3xTM4-I779A + MNI 137, p = 0.88; for mGluR2-C121A-3xTM4-I779A vs. mGluR2-C121A-3xTM4-I779A + Glu, p = 0.79).
(I) Bar graph showing the percentage of spots bleaching in two steps for SNAP-tagged constructs labeled with LD555. Application of glutamate significantly increases dimerization for mGluR3-C127A compared to no drug and LY34 conditions. * indicates statistical significance (unpaired t-test, p = 8.8E-5). Application of LY34 did not alter dimerization compared to the no drug condition (unpaired t-test, p = 0.24).
(J) Bar graph showing the percentage of spots bleaching in two steps for SNAP-tagged constructs labeled with LD555. Application of ligand does not alter mGluR3-C127A-3xTM4 dimerization (unpaired t-tests; for mGluR3-C127A-3xTM4 vs. mGluR3-C127A-3xTM4 + LY34, p = 0.78; for mGluR3-C127A-3xTM4 vs. mGluR3-C127A-3xTM4 + Glu, p = 0.38).
(K) Bar graph showing the percentage of spots bleaching in two steps for SNAP-tagged constructs labeled with LD555. Application of LY34 significantly increases dimerization for mGluR3-C127A-I788A compared to no drug and glutamate conditions. * indicates statistical significance (unpaired t-tests; for mGluR3-C127A-I788A vs. mGluR3-C127A-I788A + LY34, p = 0.00053; for mGluR3-C127A-I788A + LY34 vs. mGluR3-C127A-I788A + Glu, p = 0.00065). Number of movies analyzed for each condition is shown in parenthesis above each bar. Error bars represent s.e.m.

Figure 7-figure supplement 1. Further analysis of homo- and hetero-dimerization propensities of isolated group II mGluR TMDs.
(A) Representative images showing fluorophore labeled receptors on the surface of HEK 293T cells.
(B) Quantification of fluorescence intensities across co-expression conditions showing comparable expression conditions used for 2-color SiMPull analysis.
(C) Representative SiMPull images showing background levels of pulldown from lysates containing only CLIP-tagged constructs lacking an HA tag.
(D) Quantification of the number of immobilized spots for a representative experiment showing that SNAP-mGluR2-TMD is able to pull down a substantially higher amount of CLIP-mGluR2-TMD than CLIP-mGluR3-TMD. Background values for the CLIP construct expressed alone for each condition are shown as black bars.
(E) Same as (A-D) but with SNAP-mGluR3-TMD conditions.

Figure 7-figure supplement 2. Further analysis of homo- and hetero-dimerization propensities of isolated full-length group II mGluRs.
(A) Quantification of fluorescence intensities across co-expression conditions showing comparable expression conditions used for 2-color SNAP-mGluR2 SiMPull analysis.
(B) Quantification of the number of immobilized spots for a representative SNAP-mGluR2 SiMPull experiment. Background values for the CLIP construct expressed alone for each condition are shown as black bars.
(C) Quantification of fluorescence intensities across co-expression conditions showing comparable expression conditions used for 2-color SNAP-mGluR3 SiMPull analysis.
(D) Quantification of the number of immobilized spots for a representative SNAP-mGluR3 SiMPull experiment. Background values for the CLIP construct expressed alone for each condition are shown as black bars.

Figure 1-figure supplement 1

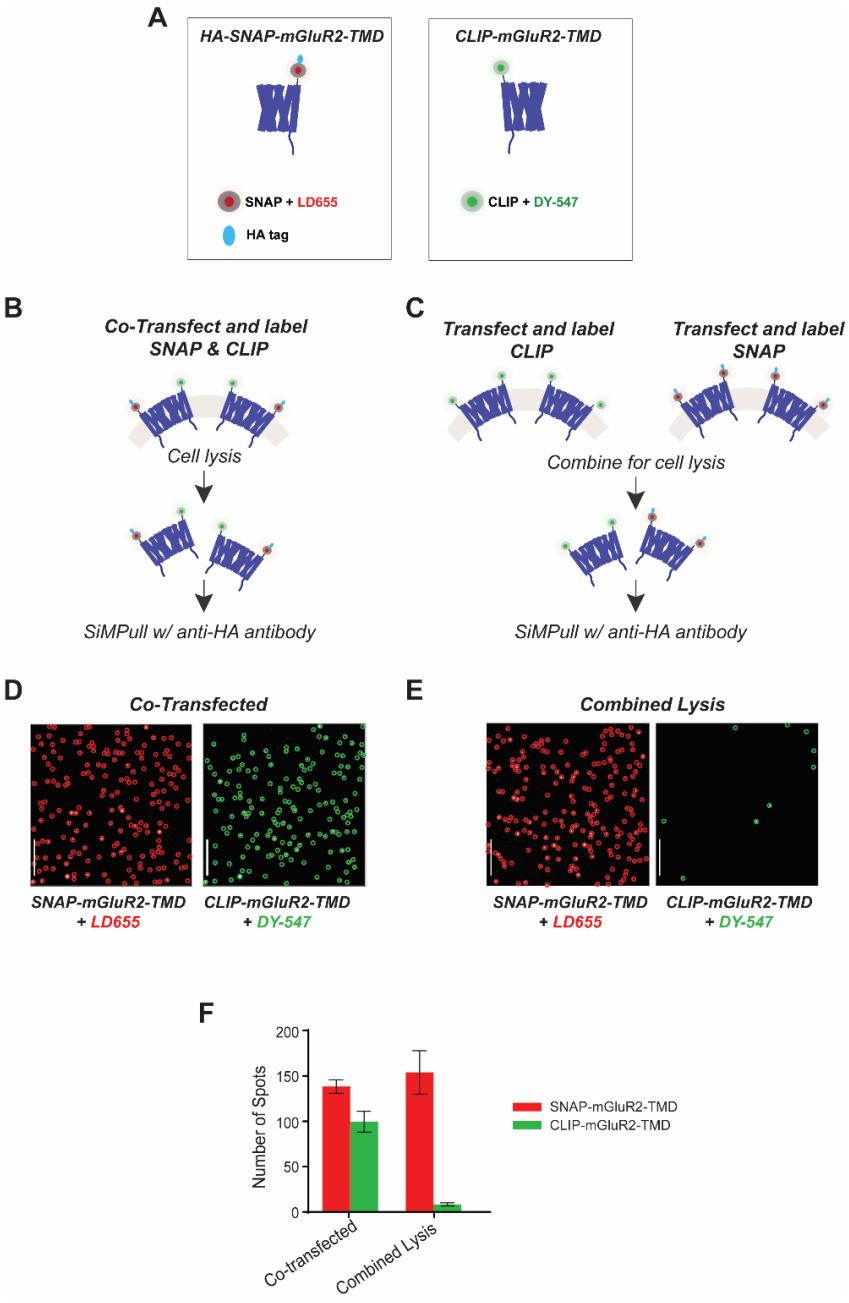

Figure 1-figure supplement 2

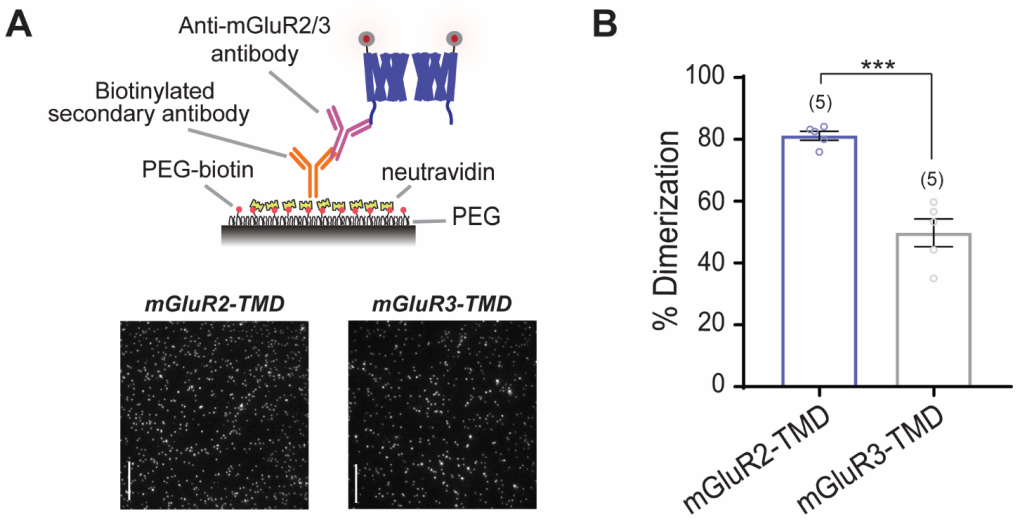

Figure 1-figure supplement 3

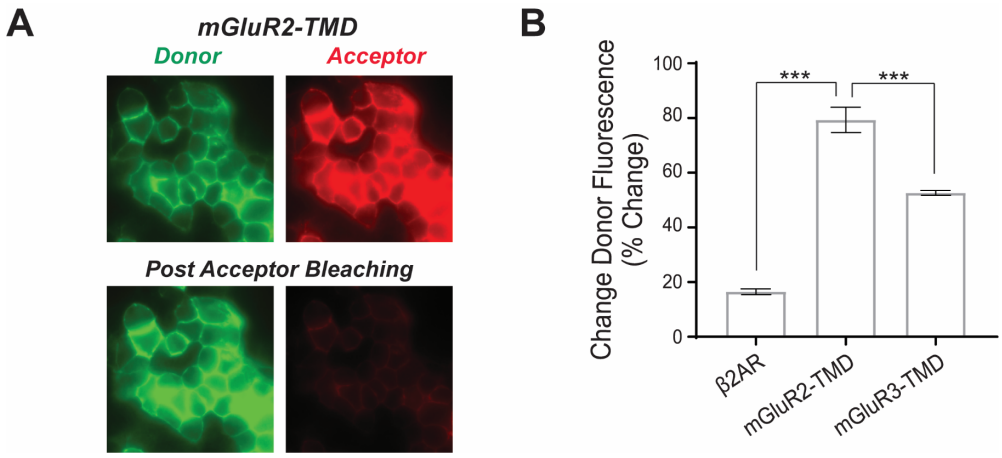

Figure 1-figure supplement 4

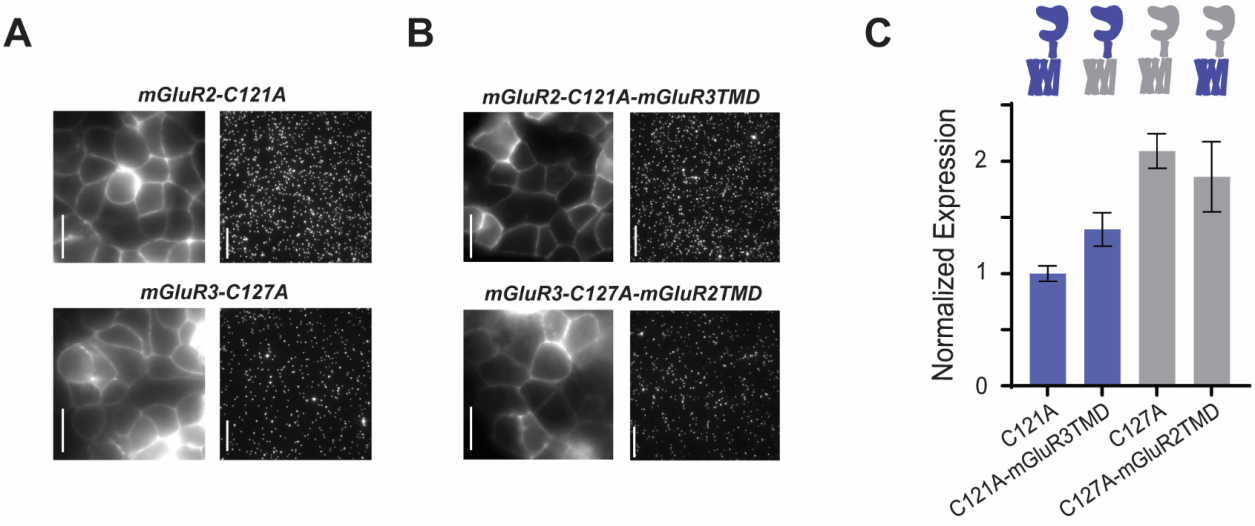

Figure 2-figure supplement 1

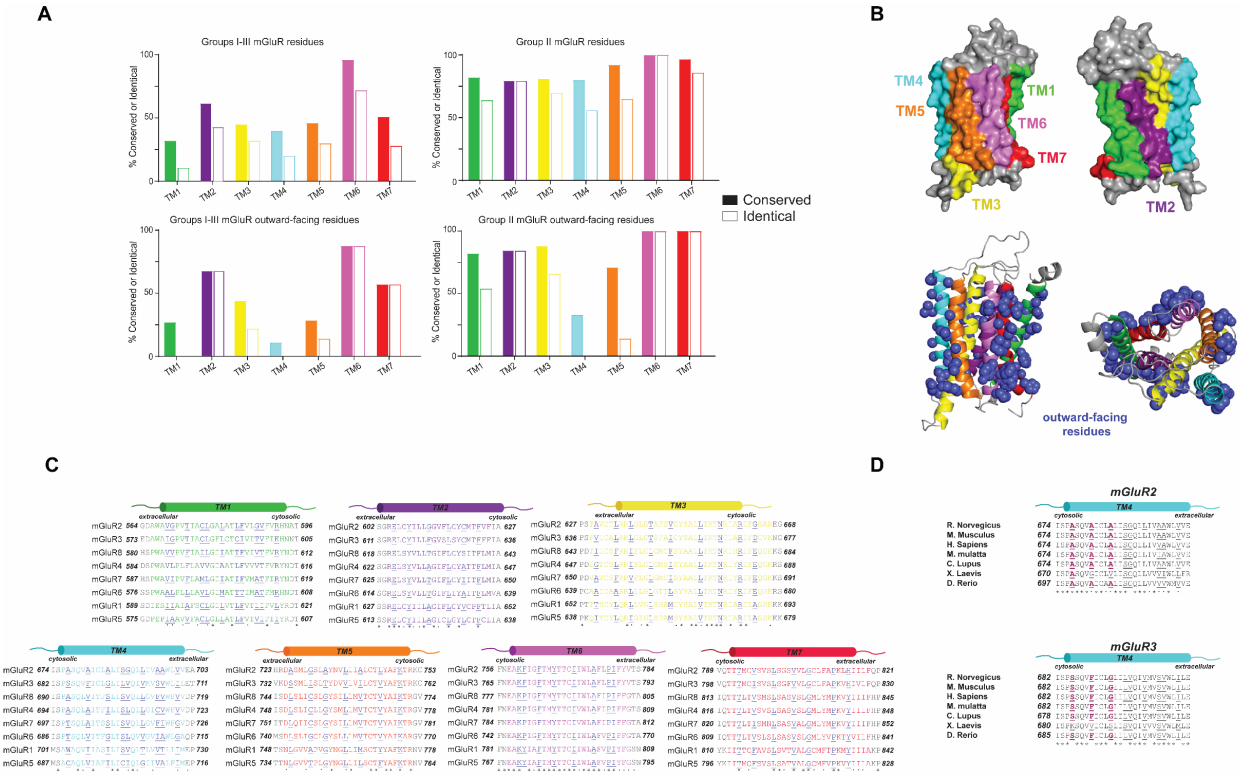

Figure 2-figure supplement 2

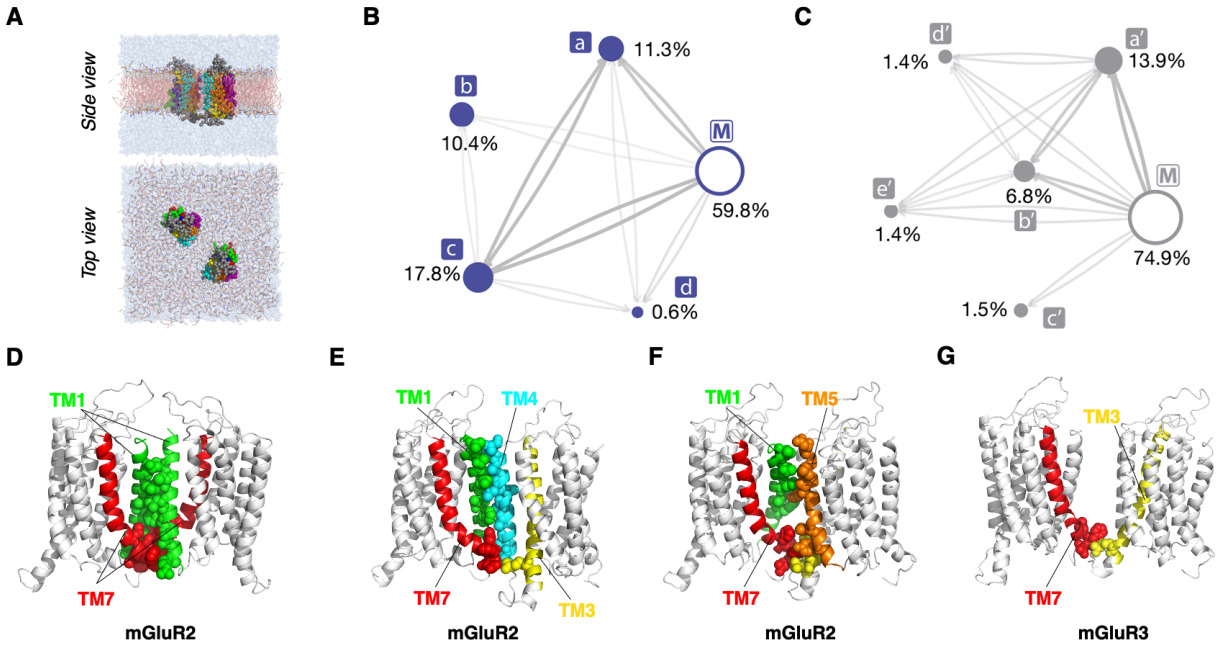

Figure 2-figure supplement 3

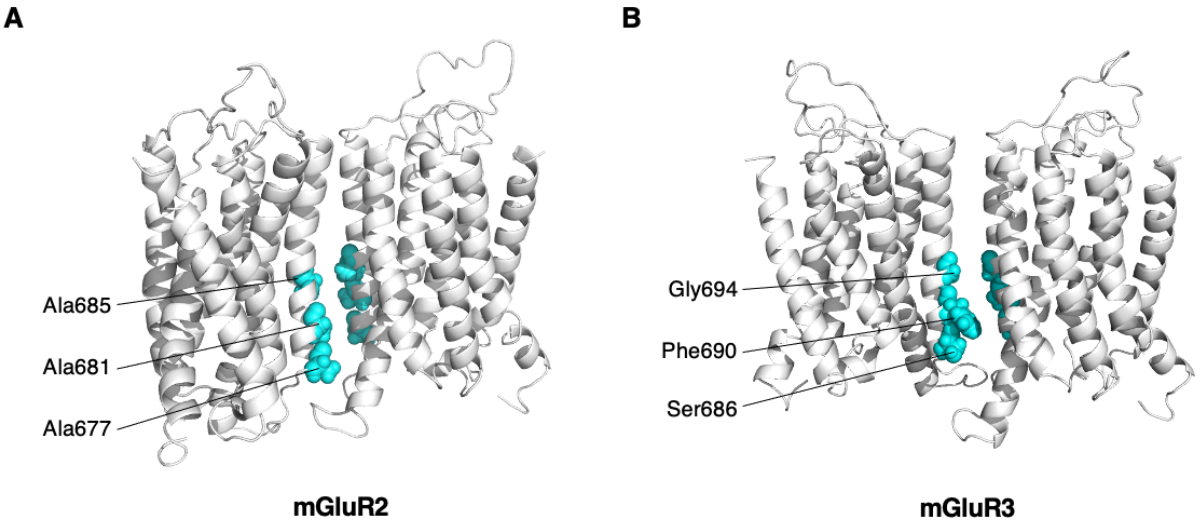

Figure 2-figure supplement 4

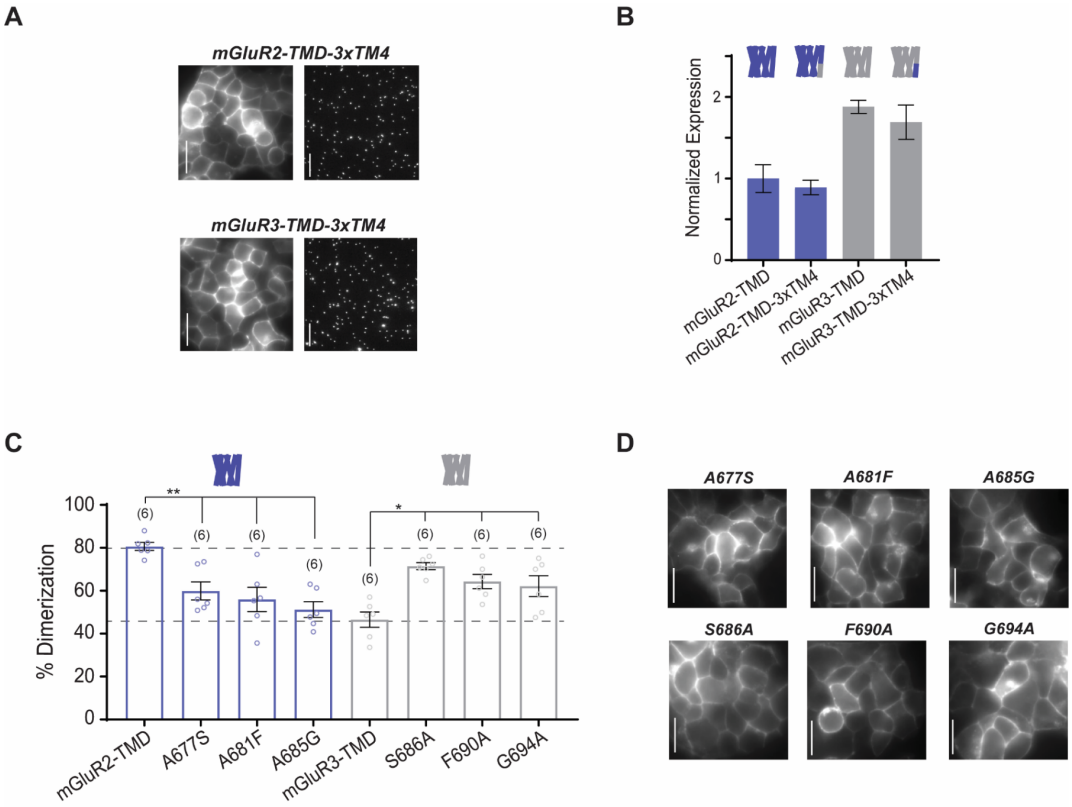

Figure 2-figure supplement 5

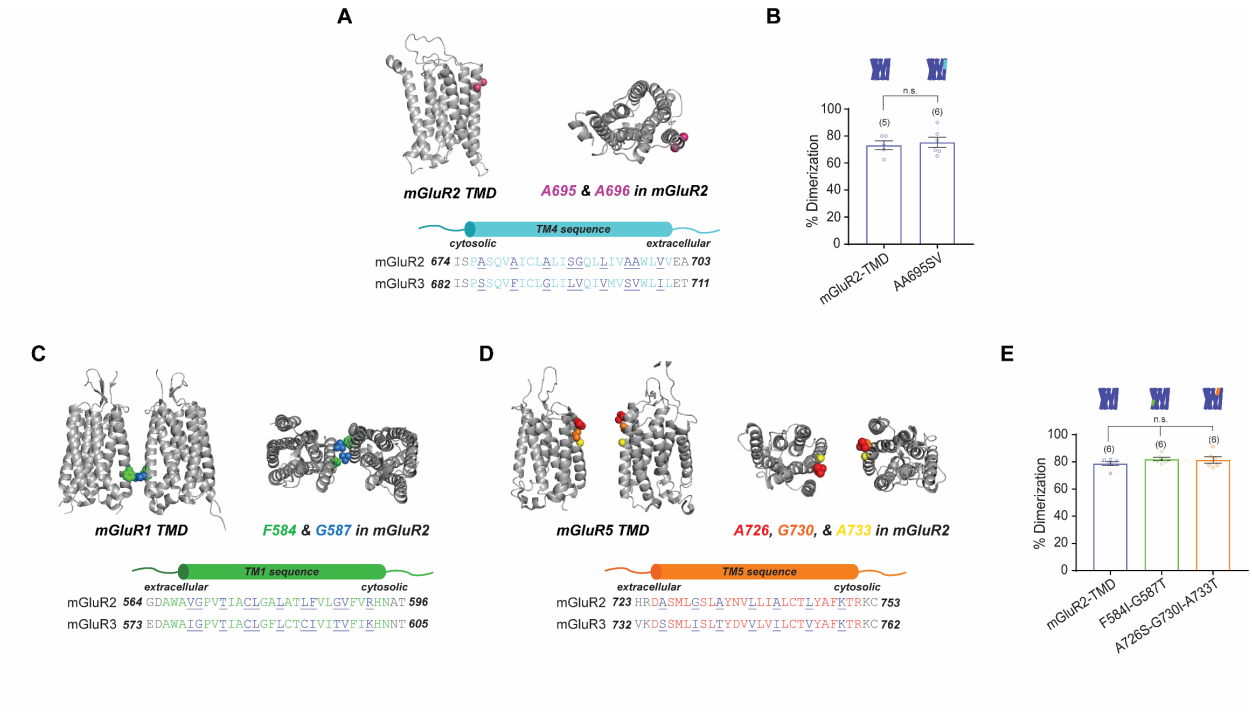

Figure 2-figure supplement 6

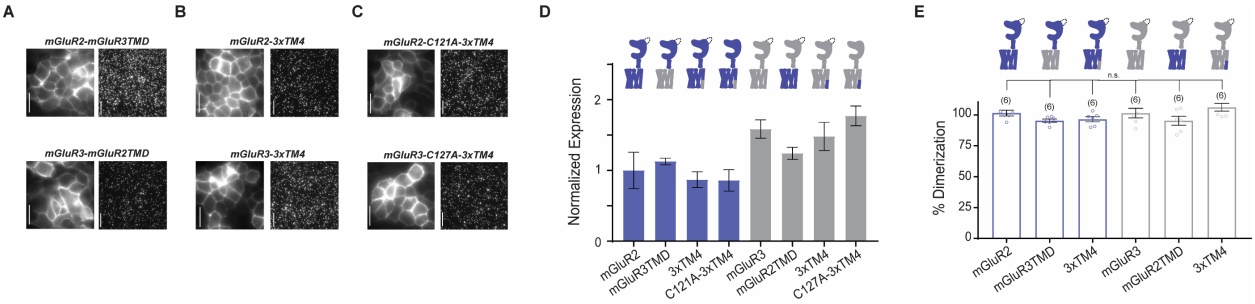

Figure 3-figure supplement 1

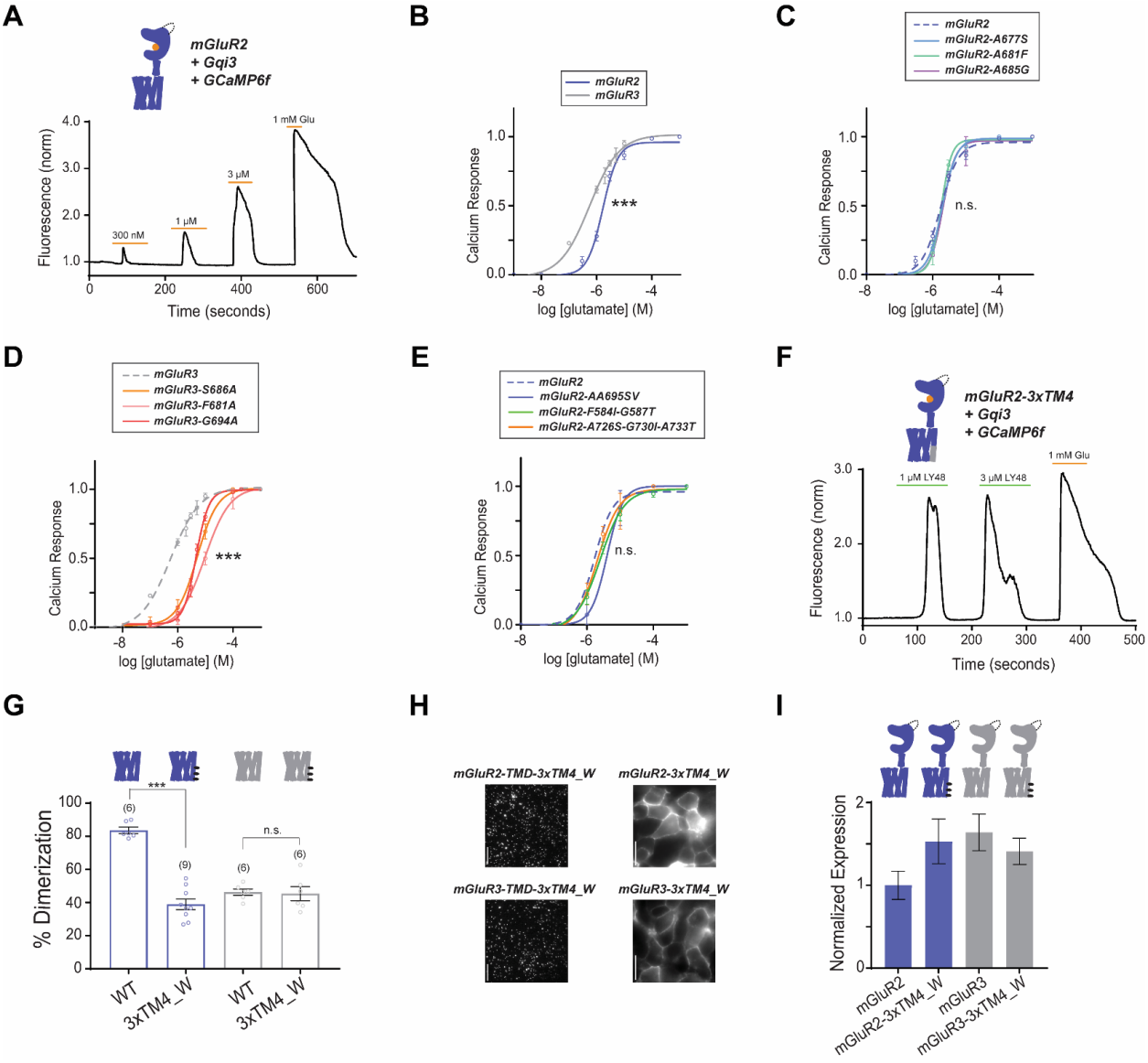

Figure 4-figure supplement 1

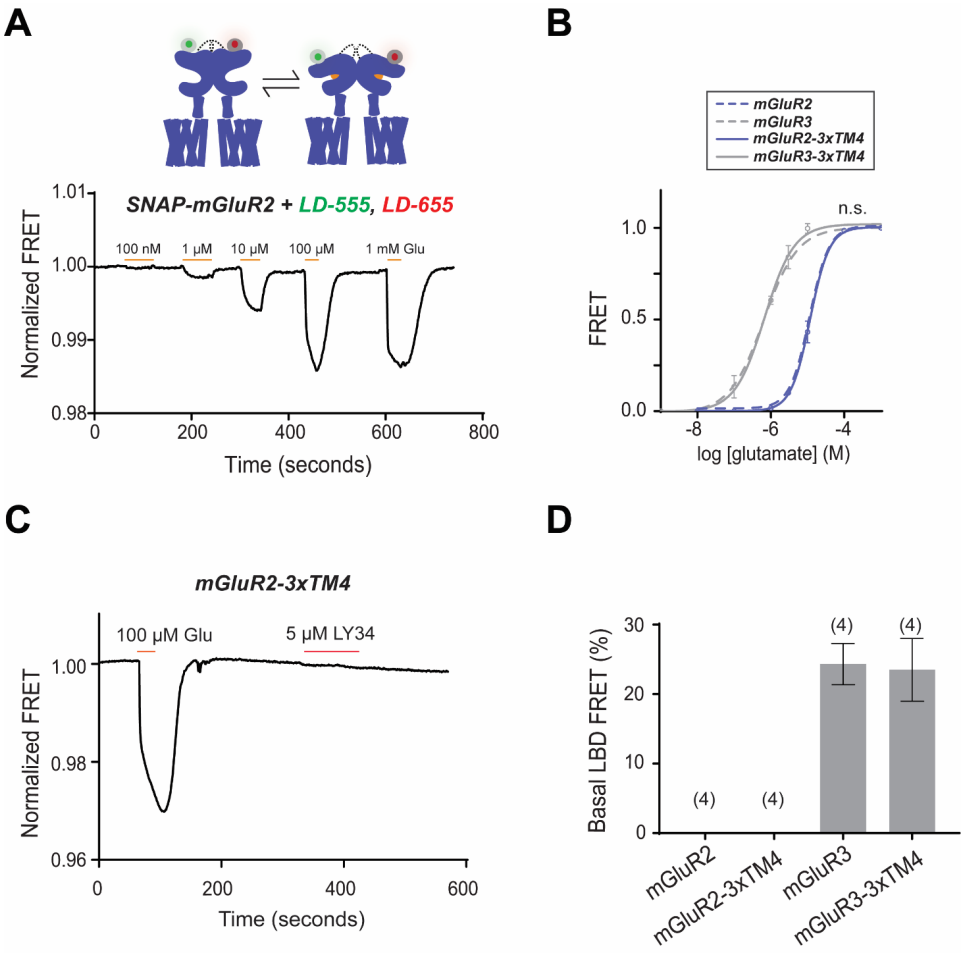

Figure 4-figure supplement 2

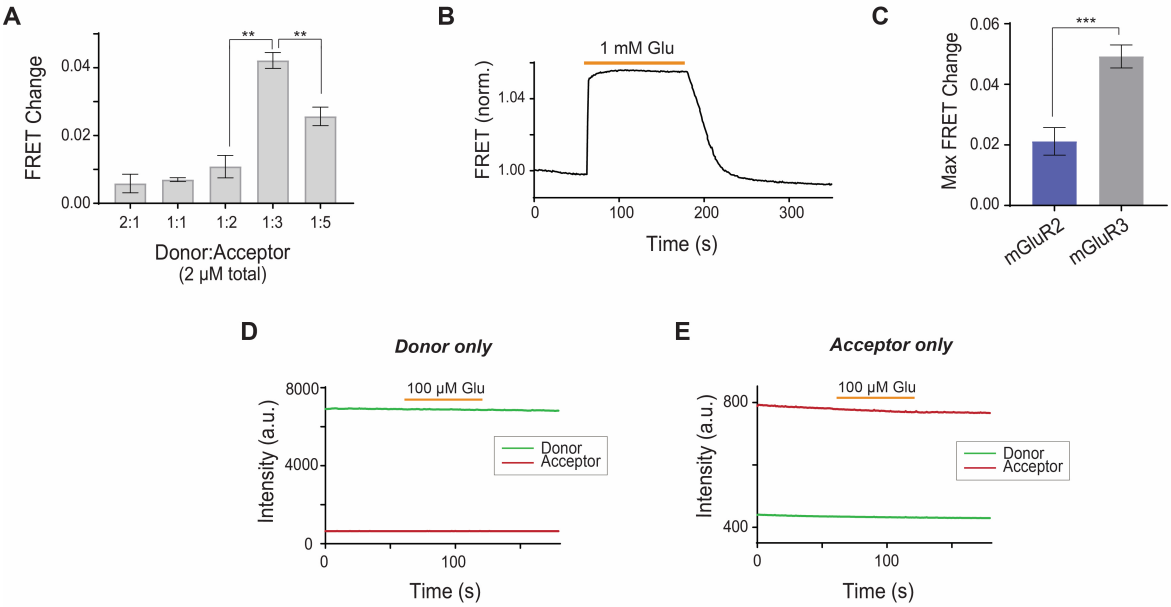

Figure 4-figure supplement 3

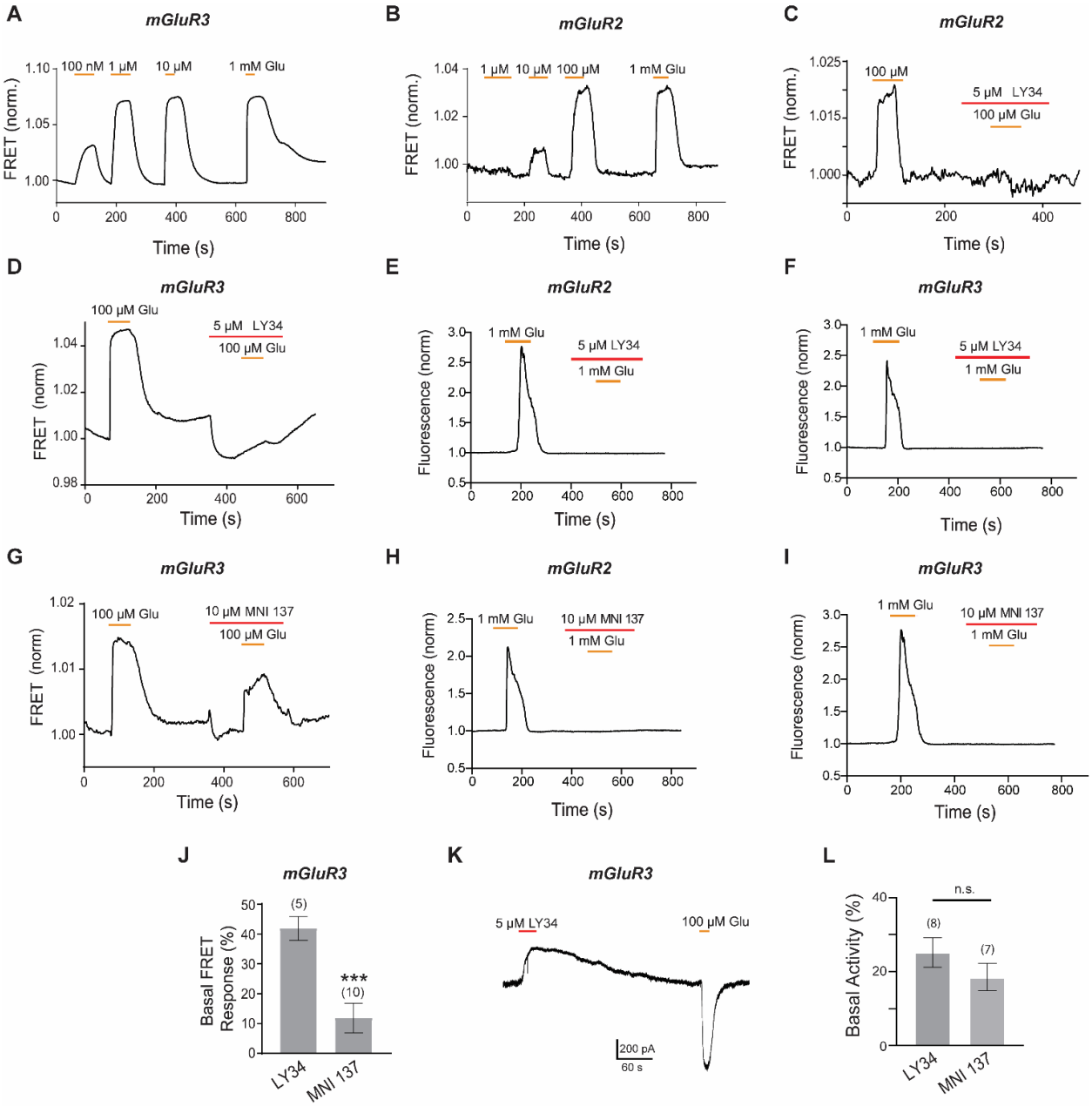

Figure 5-figure supplement 1

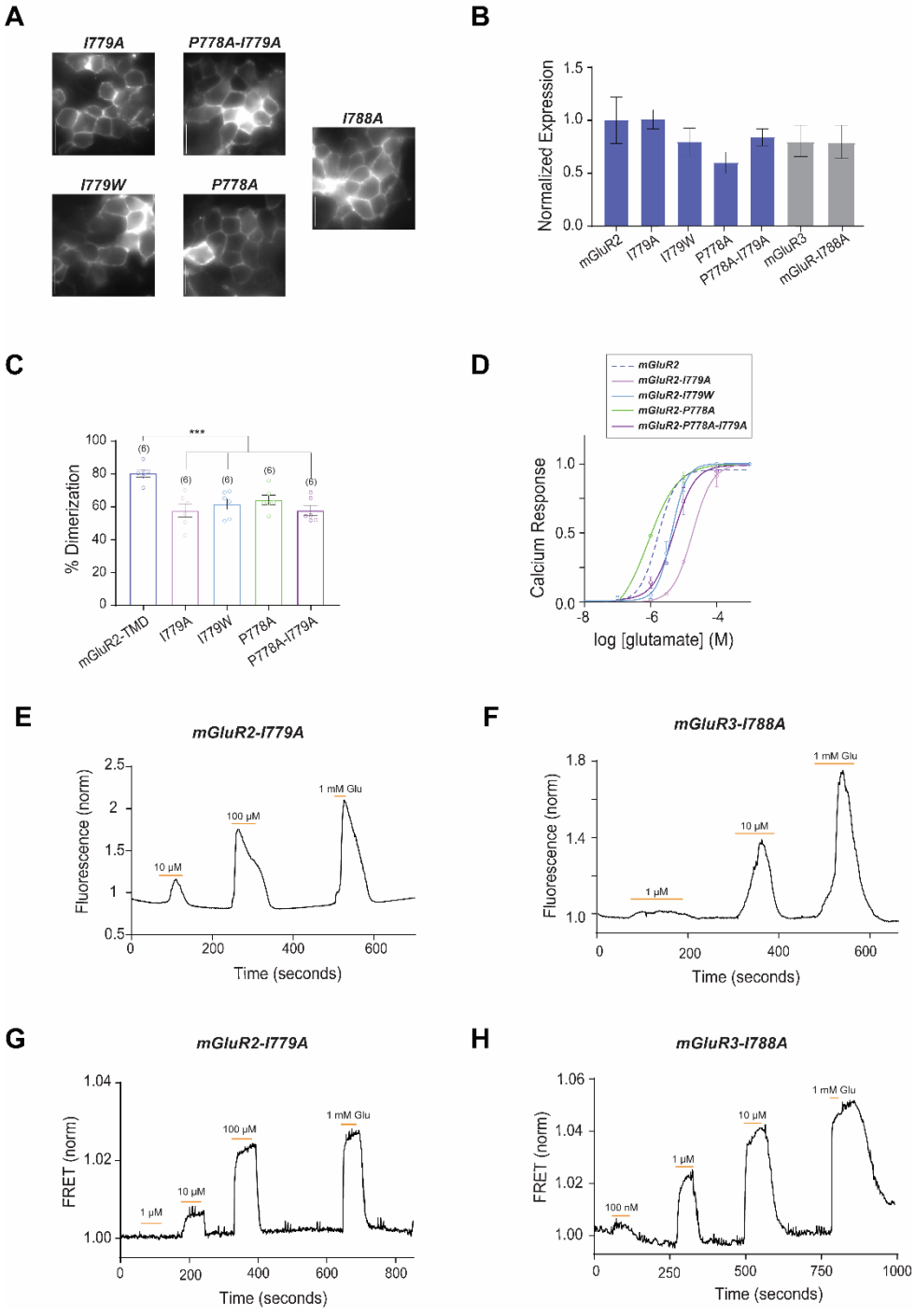

Figure 6-figure supplement 1

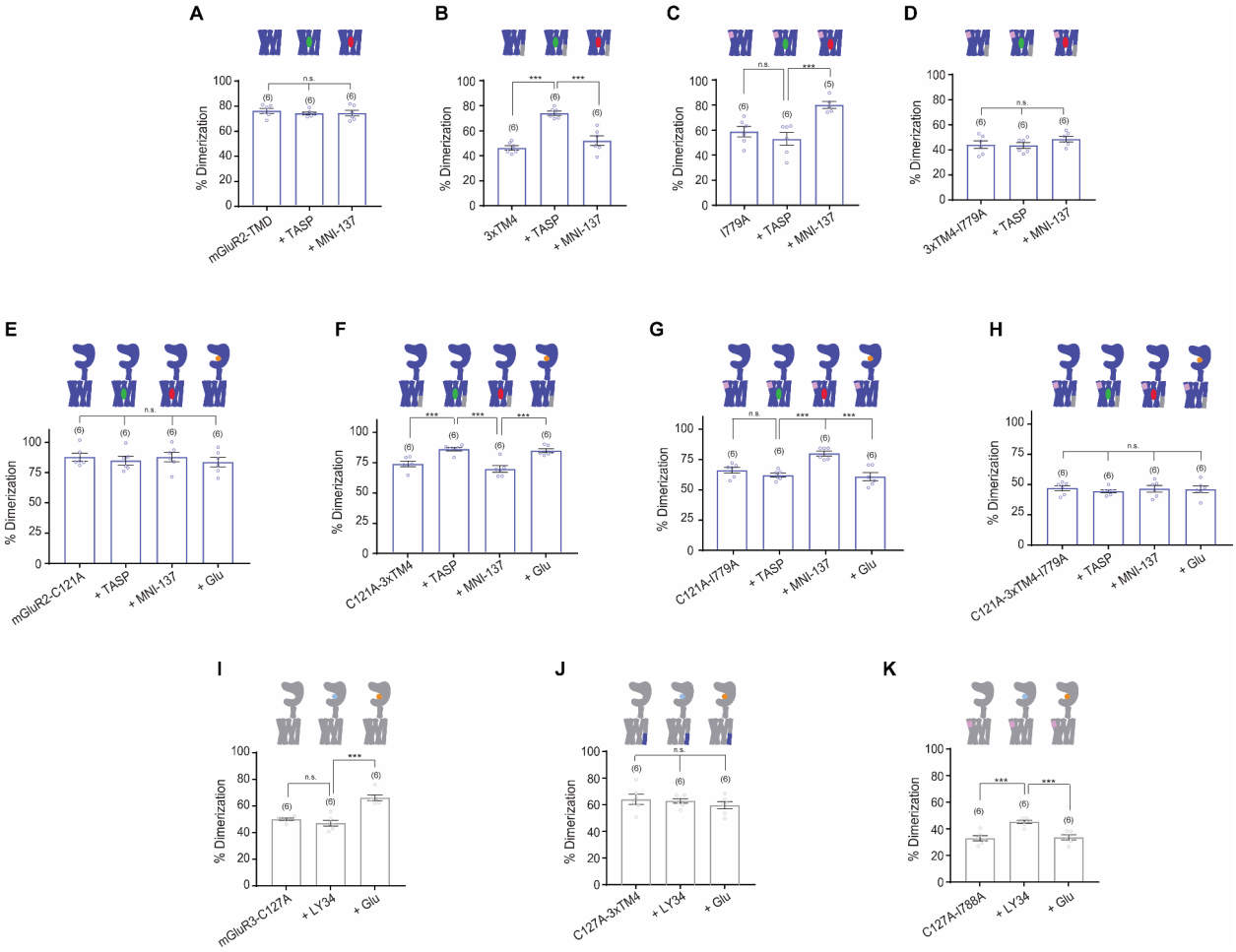

Figure 7-figure supplement 1

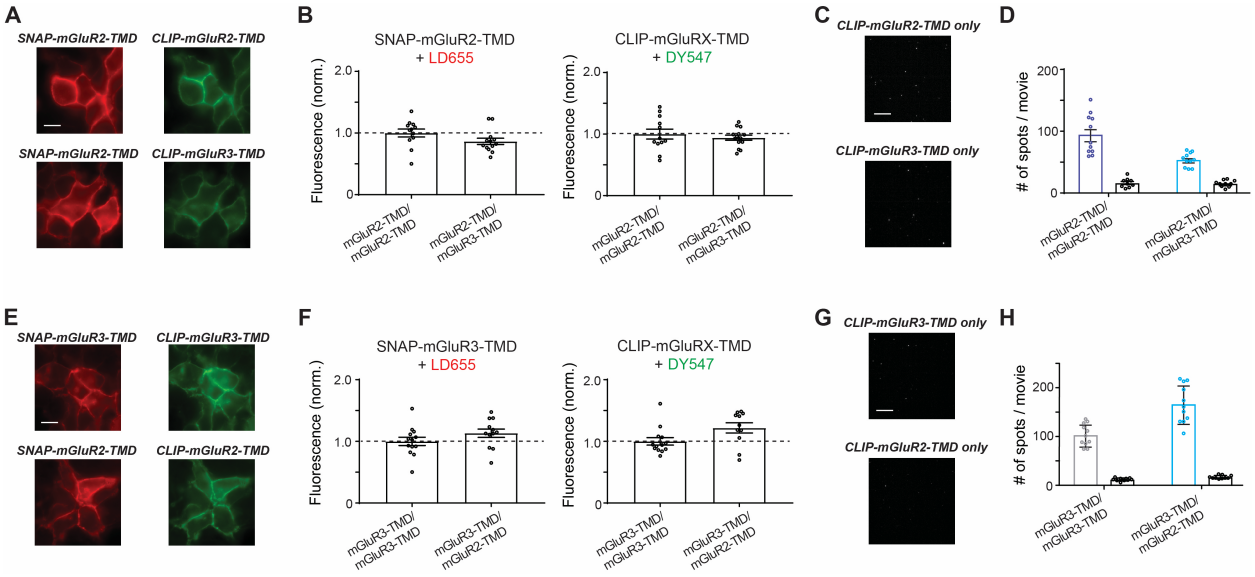

Figure 7-figure supplement 2